Detection system to study fundamental interactions in β decay of ^{21}Na

This work is part of the research programme of the Foundation for Fundamental Research on Matter (FOM), which is part of the Netherlands Organisation for Scientific Research (NWO).

Printed by: Ipskamp Drukkers, Enschede, February 2013

Rijksuniversiteit Groningen

Detection system to study fundamental interactions in β decay of ^{21}Na

Proefschrift

ter verkrijging van het doctoraat in de
Wiskunde en Natuurwetenschappen
aan de Rijksuniversiteit Groningen
op gezag van de
Rector Magnificus, dr. E. Sterken,
in het openbaar te verdedigen op
vrijdag 1 maart 2013
om 16:15 uur

door

Duurt Johan van der Hoek

geboren op 21 februari 1983
te Leeuwarden

Promotor:	Prof. dr. H.W.E.M. Wilschut
Beoordelingscommissie:	Prof. G. Ban Prof. A. Pellegrino Prof. Y. Sakemi

ISBN: 978-90-367-6087-4 Printed version
ISBN: 978-90-367-6088-1 Electronic version

Contents

1 Introduction **1**
1.1 Outline of this thesis 2

2 Theory **5**
2.1 Theory of weak interactions 5
2.2 Bounds on coupling coefficients 10
2.2.1 Limits on scalar interactions 11
2.2.2 Limits on tensor interactions 12
2.2.3 Limits on time-reversal violating interactions 14
2.3 ^{21}Na as a probe for non-SM interactions 15
2.4 Conclusions 18

3 Simulations **19**
3.1 The simulation 20
3.2 β-νcorrelation measurement (a) 21
3.2.1 Extracting a from recoil spectra 22
3.2.2 Systematic effects 30
3.3 β-Asymmetry measurement (A) 32
3.3.1 Systematic effects 37
3.4 Measurement of time-reversal violation, D coefficient 37
3.4.1 Cylindrical β- and recoil detector 41

3.4.2 Round β detector and 4π position sensitive recoil detection 41
3.4.3 Systematic effects 43
3.5 Conclusions 45

4 Experimental setup **47**
4.1 Production and transport of ^{21}Na 48
4.1.1 AGOR cyclotron and TRIμP isotope separator 48
4.1.2 Thermal Ionizer 48
4.1.3 Low energy beam line 50
4.2 Double-MOT system 50
4.2.1 Sodium trapping and the laser system 50
4.2.2 Collector MOT 52
4.2.3 Atom transfer 57
4.2.4 Decay MOT 57
4.3 Decay products detection 57
4.3.1 Recoil ion detector 58
4.3.2 β detector 58
4.4 Data acquisition 59

5 Recoil-ion momentum spectroscopy **61**
5.1 Setup 61
5.1.1 MCP and delay lines 63
5.1.2 Electronics and DAQ 63
5.2 Electric field and trajectory simulation 64
5.3 Measurements 66
5.3.1 Timing resolution 68
5.3.2 Position measurement and resolution 70
5.3.3 Discussion 71
5.4 Energy resolution 71
5.5 Distortions of the Electric field 73
5.6 Conclusions 76

6 β Detection **77**
6.1 Detector setup 78
6.1.1 Design of the ΔE and E detector 78
6.1.2 Acceptance and efficiency considerations 80
6.1.3 Electronics and DAQ 80
6.2 Measurements 83
6.2.1 Gain matching of the PMTs 83

6.2.2 Energy resolution and photon statistics 83
6.2.3 Position sensitivity 84
6.2.4 Timing resolution 91
6.2.5 Discussion 91
6.3 Conclusions 91

7 Summary and outlook **95**

Nederlandse Samenvatting **101**

Dankwoord **105**

Bibliography **107**

CHAPTER 1

Introduction

An important concept in physics is symmetry. In the theory of weak interactions, as introduced by Fermi in 1933 [1], the symmetries parity (P), charge conjugation (C), and time reversal (T) are all conserved. It was already clear that not only vector interactions, as was assumed by Fermi, would contribute when Lee and Yang noted in 1956 that in the weak interaction parity conservation was not yet checked [2]. Less than half a year later the first observations of P violation were made by Wu *et al.* [3], and of P and C violation by Garwin, Lederman and Weinrich [4].

β decay, and more general, the weak interaction, was soon found to be consistently described by vector and axial-vector currents with maximal P and C breaking, but with CP conserved. Assuming CPT invariance, also T was conserved.

Observing the various weak decay modes of the neutral-kaon system it was found in 1964 that CP, and indirectly with it, T is not conserved. There are two mechanisms leading to CP violation within the Standard Model (SM) of particle physics. With three families of quarks, the mixing matrix (Cabibbo-Kobayashi-Maskawa matrix) can have a complex phase, leading to CP and T violation. This is the most important source. From bounds on permanent electric dipole moments (EDMs) we know that in nuclear β-decay processes the resulting T-

violating effect will be immeasurably small. It is unclear why the effect is so small.

There are more aspects of nature, for instance gravity, dark matter, dark energy, and the matter-antimatter asymmetry in the universe, that is not explained by the SM. Therefore, one generally believes that there must be a theoretical description that goes beyond the SM. Theories that attempt to provide such models inevitably lead to modifications of the predictions of the SM, in particular to new sources of CP or T violation. They may also lead to V+A, scalar, or tensor contributions in weak decays. It is therefore worthwhile to consider to what extent β decay studies can be of use to the search for physics beyond the SM.

In this thesis we explore for ^{21}Na the possibilities to search for S or T interactions by measuring the β-ν correlation and the β asymmetry, i.e. the angular correlation between the lepton momenta $\mathbf{p}_\nu$ and $\mathbf{p}_e$ and correlation between $\mathbf{J}$ and $\mathbf{p}_e$, respectively. Most importantly, to search for time-reversal violation, the triple correlation between $\mathbf{J}$, $\mathbf{p}_\nu$, and $\mathbf{p}_e$ can also explored.

The fact that the recoil must be observed instead of the neutrino, results in very specific detection requirements. The recoil energy is only ∼200 eV, which means that the radioactive atoms cannot be implanted in a substrate. In this work we hold the atoms in an atom trap with various consequences for the production of the ^{21}Na source and the detection system measuring the β-decay correlations.

1.1 Outline of this thesis

The discussion in this thesis of the measurement of β-ν correlations consists of the following:

Chapter 2 gives the theoretical background of the weak interactions that is relevant for this thesis. β-decay correlation parameters are expressed in terms of the coupling constants of the most general weak interaction Hamiltonian. The current bounds on these coupling constants that are not part of the SM are discussed.

Chapter 3 describes simulations of β-decay events. These are used to estimate the statistical sensitivity of our setup to the correlation parameters and to determine the number of radioactive decays that need to be observed to put new bounds on non-standard interactions. In addition systematic errors are discussed and estimated using the simulation.

Chapter 4 describes the experimental setup that is used. Discussed are the

production and transport of ^{21}Na, the double-MOT system, and the detection of decay products.

Chapter 5 describes the design and performance of the recoil ion detector. The resolution of the position and time of the recoil detector is determined by ionizing atoms in the MOT with a pulsed UV laser.

Chapter 6 describes the design and performance of the β detector. The detector was characterized using a radioactive source. The position and timing resolution are determined.

Chapter 7 summarizes the main conclusions and gives an outlook of the use of this detection system in an actual experiment.

CHAPTER 2

Theory

In this chapter the theory is introduced that is needed to put the β-decay experiment in a theoretical context. In the most general Hamiltonian for β decay, there are 10 coupling constants of which only one is non zero in the SM. The current constraints on the non-standard couplings from various β-decay experiments are discussed. In this discussion we follow the notation of Herczeg [5].

2.1 Theory of weak interactions

In the framework of nuclear β decay one considers an effective semi-leptonic four-fermion interaction. The basic reaction for β decay is $d \to ue^-\overline{\nu}_e$ or $u \to de^+\nu_e$ at the quark level. Within the Standard Model (SM) only V−A type, 'vector minus axial-vector', interactions are present so that the charged gauge bosons, $W^\pm$, couple only to left-handed fermions. In a general model V+A type interactions, scalar (S), pseudoscalar (P), and tensor (T) interactions can also be considered. Table 2.1 summarizes the corresponding Dirac field bilinears. In the most general form of the β-decay Hamiltonian all these interactions are possible [5]:

$$H_\beta = H_{V,A} + H_{S,P} + H_T, \tag{2.1}$$

name		Γ
scalar	S	1
vector	V	γ^μ
tensor	T	$\sigma^{\mu\nu}$
axial-vector	A	$\gamma^\mu\gamma^5$
pseudoscalar	P	γ^5

Table 2.1: *Terminology of Dirac field bilinears of the form* $\overline{\psi}\Gamma\psi$

.

with

$$\begin{aligned} H_{V,A} &= \overline{e}\gamma^\mu(1-\gamma_5)\nu_e^{(L)}\left[a_{LL}\overline{u}\gamma_\mu(1-\gamma_5)d + a_{LR}\overline{u}\gamma_\mu(1+\gamma_5)d\right] \\ &\quad + \overline{e}\gamma^\mu(1+\gamma_5)\nu_e^{(R)}\left[a_{RL}\overline{u}\gamma_\mu(1-\gamma_5)d + a_{RR}\overline{u}\gamma_\mu(1+\gamma_5)d\right] \\ &\quad + \text{H.c.}, \end{aligned} \tag{2.2}$$

$$\begin{aligned} H_{S,P} &= \overline{e}(1-\gamma_5)\nu_e^{(L)}\left[A_{LL}\overline{u}(1-\gamma_5)d + A_{LR}\overline{u}(1+\gamma_5)d\right] \\ &\quad + \overline{e}(1+\gamma_5)\nu_e^{(R)}\left[A_{RL}\overline{u}(1-\gamma_5)d + A_{RR}\overline{u}\gamma_\mu(1+\gamma_5)d\right] \\ &\quad + \text{H.c.}, \end{aligned} \tag{2.3}$$

$$\begin{aligned} H_T &= \alpha_{LL}\overline{e}\frac{\sigma^{\mu\nu}}{\sqrt{2}}(1-\gamma_5)\nu_e^{(L)}\,\overline{u}\frac{\sigma_{\mu\nu}}{\sqrt{2}}(1-\gamma_5)d \\ &\quad + \alpha_{RR}\overline{e}\frac{\sigma^{\mu\nu}}{\sqrt{2}}(1+\gamma_5)\nu_e^{(R)}\,\overline{u}\frac{\sigma_{\mu\nu}}{\sqrt{2}}(1+\gamma_5)d \\ &\quad + \text{H.c.}, \end{aligned} \tag{2.4}$$

where the a_{ij}, A_{ij} and α_{ij}, with $i,j = L,R$ are the chiral coupling constants, and H.c. denotes the Hermitian conjugate. The first (second) index on these coupling constants indicates the chirality of the leptons (quarks) that are involved. In the Standard Model the only non-zero coupling constant is

$$a_{LL} = \frac{G_F V_{ud}}{\sqrt{2}} = \frac{g^2 V_{ud}}{8M_W^2}, \tag{2.5}$$

but in this general parametrization there are 10 independent complex parameters or 20 independent real parameters, that determine the mix of (axial) vector, (pseudo-) scalar and tensor contributions to the interaction. The value of these parameters determine the properties of the Hamiltonian under C, P, and T transformations.

	Fermi	Gamow-Teller
Spin $e\nu$ pair	0	1
$\|\Delta J\|$	0	0, 1 ($0 \to 0$ not allowed)
Interaction types	V, S	A, T

Table 2.2: *Summary of properties of pure Fermi and pure Gamow-Teller transitions.*

When calculating transition amplitudes in β-decaying nuclei, one has to calculate matrix elements of Eq. (2.1) between nucleon states (neutron $|n\rangle$ and proton $|p\rangle$). The constants $g_i \equiv g_i(0)$ that arise, and will be present in the expressions of many observables in this chapter, are defined by the form factors

$$\begin{aligned}
\langle p|\bar{u}\gamma_\mu d|n\rangle &= g_V(q^2)\bar{p}\gamma_\mu n,\\
\langle p|\bar{u}\gamma_\mu\gamma_5 d|n\rangle &= g_A(q^2)\bar{p}\gamma_\mu\gamma_5 n,\\
\langle p|\bar{u}d|n\rangle &= g_S(q^2)\bar{p}n,\\
\langle p|\bar{u}\sigma_{\mu\nu}d|n\rangle &= g_T(q^2)\bar{p}\sigma_{\mu\nu}n,\\
\langle p|\bar{u}\gamma_5 d|n\rangle &= g_P(q^2)\bar{p}\gamma_5 n.
\end{aligned} \tag{2.6}$$

In the non-relativistic limit, which applies to nuclear β-decay processes, the pseudoscalar expression vanishes.

In nuclei one can select transitions where the combined spin of the emitted leptons is 0 or 1. These are referred to as Fermi and Gamow-Teller transitions respectively. The kinetic energy of the daughter nucleus is about 8 orders of magnitude smaller than its rest mass. Therefore, in the Dirac spinors of the proton and the neutron one can neglect the 'small component'[1] χ in $\psi = (\phi, \chi)$. In this limit (*cf.* Ref. [6]) we have that all V and S terms reduce to $\phi_p^\dagger\phi_n$, vanishing when the spin changes, and all A and T terms reduce to $\phi_p^\dagger\boldsymbol{\sigma}\phi_n$, vanishing when the spin remains the same. Therefore, in a pure Fermi transition only V and S interactions are present, in a pure Gamow-Teller transition only A and T. Table 2.2 summarizes the properties of these two types of transitions. Pseudoscalar terms can be neglected altogether, since these terms contain the small component χ. In mixed transitions all types of interactions potentially play a role. Later we will see that this is important for measurements of time-reversal violation.

[1] ψ denotes a four-component Dirac spinor, ϕ and χ both denote a two-component spinor, and $\boldsymbol{\sigma} = (\sigma_x, \sigma_y, \sigma_z)$.

Symmetry	Conserved if
C	$\lvert X_L\rvert=\lvert X_R\rvert$ and $\lvert X_L^{'}\rvert=\lvert X_R^{'}\rvert$
P	$X_L = \pm X_R$ and $X_L^{'} = \pm X_R^{'}$
T	$\mathrm{Im}(X_L^{(')}) = 0$, up to common phase

Table 2.3: *Summary of conditions for conservation of C, P and T. $X^{(')}$ can stand for a, A and α (cf. Eqs. (2.2-2.4)), both primed and unprimed.*

We will use combinations of coupling constants such as $a_{LL} + a_{LR}$ or $A_{RL} - A_{RR}$ where in all cases the two terms share a common first index. Therefore it is convenient to define

$$\begin{aligned} X_L &\equiv X_{LL} + X_{LR}, & X'_L &\equiv X_{LL} - X_{LR}, \\ X_R &\equiv X_{RL} + X_{RR}, & X'_R &\equiv X_{RL} - X_{RR}, \\ \alpha_L &\equiv \alpha_{LL}, & \alpha_R &\equiv \alpha_{RR}, \end{aligned} \tag{2.7}$$

where X_{ij} stands for A_{ij} or a_{ij}. The index on X_i indicates the chirality of the leptons that are involved in the interaction, e.g. A_R describes the strength of the scalar contribution involving right-handed neutrino's and electrons. Table 2.3 summarizes the conditions for conservation of C, P, and T in terms of the parameters defined in Eq. (2.7).

From the Hamiltonian, Eqs. (2.1-2.4), it can be shown that the β-decay rate is given by[2] [7]

$$\begin{aligned} &\omega(\langle J\rangle|E_e,\Omega_e,\Omega_\nu)\,dE_e\,d\Omega_e\,d\Omega_\nu = \\ &\quad \frac{1}{(2\pi)^5} p_e E_e (Q + m_e - E_e)^2\,dE_e\,d\Omega_e\,d\Omega_\nu\,\xi \\ &\quad \times \left[1 + a\frac{\mathbf{p}_e\cdot\mathbf{p}_\nu}{E_e E_\nu} + b\frac{m_e}{E_e} + c\left(\frac{1}{3}\frac{\mathbf{p}_e\cdot\mathbf{p}_\nu}{E_e E_\nu} - \frac{(\mathbf{p}_e\cdot\mathbf{j})(\mathbf{p}_\nu\cdot\mathbf{j})}{E_e E_\nu}\right)\right. \\ &\quad \left. \times \left(\frac{J(J+1) - 3\langle(\mathbf{J}\cdot\mathbf{j})^2\rangle}{J(2J-1)}\right) + \frac{\langle\mathbf{J}\rangle}{J}\cdot\left(A\frac{\mathbf{p}_e}{E_e} + B\frac{\mathbf{p}_\nu}{E_\nu} + D\frac{\mathbf{p}_e\times\mathbf{p}_\nu}{E_e E_\nu}\right)\right], \end{aligned} \tag{2.8}$$

where $E_{e(\nu)}$ is the total relativistic energy of the electron (neutrino), $\mathbf{p}_{e(\nu)}$ the momentum of the electron (neutrino), Q the available kinetic energy in the

[2]The complete expression contains many more correlations, see [7, 8]. They are omitted here since they contain the spin of the β particle which will not be measured in our experiment.

decay, **J** the spin of the parent nucleus and **j** a unit vector parallel to it. a, b, c, A, B and D are referred to as the correlation parameters. The values of these correlation parameters are closely related to the symmetry properties of the theory. For example, under a parity transformation the terms involving A and B acquire a minus sign, so a non-zero value for A or B implies P-violation. A non-zero D can be caused by T-violation or final-state interactions (FSI, further discussion in section 2.2.3). In Eq. (2.8), terms involving the spin polarization of the outgoing β particle are not given since in this work we do not consider measuring it.

The correlation parameters as well as ξ are defined in terms of the free parameters of the nuclear β-decay Hamiltonian. The expression for ξ is

$$\begin{aligned}\xi =&|M_F|^2(|a_L|^2 + |a_R|^2 + |A_L|^2 + |A_R|^2) \\ &+ |M_{GT}|^2(|a'_L|^2 + |a'_R|^2 + |\alpha_L|^2 + |\alpha_R|^2).\end{aligned} \tag{2.9}$$

where M_F (M_{GT}) is the Fermi (Gamow-Teller) matrix element of the nuclear transition.

The expressions for the coupling constants are taken from Jackson *et al.* [7]. However, we have chosen to parametrize the coupling constants using the chiral notation of Eq. (2.2-2.4) following Herczeg [5], this makes the coupling to left- and right-handed leptons and quarks explicit. In the expressions for the correlation parameters the mixing parameter ρ is used, defined by

$$\rho = \frac{g_A M_{GT}}{g_V M_F}. \tag{2.10}$$

Keeping the leading-order terms one finds for the β-ν correlation parameter a

$$\begin{aligned}a_F &= 1 - \frac{4g_S^2(|A_L|^2 + |A_R|^2)}{g_V^2(|a_L|^2 + |a_R|^2) + g_S^2(|A_L|^2 + |A_R|^2)}, \\ a_{GT} &= -\frac{1}{3} + \frac{g_T^2(|\alpha_L|^2 + |\alpha_R|^2)}{3g_A^2(|a'_L|^2 + |a'_R|^2) + 4g_T^2(|\alpha_L|^2 + |\alpha_R|^2)},\end{aligned} \tag{2.11}$$

where the F (GT) subscript indicate the case for a pure Fermi (Gamow-Teller) transition. The values $a_F = 1$ and $a_{GT} = -1/3$ are the Standard Model values and for mixed transitions one has [9]

$$a_{SM} = \frac{1 - \rho^2/3}{1 + \rho^2}. \tag{2.12}$$

For b, A and D the leading-order terms are linear in the non-SM couplings. For the Fierz interference parameter b one finds

$$b_F = \pm\frac{2\gamma g_s g_V \mathrm{Re}[A_L(a_L^* - a_R^*)]}{g_V^2(|a_L|^2+|a_R|^2)+g_S^2(|A_L|^2+|A_R|^2)} \simeq \pm\frac{2\gamma g_S \mathrm{Re}[A_L]}{g_V a_L}, \tag{2.13}$$

$$b_{GT} = \pm\frac{4\gamma g_T}{g_V}\mathrm{Re}[\alpha_{LL}], \tag{2.14}$$

where $\pm$ refers to $\beta^{\mp}$ decay, $\gamma = \sqrt{1-(\alpha Z)^2}$, Z being the element number of the daughter nucleus and α the fine-structure constant. The approximate expressions for the β-asymmetry parameter $\tilde{A}$ (as defined in Eq. (2.18)) are

$$\tilde{A}_{GT} \simeq A_{SM} + 4\alpha Z\Big\langle\frac{m}{p_e}\Big\rangle\mathrm{Im}(g_T\alpha_L) + 4\gamma\Big\langle\frac{m}{E_e}\Big\rangle\mathrm{Re}(g_T\alpha_L), \tag{2.15}$$

and of course $A_F = 0$. The TRV triple correlation parameter D is given by

$$D \simeq -4\delta_{J'J}\frac{\rho}{1+\rho^2}\sqrt{\frac{J}{J+1}}\mathrm{Im}(a_{LR}). \tag{2.16}$$

Sensitivity to D requires a mixed transition, because it can only arise from the relative phase between V and A contributions in the Hamiltonian.

2.2 Bounds on coupling coefficients

In this section we discuss the bounds that have been put on the coupling coefficients that were introduced in section 2.1.

Noteworthy is the fact that b has a linear dependence on the non-SM coupling constants, and a a quadratic dependence. In the next chapter we will see that in experiments that are designed to measure a, one actually measures $\tilde{a}$ instead, defined by

$$\tilde{a} \equiv \frac{a}{1+b\langle\frac{m_e}{E_e}\rangle}. \tag{2.17}$$

Therefore, in a measurement of a one is actually most sensitive to the parameters that enter linearly through b. Analogous, in measurements of the β-asymmetry

parameter A one measures

$$\tilde{A} \equiv \frac{A}{1 + b\langle \frac{m_e}{E_e} \rangle}. \tag{2.18}$$

In chapter 3 we will see that the expression for $\tilde{A}$ is exact, but for $\tilde{a}$ it is not. There we will also show that in a typical β-decay experiment measuring D one actually measures

$$\tilde{D} = \frac{D}{1 + \Delta}, \tag{2.19}$$

where Δ is some combination of non-SM couplings including b. The main point is that in the SM $D \lesssim 10^{-12}$ [10], and therefore, to lowest order in non-SM couplings, one is only sensitive to $\mathrm{Im}(a_{LR})$, the coupling appearing in D itself.

Except for the section on time-reversal violation, we assume in the remainder of this section the SM case for V and A interactions: $a_{LL} = 1$ and all other $a_{ij} = 0$.

2.2.1 Limits on scalar interactions

From Eqs. (2.11), (2.13) and (2.17) it can be seen that measuring the coefficient $\tilde{a}$ for a pure Fermi transition, puts constraints on the parameters $g_S A_L = g_S(A_{LL} + A_{LR})$ and $g_S A_R = g_S(A_{RL} + A_{RR})$, i.e. the scalar couplings. The constraints are shown in Fig. 2.1. Assuming they are real the annular-shaped bounds can be constructed from the measurements that are listed in the caption. In the case of ^{21}Na, which decays by a mixed transition, the tensor contributions (see expressions a_{GT} and b_{GT}) are set to zero, resulting in upper bounds for the scalar couplings.

The exclusion band labeled '$0^+ \to 0^+$' in Fig. 2.1 puts a very stringent constraint on the scalar couplings to left-handed neutrinos (A_L). It comes from precise life time measurements of superallowed Fermi decays, which are used to measure V_{ud}. The life time (or decay rate) follows from Eq. (2.8) by integrating over all five kinematic variables. The result will depend on the parameter b; all other terms in Eq. (2.8) are odd functions w.r.t. the integration region. From the set of measured life times one can extract not only V_{ud} but also a value for b_F (Eq. (2.13)), and put a bound on A_L. For details we refer to Towner and Hardy [11]. This method can also be applied to mirror transitions. A correlation measurement, to determine ρ, combined with a precise lifetime measurement can be used to extract $|V_{\mathrm{ud}}|$ [12], and also allows to extract from the dependence of

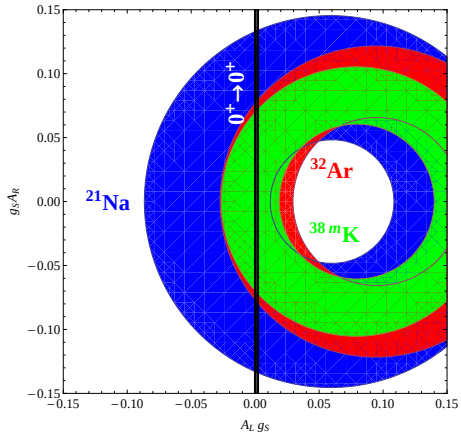

Figure 2.1: *Bounds (90% C.L.) on the scalar couplings (A) in the $A_L A_R$ plane. The circular shape of the exclusion regions can be understood from the structure of Eq. (2.11). The appearance of b in $\tilde{a}$ (Eq. (2.17)) causes a shift of the center of the circle. The measurements in this plot are from ^{32}Ar [13], ^{21}Na [14], and $^{38}K^m$ [15]. The vertical exclusion band is from a combined analysis of several experiments [11]. Figure courtesy of Hans Wilschut and Nathan Mol.*

b values a limit on the combination of left-handed scalar and tensor interactions (A_L and α_L). A coherent set of data on mirror nuclei can be as powerful as superallowed Fermi transitions.

Although these lifetime measurements put a very tight bound on $g_S A_L$, they have no constraining power on $g_S A_R$. This is where β-decay measurements of $\tilde{a}$ are relevant. The most constraining measurement is from $^{38}\mathrm{K}^m$.

Measuring $\tilde{a}$ is not the only way to constrain A_R: other observations should be considered as well. In Ref. [16] a connection is made between the neutrino mass and non-SM interactions in β decay. An order of magnitude estimation is made putting a tight constraint on right-handed scalar-currents. According to the author the constraint $|A_{RL} + A_{RR}| \lesssim 2 \times 10^{-3}$ is quite general.

2.2.2 Limits on tensor interactions

By measuring $\tilde{a}$ for pure Gamow-Teller transitions, one can put bounds on the tensor contributions to the weak interaction, see Eqs. (2.11) and (2.13). Fig. 2.2 shows the the annulus shaped confidence interval it provides.

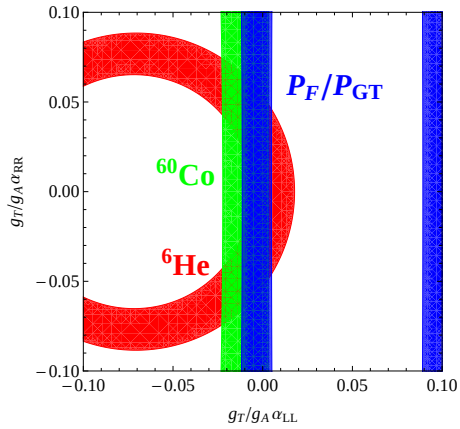

Figure 2.2: *Bounds (90% C.L.) on the tensor couplings α in the $\alpha_{LL}\alpha_{RR}$ plane. The circular bound comes from ^{6}He [19, 20], the green vertical band from ^{60}Co [21] and the double band from [18]. Figure courtesy of Hans Wilschut and Nathan Mol.*

The green vertical band comes from measurements of $\tilde{A}_{GT}$, which is sensitive to both $\mathrm{Im}(g_T\alpha_{LL})$ and, through b_{GT}, to $\mathrm{Re}(g_T\alpha_{LL})$ (see Eq. (2.15)). Due to the tight bound on $\mathrm{Im}(g_T\alpha_L)$ from measurements on the time-reversal violating coefficient R [17], one may assume that the term containing $\mathrm{Re}(g_T\alpha_L)$ dominates. A measurement of $\tilde{A}_{GT}$ is in essence a measurement of b_{GT}.

A third bound comes from measurements of the longitudinal polarization of β particles. The associated correlation, not shown in Eq. (2.8), is $G\boldsymbol{\sigma}_e \cdot \mathbf{p}_e/m_e$, where $\boldsymbol{\sigma}_e$ is the spin vector of the β particle. The measurement done by Wichers *et al.* [18] was originally performed to put bounds on parameters in left-right symmetric models. In such case only vector and axial-vector contributions play a role. Consequently, b vanishes and $\tilde{G} = G$. In contrast, allowing for other types of interactions, the result can be used to put bounds on tensor contributions. As was the case in the $\tilde{A}$ measurements the dependence on the non-SM interactions goes through b. The resulting boundary is shown as blue bands.

Thus, as was the case for scalar couplings, also in tensor couplings the left-handed currents are much better constrained than the right handed. Also here the mass limits of the neutrino give an order of magnitude bound [16]: $|\alpha_{RR}| \lesssim 10^{-3}$.

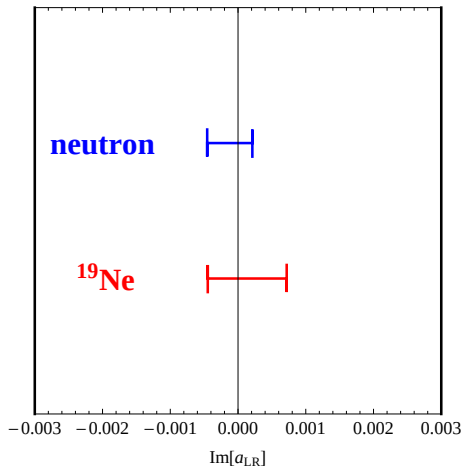

Figure 2.3: *The bounds (90% C.L.) on $Im(a_{LR})$ from measurements of the T-violating parameter D. The neutron measurement is from [24], the ^{19}Ne measurement from [25]. Figure courtesy of hans Wilschut and Nathan Mol.*

2.2.3 Limits on time-reversal violating interactions

We now discuss the bounds obtained from the measurements of the time-reversal violating correlation $D\mathbf{J}\cdot(\mathbf{p}_e\times\mathbf{p}_\nu)$. The approximate expression for D is given by Eq. (2.16) and shows it requires a mixed transition. It also follows that upper bounds on D impose a bound on interactions involving left-handed neutrinos.

It is known that final-state interactions (FSI) produce a non-zero contribution D [22]. The FSI have to be calculated which can be done to a precision better than 1% [22]. For neutrons FSI are at the level of 10^{-5} and for ^{21}Na at 10^{-4} [23] so that contributions from a true time-reversal-violating effect can be probed down to 10^{-6} for ^{21}Na.

The current experimental limits are still an order of magnitude higher than the contribution of the final-state interactions: the strongest bound so far is from the β decay of neutrons, $D=(-0.96\pm2.14)\times10^{-4}$ [24]. The best value for nuclei to date is the 1984 measurement using polarized ^{19}Ne, $D=(4\pm8)\times10^{-4}$ [25]. The resulting bounds on $\mathrm{Im}(a_{LR})$ from these two measurements are shown in Fig. 2.3.

Complementary to these time-reversal violating D-coefficient measurements are searches for permanent electric dipole moments (EDMs). The presence

of a permanent EDM, d, would violate P and T whereas the D coefficient is related to T violation only. Within a certain model one can evaluate the connection between D and d, which means that a bound on one implies a bound on the other. This correspondence depends on the model under consideration. A recent discussion is in Ref. [26]. New in this paper is that also with leptoquark models EDM measurements imply a tight bound on D, whereas they were first considered 'EDM safe' (Herczeg 2005 [27]). Also, in the more recent paper the 2006 bound on the neutron EDM [28] is included, providing the most stringent bounds on D: for models with left-right symmetry, exotic fermions and the R-parity violating minimal supersymmetric standard model $D < 4 \times 10^{-7}$ and for leptoquark models with (without) light right-handed neutrino's $D < 4 \times 10^{-5}$ (1×10^{-5}). In Ref. [26] these limits are expressed in terms of D/κ, where κ is the numerical factor in front of $\mathrm{Im}(a_{LR})$ in Eq. (2.16). The above numbers are for ^{21}Na, i.e. $\kappa = 1.46$, see Eq. (2.26). From Ref. [29] it appears that further scrutiny of the results in [26] is required. Again, a direct, model independent measurement of D would avoid theoretical uncertainties from deriving bounds from the EDM and the issues of fine tuning.

2.3 ^{21}Na as a probe for non-SM interactions

In this section we discuss some relevant properties of the β^+ decay of ^{21}Na. Also, given the current bounds on the exotic couplings, we calculate the required precision for a competitive measurement of a, A or D measurement using ^{21}Na.

^{21}Na undergoes a mixed β^+ transition which is suitable to measure D. Table 2.4 summarizes the main properties of the decay.

From the existing bounds and the expressions of the correlation coefficients in terms of the coupling constants we can determine the required sensitivity of our experiment. Consider a measurement of $\tilde{a}$. When we make the following assumptions: all coupling constants are real, V and A interactions are as in the SM ($a_{LL} = 1$ and all other a_{ij} are zero) and there are no tensor contributions, then we can write

$$\tilde{a} \simeq a_{SM} - C_1(g_s A_L)^2 - C_2(g_s A_R)^2 + 2C_3(g_s A_L). \tag{2.20}$$

The appearance of the linear C_3-term in Eq. (2.20) comes from the presence of

Property ^{21}Na	Value	
$T_{1/2}$	22.49	s
Endpoint	2525.6	keV
Branching ratio	94.84	%
$\rho = \frac{g_A M_{GT}}{g_V M_F}$	0.7034	(32)
a	0.5587	(27)
c	0.2648	(16)
A	0.8614	(19)
B	0.59661	(32)
G	1	

Figure 2.4: *Main decay properties of ^{21}Na to the ground state of ^{21}Ne. The first half of the table is taken from [30], the second half (except the value of G) from [31].*

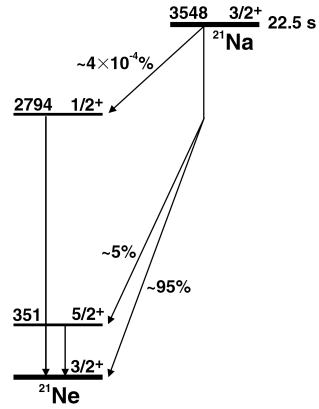

Figure 2.5: *Decay scheme of ^{21}Na.*

b in $\tilde{a}$. The coefficients C_1, C_2 and C_3 (taking $g_V = a_{LL} = 1$) are

$$\begin{aligned} C_1 &= C_2 - \frac{4C_3^2}{a_{SM}}, \\ C_2 &= \frac{2(\rho^2/3+1)}{(\rho^2+1)^2}, \\ C_3 &= \frac{a_{SM}\gamma m_e}{(\rho^2+1)E_e}. \end{aligned} \tag{2.21}$$

In Fig. 2.1 it can be seen that A_R is tightly bound around the line $A_L = 0$, by the $0^+ \to 0^+$ measurements. If we parametrize the confidence interval of the measured value of $\tilde{a}$ as $(a_{SM} - \delta_-) < \tilde{a} < (a_{SM} + \delta_+)$, we can write the bound for $g_s A_R$ on the line $A_L = 0$ as

$$|g_s A_R| < \sqrt{\frac{\delta_-}{C2}} \tag{2.22}$$

So, with a larger C_2 one can set a tighter bound for a given δ_-. On the line

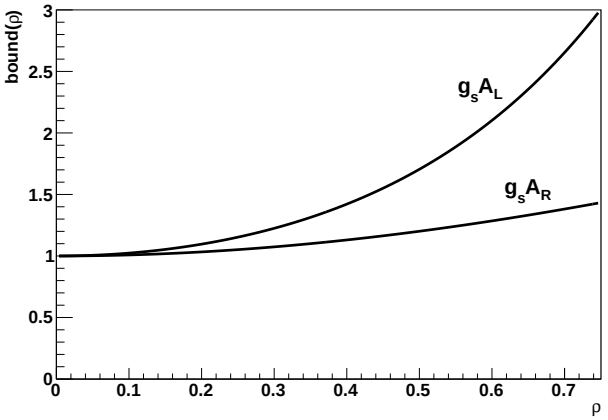

Figure 2.6: *The bounds on left and right-handed scalar-couplings as a function of the mixing parameter ρ, normalized to the pure Fermi case ($\rho = 0$). For ^{21}Na $\rho \simeq 0.70$. Note that only the ρ-dependence is plotted; the bound on A_R depends on $\langle 1/E_e \rangle$.*

$A_R = 0$ we find a bound on $g_S A_L$

$$(g_S A_L)_\pm = \frac{C_3 - \sqrt{C_3^2 \mp C1\delta_\pm}}{C_1} \simeq \pm \frac{(\rho^2+1)E_e}{2a_{SM}\gamma m_e}\delta_\pm, \tag{2.23}$$

where the approximation describes the limit $C_3^2 \gg C1\delta_\pm$. Although this condition is not met in case of $\delta_-/a = 1\%$ error, the approximation estimates the bound accurate to about[3] $\sim$10%. From the above two formulas it can be seen that the sensitivity to both A_L and A_R depends on the mixing parameter ρ. Fig. 2.6 shows that for a given measurement the highest sensitivity is reached for $\rho = 0$, i.e. a pure Fermi decay. In any the case the bound on A_L from measuring $\tilde{a}$ is inferior to the bound from the super allowed $0^+ \to 0^+$ decay rates; we will not consider this further.

The numerical values for ^{21}Na are

$$C_1 = 0.97, \quad C_2 = 1.0, \quad \text{and} \quad C_3 = 0.10 \tag{2.24}$$

[3]In this approximation the lower bound is overestimated by about 10%, the upper bound underestimated by about 15%.

For comparison, the decay of $^{38}\mathrm{K}^m$, a pure Fermi decay, has $C_2 = 2.0$, i.e. a factor 1.4 higher sensitivity.

Assuming a measurement result of the form $\tilde{a} = a_{SM} \pm \sigma_a$, with the current limit from ^{21}Na of $|g_s A_R| < 0.13$ this leads to a required precision (1σ) of $0.13^2/0.55 = 3\%$. The tightest bound is from $^{38}\mathrm{K}^m$ and to compete with this measurement, 0.8% precision is needed for ^{21}Na.

For $\tilde{A}$ in ^{21}Na decay, we can write

$$\tilde{A} = 0.8655 - 0.24\mathrm{Re}(g_T \alpha_L). \tag{2.25}$$

The current limit is $|g_T \alpha_L| < 2.3 \times 10^{-3}$, and assuming that a measurement of $\tilde{A}$ yields a central value equal to 0.8655, one needs a precision of 5.6×10^{-4} or 0.6‰ to compete with the bound from the P_F/P_{GT} measurement, shown in Fig. 2.2.

Using Eq. (2.16), we have for ^{21}Na and for the neutron

$$D_{\mathrm{Na}} \simeq 1.46\mathrm{Im}(a_{LR}), \qquad D_{\mathrm{n}} \simeq -0.87\mathrm{Im}(a_{LR}), \tag{2.26}$$

where for the neutron $\rho = \sqrt{3} g_A/g_V \simeq 2.2$ was taken. The value of $D_n = (-0.96 \pm 2.14) \times 10^{-4}$ taken from Mumm 2011 [24] implies a required 4×10^{-4} precision in D_{Na} to be competitive.

2.4 Conclusions

In this chapter we introduced the most general Hamiltonian for β decay requiring 10 complex coupling coefficients. In β-decay experiments one can measure correlation coefficients as defined in Eq. (2.8). Bounds on the coupling coefficient derived from such measurements were presented.

To be competitive with the current bounds we need to measure a with a precision (i.e. 1σ) of 0.8%, A with 0.6‰ and D, which is a zero measurement, at the 4×10^{-4} level.

CHAPTER 3

Simulations

In chapter 2 we discussed several correlation parameters and their corresponding experimental bounds on non-Standard Model contributions to β decay. This chapter will describe a Monte Carlo simulation of the experiments to determine how well these correlation parameters must be measured to obtain more precise bounds.

In the simulation β-decay events are randomly generated from the distribution

$$\begin{aligned}\omega(\langle J\rangle|E_e,\Omega_e,\Omega_\nu)\,dE_e\,d\Omega_e\,d\Omega_\nu = \\ \frac{1}{(2\pi)^5}p_eE_e(Q+m_e-E_e)^2\,dE_e\,d\Omega_e\,d\Omega_\nu\,\xi\left[1+a\frac{\mathbf{p}_e\cdot\mathbf{p}_\nu}{E_eE_\nu}+b\frac{m_e}{E_e}\right. \\ +c\left(\frac{1}{3}\frac{\mathbf{p}_e\cdot\mathbf{p}_\nu}{E_eE_\nu}-\frac{(\mathbf{p}_e\cdot\mathbf{j})(\mathbf{p}_\nu\cdot\mathbf{j})}{E_eE_\nu}\right)\left(\frac{J(J+1)-3\langle(\mathbf{J}\cdot\mathbf{j})^2\rangle}{J(2J-1)}\right) \\ \left.+\frac{\langle\mathbf{J}\rangle}{J}\cdot\left(A\frac{\mathbf{p}_e}{E_e}+B\frac{\mathbf{p}_\nu}{E_\nu}+D\frac{\mathbf{p}_e\times\mathbf{p}_\nu}{E_eE_\nu}\right)\right],\end{aligned} \tag{3.1}$$

where $E_{e(\nu)}$ is the total relativistic energy[1] of the electron (neutrino), $\mathbf{p}_{e(\nu)}$ the momentum of the electron (neutrino), Q the available kinetic energy in the

[1] In this chapter the *kinetic energy* of the recoil nucleus is denoted by E_r.

decay, **J** the spin of the nucleus and **j** a unit vector parallel to it, and a, b, c, A, B and D are the correlation parameters. The correlation parameters as well as ξ are defined in terms of a set of coupling coefficients in the general β-decay Hamiltonian. For explicit expressions see chapter 2 and [7,9]. In the remainder of this chapter we will use

$$\frac{\langle \mathbf{J} \rangle}{J} \equiv P\mathbf{j} \tag{3.2}$$

defining the degree of polarization P.

The layout of the chapter is as follows. In section 3.1 details of the simulation are discussed. Sections 3.2 to 3.4 discuss some possibilities for measuring the correlation coefficients a, A and D. Assuming the current setup in terms of geometry and detector properties we estimate the number of decays needed in the decay MOT for a competitive measurement of all these parameters. In addition some systematic errors are considered. The parameters that are studied are the MOT position (x, y and z), the size of the MOT cloud, the β threshold, and, for A and D, the orientation of **J**.

3.1 The simulation

The main goal of the simulation is to estimate the required number of decays in the MOT to reach a certain precision. Additionally, systematic effects can be studied. Events need to be generated following the distribution given by Eq. (3.1) and a detector geometry has to be implemented to count events. The simulation done here is not intended to simulate the system in as great a detail required to actually analyze a real experiment. More attention would need to be payed to the exact geometry of the detectors and chamber to simulate the background, from for instance back scattering of β particles. Such studies would also require additional experiments.

The heart of the event generator is the ROOT class TGenPhaseSpace [32]. Given the initial energy and momentum in the decay and the masses of the decay products, it generates the four-momenta in the final state. The algorithm produces a uniform distribution over the kinematically allowed region of phase space. The matrix element including all the correlations (the terms between square brackets in Eq. (3.1)), are calculated with the generated momenta. Accepting or rejecting the event with a probability proportional to the matrix element will produce a set of events following Eq. (3.1). The event files are

saved so that analysis and event generation are separated. A single file contains events (typically 10^7) with a fixed value for all correlation parameters and P.

Detectors of two types can be placed around the center: β detectors and detectors for the recoiling daughter nucleus. Detectors can be placed as desired and single and coincidence rates can be 'recorded'. The implementation of the detectors is such that only cylindrical detectors can be placed. For the β detector this is a realistic approach. The recoils, however, are guided by an electric field to an MCP so that 4π of solid angle is covered. A realistic scenario would be that in a D measurement the MCP will be divided into two halves. In the simulation this can be realized by putting two very large circular detectors very close to the decay center, each essentially covering 2π of solid angle. The β detector is not only defined in terms of its geometry. An energy threshold can be defined which the β energy needs to exceed for the detector to record a hit. The hit probability is not a step function of the energy but rather a smooth function with a certain width, modeled after the response determined by a simulation using the Casino software [33].

Using the event files and the array of detectors, an analyzer runs over all events and checks for every detector whether it is hit and, only for the β detectors, if its energy exceeds threshold. The event file does not contain information about the location of the decay. The position and size of the trapped cloud can be manipulated in the analysis stage. When a non-zero MOT size d is used, an initial position is randomly taken from a 3D-Gaussian distribution with $\sigma = d$ in all directions. Also the location of the cloud can be chosen. Lastly, for the recoils the hit position on and the time of flight to the MCP is calculated assuming a ballistic trajectory in a uniform electric field. In the actual experiment these are the observables from which the recoil momentum is calculated. Doing this in the simulation results in a recoil energy spectrum that reflects uncertainties of the finite cloud size.

In the remainder of this chapter the measurement concepts of a, A and D will be discussed. The central questions are: 1) How is the coefficient determined from the observables? 2) How many events do we need for a given precision? 3) How large are some of the important systematic effects that we can foresee at this point?

3.2 β-ν correlation measurement (a)

We will discuss two different approaches to determine the β-ν correlation parameter a, both of which require the detection of the recoil ion. In the first

β detector threshold (MeV)	% detected
0	100
0.2	96
0.4	90
0.6	80
0.8	68
1.0	55

Table 3.1: *Percentage of events above β threshold.*

approach the recoil energy (E_r) spectrum is measured. It can be derived [34] that the distribution of the recoil energy is given by

$$R(E_r)dE_r = 8\pi^2 dE_r \int_{E_{\min}}^{E_{\max}} dE_e\, E_e(M_r + E_r)A(1 - a\frac{p_e^2 - p_r^2 + A^2}{2W_e A} + b\frac{m_e}{E_e}), \tag{3.3}$$

where $A = Q - E_r - E_e$ and $E_{\min}$ and $E_{\max}$ are determined from the decay kinematics and depend on E_r. The shape of the kinematically allowed region can be seen in Fig. 3.1, which shows the 2D spectrum of the the recoil energy vs. the β (kinetic) energy, resulting from the integrand of Eq. (3.3). The value of a determines the shape of the recoil spectrum. In Fig. 3.2 recoil energy spectra for some typical values of a are shown. The phase space distribution has $a = 0$, while $a = -\frac{1}{3}$ and $a = 1$ are for pure Fermi and pure Gamow-Teller transitions, respectively. $a = 0.558$ is (close to) the value expected for ^{21}Na decay [31]. In the second approach the time of flight (TOF) spectrum is measured; its shape is also sensitive to the value of a.

3.2.1 Extracting a from recoil spectra

In the following the value of a will be determined from energy and TOF spectra. The function that is fitted to the data is constructed from the simulation. It includes, for example, effects due to a finite MOT-cloud size and a non-zero β-energy threshold, which cannot be cast into an analytical expression. When generating the fit function with the simulation, it is assumed that $b = 0$, so that in effect the actual fit parameter is not just a, but

$$\tilde{a} \simeq \frac{1}{1 + b\langle\frac{m_e}{E_e}\rangle}. \tag{3.4}$$

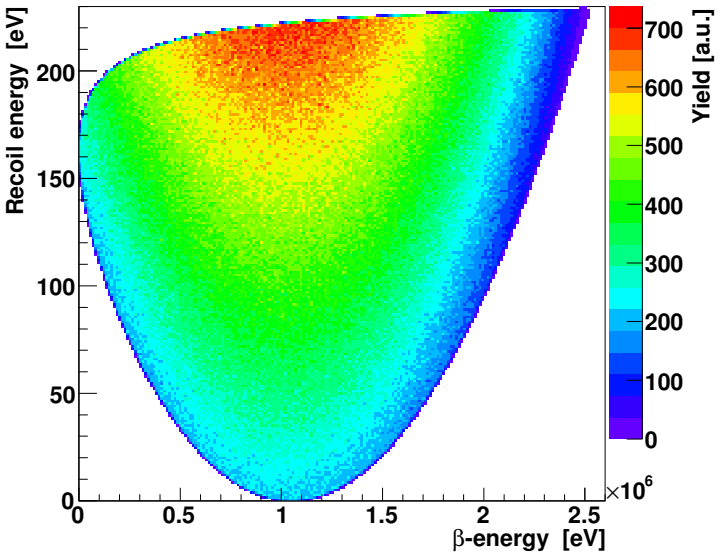

Figure 3.1: *The recoil energy vs. the β energy.* 10^7 *events are plotted; a=0.558.*

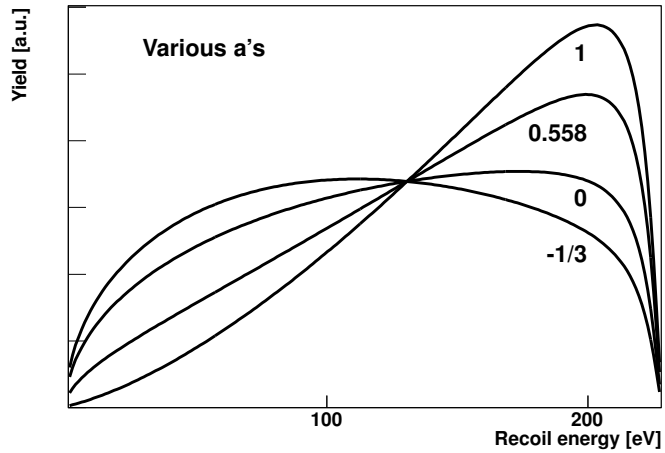

Figure 3.2: *Recoil spectra for different values of a: -1/3 (pure Gamow Teller), 0, 0.558, and 1 (pure Fermi). For larger a the spectrum peaks towards higher energies.*

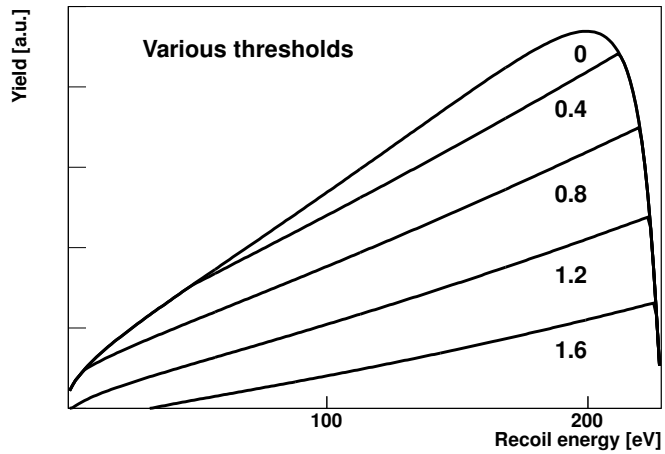

Figure 3.3: *Recoil spectra for different values of the β-energy thresholds (in MeV); a=0.558.*

in section 3.3 we find a similar expression for the β-asymmetry parameter A. From Eq. (3.3) it can be seen that Eq. (3.4) is an approximation.

Number of decays needed

In a real experiment a number of N_d decays occur in the MOT of which a certain fraction ε_tot leads to counts in the recoil-ion spectrum:

$$\frac{N_\mathrm{s}}{N_\mathrm{d}} \equiv \varepsilon_\mathrm{tot}, \tag{3.5}$$

where N_s is the number of counts in the spectrum. Three methods to extract a from recoil-ion spectra will be discussed below. The specifics of obtaining ε_tot depends on whether a β hit or the detection of a shake-off electron (see below) is used as an event trigger:

$$\varepsilon_\mathrm{tot} = \begin{cases} \varepsilon_\beta^\mathrm{sim}\varepsilon_\mathrm{MCP}\varepsilon_\mathrm{charge}, & \text{using β detection} \\ \varepsilon_\mathrm{s.o.}\varepsilon_\mathrm{MCP}\varepsilon_\mathrm{charge}, & \text{using shake-off detection.} \end{cases} \tag{3.6}$$

The efficiencies introduced above are the ion detection efficiency by the MCP, ε_MCP and the loss due to the charge state distributions of the recoil ion following the decay [35], $\varepsilon_\mathrm{charge}$ (neutral recoils can not be detected efficiently). We also consider the detection of electrons freed by the β decay (shake-off electrons). In the work of Vetter *et al.* [36], this proved to be an efficient detection method to measure a. $\varepsilon_\mathrm{s.o.}$ denotes the corresponding electron-detection efficiency.

Lastly we need to know the *required* number of events in the spectrum for a certain fit precision. We assume the following scaling of the precision, α_a, with the number of events in the spectrum

$$\alpha_a \equiv \frac{\sigma_a}{a} \propto \frac{1}{\sqrt{N_\mathrm{s}}}. \tag{3.7}$$

or

$$\alpha_a^\mathrm{needed}\sqrt{N_\mathrm{s}^\mathrm{needed}} = \alpha_a^\mathrm{sim}\sqrt{N_\mathrm{s}^\mathrm{sim}}. \tag{3.8}$$

Combining Eq. (3.5) and (3.8) gives the required number of decays in the MOT

$$N_d^\mathrm{needed} = \left(\frac{\alpha_a^\mathrm{sim}}{\alpha_a^\mathrm{needed}}\right)^2 \frac{N_s^\mathrm{sim}}{\varepsilon_\mathrm{tot}}, \tag{3.9}$$

where ε_tot is the combined efficiency from Eq. (3.6).

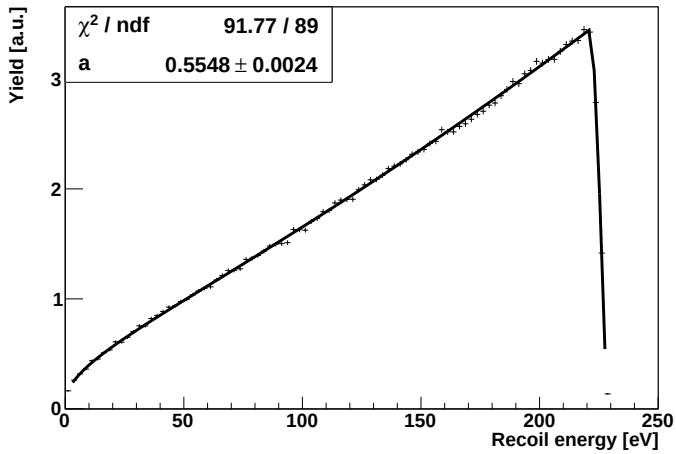

Figure 3.4: *A simulated recoil spectrum with an analytical fit function. The β threshold is set to 1.0 MeV.* 5.58×10^5 *out of* 10^6 *events are above threshold.*

Fitting to the recoil energy spectrum

By using a β detector to generate an event trigger, the decays with β's below the detector threshold are discarded. This is incorporated in Eq. (3.3) by E_{min}. In Fig. 3.3 the effect of a β threshold is shown. From Fig. 3.1 it can be understood why the high- and low-energy end of the recoil spectrum are not affected (at not too high a threshold). Fig. 3.4 shows the simulated recoil energy spectrum where a β-energy threshold of 1.0 MeV is applied. The precision in the fitted value of a is 0.4% for 5.58×10^5 events in the spectrum.

So far no imperfections were taken into account. For example, the cloud of trapped atoms has a finite size. When E_r is calculated from the TOF and the hit position, a particular decay location is assumed, which results in a distorted spectrum when the decay is not occurring at that location. A MOT-size of 0.5 mm (σ) causes a significant deviation in the inferred value of a. However, if the size of the cloud is known, an alternative fit procedure can be used.

Because the recoil spectrum, Eq. (3.3), is of the form

$$R(E_r; a) = f(E_r) + ag(E_r), \tag{3.10}$$

i.e. linear in a, a spectrum with *any* value of a can be written as a linear

Efficiency due to		size
Acceptance β detector	$\varepsilon_{\beta}^{\mathrm{sim}}$	2.2×10^{-2}
Ion detection MCP	$\varepsilon_{\mathrm{MCP}}$	0.5
80% neutral recoils	$\varepsilon_{\mathrm{charge}}$	0.2 [35]
Shake off detection	$\varepsilon_{\mathrm{s.o.}}$	0.15 [37]

Table 3.2: *The efficiencies that are relevant for the determination of the number of decays we need in the MOT for a measurement of a.*

combination of *any* two spectra $R(E_r; a_1)$ and $R(E_r; a_2)$, with $a_1 \neq a_2$:

$$\frac{A \cdot R(E_r; a_1) + B \cdot R(E_r; a_2)}{A + B} = R(E_r; \frac{Aa_1 + Ba_2}{A + B}). \tag{3.11}$$

In particular, choosing $a_1 = 1$ and $a_2 = 0$, giving

$$R_{fit}(E_r) = a \cdot R(E_r; 1) + (1 - a) \cdot R(E_r; 0), \tag{3.12}$$

is convenient since the fit parameter a represents the value of the β-ν correlation parameter a. When imperfections are introduced, events at an initial energy (E_0) are distributed over the energy spectrum given by a function $H(E_r; E0)$. The resulting spectrum is given by folding R with H:

$$\begin{aligned} \tilde{R}(E_r; a) &\equiv \int_0^{E_{\max}} dE_0 \, R(E_0) H(E_r; E_0) \\ &= \int_0^{E_{\max}} dE_0 \, [f(E_0) + a g(E_0)] H(E_r; E_0) \\ &= \tilde{f}(E_r) + a\tilde{g}(E_r). \end{aligned} \tag{3.13}$$

In practice one creates two simulated spectra taking into account the effect of the non-perfect circumstances (earlier represented by $H(E_r; E_0)$); one with $a = 0$ and one with $a = 1$. The relative weight of the two spectra that produces the best fit to a measured (or in this case simulated) spectrum gives the value of a; see Eq. (3.12).

Since the effect of any distortion is described by Eq. (3.13), it is possible to use two 'base-histograms' to fit the data with multiple distortions at once. Fig. 3.5 shows the result of this procedure. A threshold for the β detector, shown in Fig. 6.2a, and a finite MOT size are assumed in creating this spectrum.

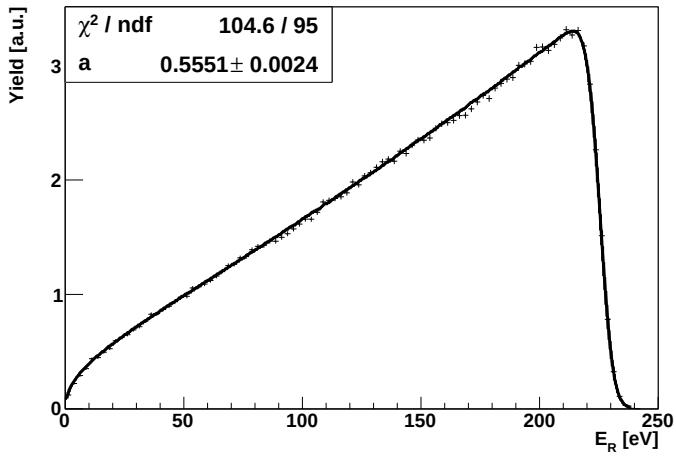

Figure 3.5: *A simulated recoil spectrum fitted with a M.C.-generated function (Eq. (3.13)).* 10^6 *events were simulated,* 5.55×10^5 *of which are in the spectrum; the* β *threshold is set to* 1.0 *MeV and the MOT size is 0.5 mm.*

The required number of decays follows from Eq. (3.9). We use the value og σ_a/a of the spectrum displayed in Fig. 3.5: $\alpha_a^{\rm sim} = 4.3 \times 10^{-3}$. The number of counts in the spectrum is $N_{\rm s}^{\rm sim} = 5.55 \times 10^5$ and $\varepsilon_{\rm tot} = \varepsilon_\beta^{\rm sim}\varepsilon_{\rm MCP}\varepsilon_{\rm charge} = 2.2 \times 10^{-3}$ (see table 3.2) so that the required number of decays in the MOT for a 0.8% measurement of a is

$$N_d^{\rm needed} \simeq 7 \times 10^7 \qquad \text{(fitting to } E_r \text{ spectrum)}. \tag{3.14}$$

Fitting to the TOF spectrum

As an alternative measuring method one can fit to the TOF spectrum of the recoils, using only part of the event information, its shape depends on a as well. The argument used in Eq. (3.13) can be extended. A suitable function transforms the recoil energy spectrum in a TOF spectrum in which a enters linearly. The TOF spectrum can therefore be fitted in the same way, using two base histograms. The current design of the setup uses a β-particle hit on the β detector as an event trigger. This means that only events with β particles flying away from the recoil detector go in the spectrum, selecting mainly recoil

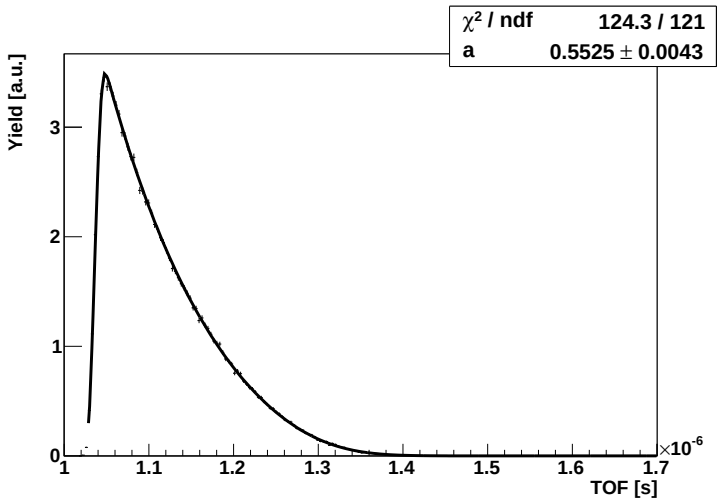

Figure 3.6: *A simulated TOF spectrum with a M.C.-generated fit function. The MOT size is 0.5 mm and β threshold* 1.0 *MeV.* 2.44×10^5 *of the* 10^7 *simulated events were detected by the β detector and are in the spectrum.*

ions with a small TOF (see Fig. 3.6). In this case $\alpha_a^{\rm sim} = 8 \times 10^{-3}$, the number of counts in the spectrum is $N_s^{\rm sim} = 2.44 \times 10^5$ and $\varepsilon_{\rm tot} = \varepsilon_\beta^{\rm sim} \varepsilon_{\rm MCP} \varepsilon_{\rm charge} = 2.2 \times 10^{-3}$ (see table 3.2) so that the required number of decays in the MOT is

$$N_d^{\rm needed} \simeq 1 \times 10^8 \qquad \text{(TOF β trigger)}. \tag{3.15}$$

In [14] a different event trigger was used: the low energy electrons shaken off in the β-decay process were guided by an electric field and collected on a second MCP. In this way there is no directional bias and a different TOF spectrum is produced. The advantage is that one is not limited anymore by the solid angle and threshold of the β detector $\varepsilon_\beta^{\rm sim} = 2.2 \times 10^{-2}$, but by the shake off detection efficiency, taken to be $\varepsilon_{\rm shake} = 0.15$ [37]. However, the spectrum in Fig. 3.7 has less sharp features leading to a larger relative error for a given number of detected events in the spectrum. Summarizing

$$N_d^{\rm needed} \simeq 9 \times 10^7 \qquad \text{(TOF shakeoff trigger)}. \tag{3.16}$$

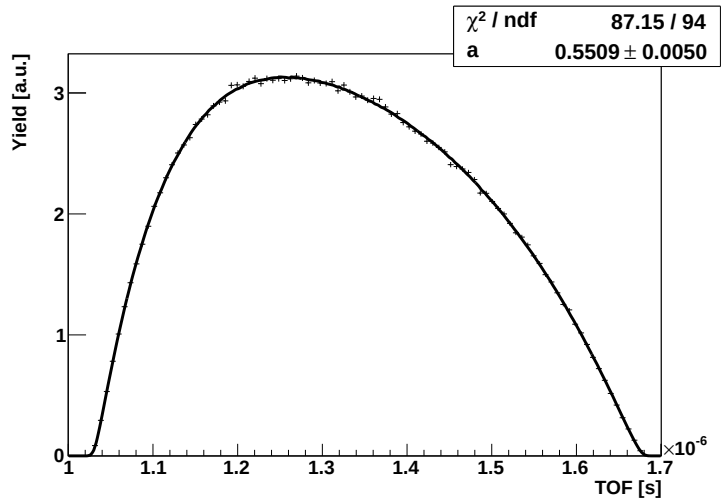

Figure 3.7: *A simulated TOF spectrum with a M.C.-generated fit function. The MOT size is 0.5 mm and β threshold* 1.0 *MeV. All of the* 10^6 *simulated events are in the spectrum.*

3.2.2 Systematic effects

Procedure

In the simulation a single setup parameter x can be changed by an amount Δx, while keeping all the others fixed. If the fit value of a changes by Δa, the number of interest is $\frac{\Delta a}{\Delta x}$, the sensitivity of a to the parameter x.

This is done is as follows. In the fitting procedure we make use of two base histograms, one where $a = 0$ and one where $a = 1$. These histograms are constructed by simulating a large number of events. Numerical values of several parameters need to be inserted. These parameters are the size of the MOT cloud (r, the σ of a 3D Gaussian distribution), the position of the MOT cloud (x, y, z), and the energy threshold of the β detector (T). Suppose the base histograms are produced using the values r_0, x_0, y_0, z_0, and T_0. If the measured spectrum is taken under nearly the same conditions, but with corresponding parameters $r_0 + \Delta r$, $x_o + \Delta x$, etc., one can still use the base histograms, but the value of a is shifted.

How to correct for this shift can be found using the simulation itself. One

produces a 'measured' spectrum with one of the parameters changed with respect to the base histogram value. The resulting change in the fitted value of a gives the sensitivity of a to the parameter that was varied. This is shown in the '$\Delta a/a$' column of the tables 3.3-3.5. Due to symmetry Δa depends to lowest order quadratically on Δx and Δy.

A measurement error in Δr, etc., causes an uncertainty in the resulting shift and hence a systematic error in a. The maximally allowed uncertainty in the shift in order to satisfy $\Delta a/a < 1\%$ is indicated in the last column of the tables. Put differently, the last column gives the precision at which the setup parameter should be known.

Table 3.3 summarizes the results for fitting to the recoil energy E_r. The results for TOF spectrum fits can be found in tables 3.4 and 3.5 for β-detector selected events and an unbiased selection, respectively.

Discussion

The systematic error due to uncertainty in the β-energy threshold is roughly the same in all three cases. It should be known to 10 keV precision or better to have a systematic uncertainty smaller than 1%. The claimed precision found in [38], for a detector with a less complex design, would be high enough for our purposes. When using the TOF spectra, more accurate knowledge of the z-position (the MCP is on the z-axis) is needed. An advantage of using TOF spectra is that uncertainties in position in the xy plane are unimportant since they do not influence the TOF.

We consider two systematic effects related to the time of flight. They were not simulated but can be deduced from other shifts. The first is due to an offset in the TOF which is approximately equivalent to a shift Δz of the MOT in the z direction. From the expression

$$\mathrm{TOF} = T_0 + \frac{1}{\sqrt{v_{z,0}^2 + 2aL}}\Delta z + ... \tag{3.17}$$

it can be seen that the shift in the TOF depends on the initial v_z so the shape of the TOF spectrum will be distorted by a shift in the z direction. However, since $v_z^2/(2aL)$ is maximally 1/10, we will ignore this effect and regard the two shifts equivalent. One can be transformed in the other by

$$\Delta z \to 0.18\mathrm{mm/ns} \cdot \Delta\mathrm{TOF} \qquad (\mathrm{TOF\ in\ ns}). \tag{3.18}$$

Systematic effect	Units	$\Delta a/a$	Max. uncertainty
MOT position	(x or y in mm)	$-2 \times 10^{-2}(\Delta x)^2$	0.5 mm
MOT position	(z in mm)	$-9 \times 10^{-3}\Delta z$	1.1 mm
MOT size	(r in mm)	$-7 \times 10^{-2}\Delta r$	0.14 mm
β threshold	(T in keV)	$9 \times 10^{-4}\Delta T$	11 keV
TOF offset	(t in ns)	$-0.2 \times 10^{-3}\Delta t$	5 ns

Table 3.3: *Systematic shifts in a for fit to E_r-spectrum. The last column shows the maximally allowed uncertainty of the shift for a 1% precision of a.*

The second effect is due to the resolution of the TOF which leads to a small broadening of the spectrum. Following the argument above this is (approximately) equivalent to a spread in the initial z position of the ions. This was not simulated but instead we can use the simulated finite MOT size. This can only be done for the fits to the TOF spectra because then the spread in initial x and y position are not relevant. Eq. (3.17) can be applied here as well.

Analogously, the position resolution of the MCP introduces an uncertainty in the hit position which is equivalent to an uncertainty in the xy position of the MOT; no numerical factor is needed to translate one into the other.

Comparing the three tables 3.3-3.5 we see that the E_r-fit method is comparable to the TOF measurement using shake-off electrons. The third method, using the β-detector, demands extremely accurate knowledge of the z-position making the other two preferably. The E_r type of measurement requires the use of the β detector as well as a hit-position measurement of the recoil ion, which is also the case for a measurement of D. So, apart from the need for a polarized sample, a D measurement requires the same setup as the E_r-fit measurement of a, making this the more favorable choice.

3.3 β-Asymmetry measurement (A)

From Eq. (3.1) it can be seen that a polarized sample is needed. The term containing $\mathbf{J} \cdot \mathbf{p}_e$ causes a beaming of the electrons along the direction of the spin. This parity violating term was first measured by Wu [3]. Suppose that $\mathbf{J}$ is parallel to $\hat{z}$ and that a cylindrical β detector is placed at some distance from the sample on the positive z axis. The amount of β's measured in the direction

Systematic effect	Units	$\Delta a/a$	Max. uncertainty
MOT position	(z in mm)	$-3 \times 10^{-1} \Delta z$	$3.3 \cdot 10^{-2}$ mm
MOT size	(r in mm)	$-8 \times 10^{-2} \Delta r$	0.13 mm
β threshold	(T in kev)	$1 \times 10^{-3} \Delta T$	10 keV
TOF offset	(t in ns)	$-5 \times 10^{-2} \Delta t$	0.2 ns
TOF resolution	(t in ns)	$-1 \times 10^{-2} \Delta t$	0.7 ns

Table 3.4: *Systematic shifts in a for a fit to TOF-spectrum using a biased sample by β-detector selection.*

Systematic effect	Units	$\Delta a/a$	Max. uncertainty
MOT position	(z in mm)	$-7 \times 10^{-2} \Delta z$	0.14 mm
MOT size	(r in mm)	$-4 \times 10^{-3} \Delta r$	2.5 mm
β threshold	(T in keV)	$1 \times 10^{-3} \Delta T$	10 keV
TOF offset	(t in ns)	$-1 \times 10^{-2} \Delta t$	0.8 ns
TOF resolution	(t in ns)	$-7 \times 10^{-4} \Delta t$	14 ns

Table 3.5: *Systematic shifts in a for a fit to TOF-spectrum using an unbiased sample (shake-off detection).*

(anti-)parallel is N_+ (N_-), which can be written as

$$N_\pm = \text{const} \times \int dV\, \rho(E_e)\,(1 + a' + b' \pm PA')\,. \tag{3.19}$$

where we use the notation

$$a' = a\frac{\mathbf{p}_e \cdot \mathbf{p}_\nu}{E_e E_\nu}, \qquad b' = b\frac{m_e}{E_e}, \qquad A' = A\frac{\mathbf{j} \cdot \mathbf{p}_e}{E_e}. \tag{3.20}$$

Further,

$$\rho(E_e) = p_e E_e (Q + m_e - E_e)^2 \xi \qquad \text{and} \tag{3.21}$$
$$\int dV = \int_{\beta-\text{cut}} dE_e d\Omega_e \int_{\text{all}} d\Omega_\nu.$$

Then

$$R_A \equiv \frac{N_+ - N_-}{N_+ + N_-} \tag{3.22}$$
$$= P\frac{\int dV\, \rho(E_e) A'}{\int dV\, \rho(E_e)\,(1 + b')}. \tag{3.23}$$

Thus, the parity-even terms drop out in the denominator while the parity-odd terms drop out in the numerator. Introducing a shorthand notation for averaging over measured data

$$\langle Q \rangle \equiv \int dV\, \rho(E_e) Q / \int dV\, \rho(E_e), \tag{3.24}$$

the asymmetry R_A can be written as

$$\begin{aligned} R_A &= P\frac{A}{1 + b\left\langle \frac{m_e}{E_e} \right\rangle} \left\langle \frac{\mathbf{j} \cdot \mathbf{p}_e}{E_e} \right\rangle \\ &\equiv P\frac{A}{1 + b\left\langle \frac{m_e}{E_e} \right\rangle} K_A \\ &\equiv P\tilde{A}K_A \end{aligned} \tag{3.25}$$

Note that $\tilde{A}$ is A corrected for the contribution of the Fierz term b. However, in the following we refer to $\tilde{A}$ as A. The number K_A is the analyzing power; it

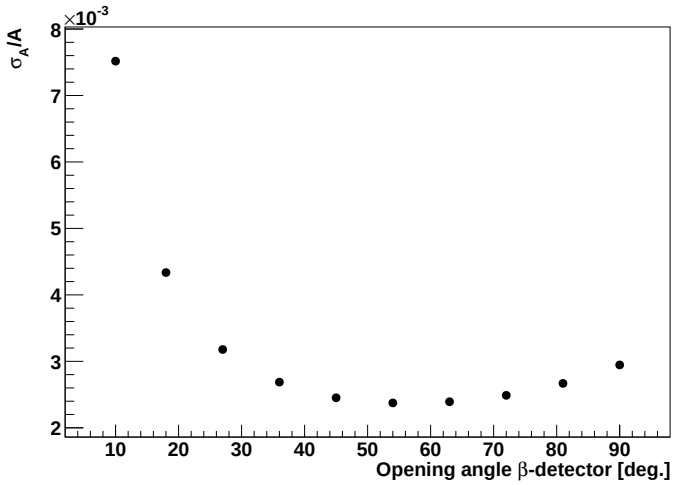

Figure 3.8: *σ_A/A vs detector opening angle.*

determines the sensitivity of R_A to A. It can be calculated by a simulation of the experiment. Since N_+ and N_- are uncorrelated the statistical error in R_A is given by

$$\sigma_{R_A} = 2\sqrt{\frac{N_+ N_-}{(N_+ + N_-)^3}} \tag{3.26}$$

The relative error σ_A/A is calculated as a function of the opening angle of the β detector. In Fig. 3.8 σ_A/A is shown as a function of opening angle. It can be seen that the optimum is around 55°. Fig. 3.9 shows σ_A/A as a function of the β threshold at a fixed opening angle of 55°. The optimum at ~ 0.2 MeV is lower than the detector threshold that is foreseen in our setup.

It should be noted that in the previous paragraph σ_{R_A}/R_A was calculated rather than σ_A/A. From Eq. (3.25) it follows that

$$\left(\frac{\sigma_A}{A}\right)^2 = \left(\frac{\sigma_{R_A}}{R_A}\right)^2 + \left(\frac{\sigma_P}{P}\right)^2 + \left(\frac{\sigma_{K_A}}{K_A}\right)^2. \tag{3.27}$$

This means that the degree of polarization as well as K_A need to be known to better that 1% for a 1% measurement of A. There are several ways to measure

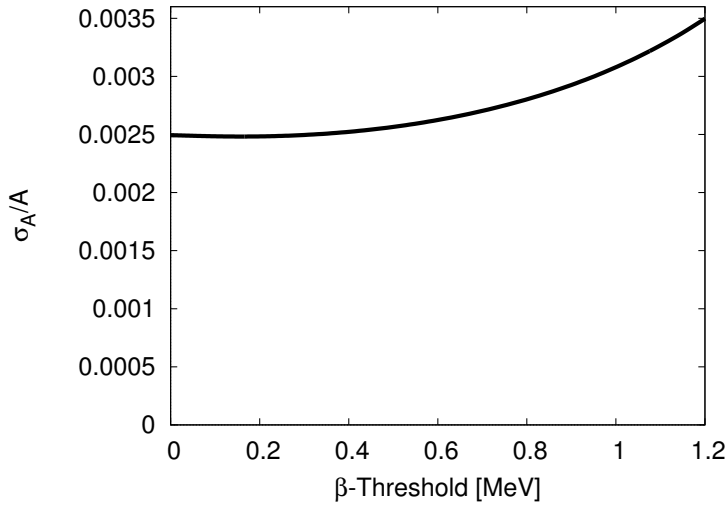

Figure 3.9: *σ_A/A vs β threshold.*

P. If the nucleus decays to an exited state, an asymmetry in the emitted gamma rays can be measured to quantify P. For example, for ^{60}Co $\sigma_P/P = 4 \times 10^{-3}$ was achieved [21]). A different approach is described in [39], where in the ^{37}K experiment the population of one of the magnetic substates of the ground state is probed by an ionizing laser ($\sigma_P/P = 2 \times 10^{-3}$).

Number of decays needed

Given $N_\pm$ in an $N = 10^6$ simulation and the resulting R_A and σ_{R_A} the number of decays in the MOT needed for a 0.6‰ statistical accuracy is

$$N \simeq 20 \left(\frac{\sigma_A}{A}\right)^{-2} = 6 \times 10^7. \tag{3.28}$$

This is including a smooth β detector threshold at 1 MeV and a realistic detection solid angle of 4.5% corresponding to an opening angle of 25°.

Systematic effect	Units	$\Delta A/A$	Max. uncertainty
MOT position	(x or y in mm)	$-8 \times 10^{-4}(\Delta x)^2$	0.87 mm
MOT position	(z in mm)	$-4 \times 10^{-3}\Delta z$	0.15 mm
MOT size	(r in mm)	$-2 \times 10^{-3}\Delta r$	0.30 mm
Spin alignment	(θ in °)	$-1.5 \times 10^{-4}(\Delta\theta)^2$	2.0°
β threshold	(T in keV)	$3 \times 10^{-5}\Delta T$	17 KeV

Table 3.6: *Systematic shifts in A. The last column shows the maximum allowed uncertainty for a* 0.6‰ *measurement.*

3.3.1 Systematic effects

Procedure

In table 3.6 we explore the sensitivity of A on systematic effects. The way to interpret the table is explained in section 3.2.2. The procedure is slightly different since there is no fitting involved here. For some reference point in the parameter space the value of R_A was determined. Varying a single parameter results in a different value: $R_A + \Delta R_A$. We identify $\Delta R_A/R_A = \Delta A/A$.

Discussion

We consider position and size of the atom cloud, and the β threshold. Due to the symmetry of the system, $\Delta A/A$ depends quadratically on shifts of the MOT position in the xy plane. The TOF is not considered here since it does not play a role. The knowledge of the threshold in this case needs to be of about the same precision as for an $\tilde{a}$ measurement. It was noticed already in the discussion following Eq. (3.27) that σ_P/P needs to be known at least as accurate as the desired precision σ_A/A.

3.4 Measurement of time-reversal violation, D coefficient

For a measurement of D we need to consider the triple correlation

$$\mathbf{J} \cdot \frac{\mathbf{p}_e \times \mathbf{p}_\nu}{E_e E_\nu} = \mathbf{J} \cdot \frac{\mathbf{p}_r \times \mathbf{p}_e}{E_e \sqrt{p_r^2 + p_e^2 + \mathbf{p}_r \cdot \mathbf{p}_e}}. \tag{3.29}$$

The experiment requires a coincidence measurement between recoils and β particles with a spin polarized sample. Since the experiment is performed in the rest frame of the nucleus we can substitute $\mathbf{p}_\nu = -\mathbf{p}_r - \mathbf{p}_e$. One needs to measure coincidences between the β and recoil particles at relative angle θ_{er} where this term is large. If the spin is in the $\hat{z}$-direction, this term is maximal if both $\mathbf{p}_r$ and $\mathbf{p}_e$ are in the xy plane. Fig. 3.10 shows an example detector geometry that is suitable for a D-measurement as will be shown below. The β detector is placed on the x-axis ($\phi = 0$) and two recoil detectors are placed symmetrically around it at $\phi = \pm\theta_{er}$. The number of coincident events between the β detector and the right (left) recoil detector $C_\pm^{R(L)}$ where the $\pm$ sign again indicates the spin polarization direction. $C_\pm^{R(L)}$ is given by (for notation see Eq. (3.20))

$$C_\pm^{R(L)} = \text{const} \times \int_{R(L)} dV\, \rho(E_e)\, [1 + a' + b' + c' \pm P\,(A' + B' + D')] \quad (3.30)$$

with

$$\begin{aligned} \rho(E_e) &= p_e E_e (Q + m_e - E_e)^2 \xi, \\ \int_{R(L)} dV &= \int_{\text{thr.}} dE_e \int_{\Omega_{R(L)}} d\Omega_e\, d\Omega_\nu. \end{aligned} \quad (3.31)$$

The integration region $\Omega_{R(L)}$ is such that both the β- and the right (left) recoil detector are hit. We define

$$\begin{aligned} R_D^{R(L)} &\equiv \frac{C_+^{R(L)} - C_-^{R(L)}}{C_+^{R(L)} + C_-^{R(L)}} \\ &= P \frac{\int_{R(L)} dV\, \rho(E_e)\, (A' + B' + D')}{\int_{R(L)} dV\, \rho(E_e)\, (1 + a' + b' + c')} \\ &\equiv P(A K_A^{R(L)} + B K_B^{R(L)} + D K_D^{R(L)}). \end{aligned} \quad (3.32)$$

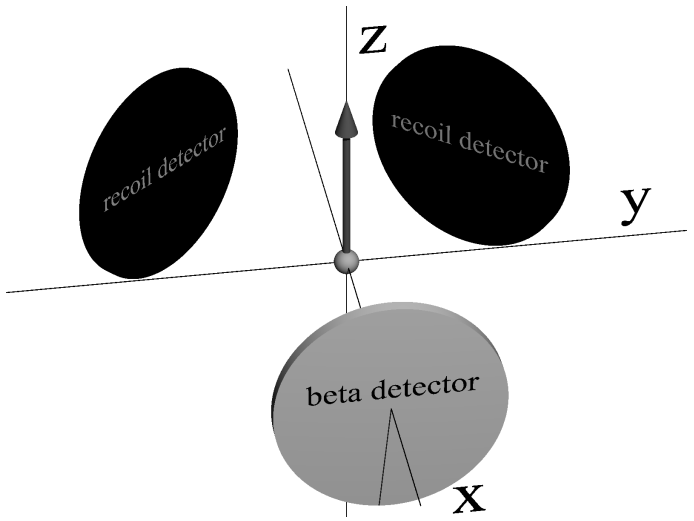

Figure 3.10: *Detector setup of a measurement of D. The arrow indicates the polarization of the sample.*

For the cancellation of the terms proportional to the degree of polarization P in the denominator, it is important that the spin flip is very precise. Defining[2]

$$K_A^{R(L)} \equiv \frac{\int_{R(L)} dV\, \rho(E_e)\, (\mathbf{j} \cdot \mathbf{p}_e/E_e)}{\int_{R(L)} dV\, \rho(E_e)\, (1 + a' + b' + c')} \tag{3.33}$$

$$K_B^{R(L)} \equiv \frac{\int_{R(L)} dV\, \rho(E_e)\, (\mathbf{j} \cdot \mathbf{p}_\nu/E_\nu)}{\int_{R(L)} dV\, \rho(E_e)\, (1 + a' + b' + c')} \tag{3.34}$$

$$K_D^{R(L)} \equiv \frac{\int_{R(L)} dV\, \rho(E_e)\, (\mathbf{j} \cdot (\mathbf{p}_e \times \mathbf{p}_\nu)/(E_e E_\nu))}{\int_{R(L)} dV\, \rho(E_e)\, (1 + a' + b' + c')}. \tag{3.35}$$

The symmetry of the setup is such that

$$K_A^R = K_A^L, \qquad K_B^R = K_B^L, \qquad K_D^R = -K_D^L, \tag{3.36}$$

and the D-term can be isolated

$$v_D \equiv R_D^R - R_D^L = 2PDK_D^R. \tag{3.37}$$

[2]When actually calculating these constants by simulation one can take the SM-values of a, b and c, see the remark below Eq. (3.37).

At this point we could define a $\tilde{D}$, similar to $\tilde{A}$ in Eq. (3.25), to incorporate non-SM values of a, b and c. However, since D is in lowest order linear in the non-SM couplings, we have in first order $\tilde{D} = D$.

The quantity v_D can be determined from a measurement and K_D^R from a Monte Carlo simulation. The statistical error in v_D is

$$\begin{aligned}\sigma_{v_D}^2 &= \frac{4C_+^R C_-^R}{(C_+^R + C_-^R)^3} + \frac{4C_+^L C_-^L}{(C_+^L + C_-^L)^3} \\ &\simeq \frac{1}{C},\end{aligned} \tag{3.38}$$

where in the second line it is used that all coincident rates will be approximately the same[3] (C). The statistical error in D is then

$$\sigma_D = \frac{1}{2PK_D\sqrt{C}} \tag{3.39}$$

From this the number of decays in the MOT N_d that is needed for a significant measurement can be calculated. The total efficiency of the coincidence measurement can be parametrized for our experiment as

$$C = \varepsilon_{\text{tot}} N_d \tag{3.40}$$

$$\begin{aligned}&= \varepsilon_{\text{coin}}^{\text{sim}} \varepsilon_{\text{MCP}} \varepsilon_{\text{charge}} \varepsilon_{\pm} N_d \\ &= 5.0 \times 10^{-2} \varepsilon_{\text{coin}}^{\text{sim}} N_d,\end{aligned} \tag{3.41}$$

where $\varepsilon_{\text{coin}}^{\text{sim}}$ denotes the coincidence acceptance efficiency of the detector setup, including the threshold of the β detector. Further, the efficiency of the MCP $\varepsilon_{\text{MCP}} = 0.5$, the charge state distribution of the recoils $\varepsilon_{\text{charge}} = 0.2$ [35], and having to do a spin up and down measurement $\varepsilon_{\pm} = 0.5$. This gives

$$N_d = \frac{5}{\varepsilon_{\text{coin}}^{\text{sim}} P^2 K_D^2 \sigma_D^2} \tag{3.42}$$

In the following two possible geometries are discussed. The β detector is the same in both cases, so the difference amounts to making different data cuts in the recoil ion data.

[3] This is only the case if the detectors are in the xy plane. In other cases the differences between C_+ and C_- can become significant.

3.4.1 Cylindrical β- and recoil detector

The computations in this section are performed for the geometry shown in Fig. 3.10. All three detectors are 20 cm away from the center and have a 9 cm radius covering a 4.4% solid angle; very comparable to E-detector of of the β telescope. A reason to discuss this particular geometry is because it gives some insight in the relation between sensitivity (K_D) and statistics (C).

Define θ_{er} as the angle at which the recoil detectors are placed. Fig. 3.11 shows how K_D depends on θ_{er}. The dominating behavior comes from the cross product, as can be seen from the sine function fitted to the calculated curve (for comparison only). In Fig. 3.12 it can be seen that much more β-recoil coincidences are collected at (larger C) at higher θ_{er}. Finally, in Fig. 3.13 the combined effect on σ_D (Eq. (3.39)) is shown in the $K_D\sqrt{C}$ plot. The smallest error is obtained at an angle of 140°, at which $K_D^R = 0.61$ and $\varepsilon_{\text{coin}}^{\text{sim}} = 2.3\times10^{-3}$ so that from Eq. (3.42) the required total number of decays in the MOT is

$$N_d = \frac{6\times10^3}{\sigma_D^2} \tag{3.43}$$

For a precision of $\sigma_D = 4\times10^{-4}$ one would require 4×10^{10} decays.

The estimated error in D from Eq. (3.39) was checked for this particular geometry by calculating v_D and D for 200 pairs of spin up and down measurements with 10^6 simulated events (corresponding to $N = 1\times10^7$ or $C = 4.6\times10^3$). D was set to zero and a zero threshold was used which should give $\sigma_D = 1.2\times10^{-2}$. The resulting values of D show a sigma of 1.0×10^{-2}. The same was done for $D = 0.1$, and resulted in a sigma of 1.1×10^{-2}.

3.4.2 Round β detector and 4π position sensitive recoil detection

The above analysis is based on two cylindrical recoil detectors. Our setup collects all recoils, and they all contribute with various weights to the statistical accuracy of the measurement. The case that will be discussed here is a simple division of the recoil detector in two halves; the two sides of the xz plane. In this arrangement $K_D = 0.38$ and $\varepsilon_{\text{coin}}^{\text{sim}} = 1.1\times10^{-2}$ so that from Eq. (3.42)

$$N_d = \frac{3\times10^3}{\sigma_D^2}, \tag{3.44}$$

leading to $N_d = 2\times10^{10}$ decays for a 4×10^{-4} measurement of D.

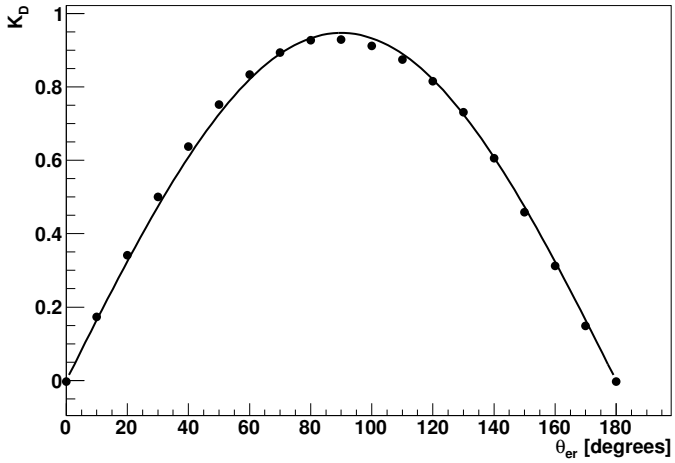

Figure 3.11: *The analyzing power K_D^R (Eq. (3.32)) as a function θ_{er}. The geometry is shown in Fig. 3.10.*

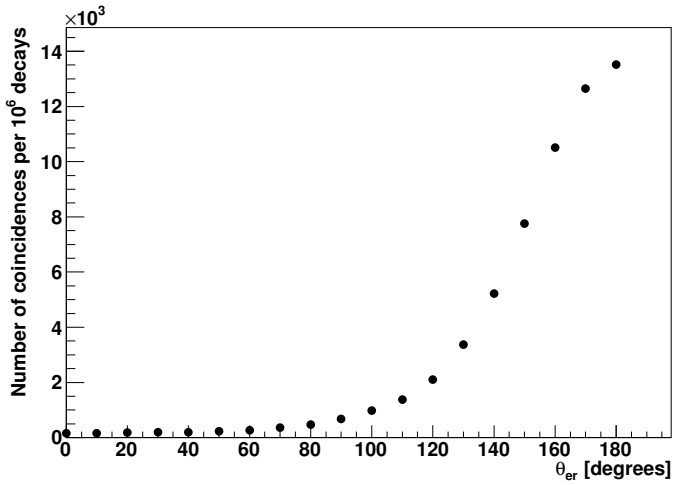

Figure 3.12: *Number of coincidences C as a function θ_{er}. The total number of decays is 10^6 and the geometry is shown in Fig. 3.10.*

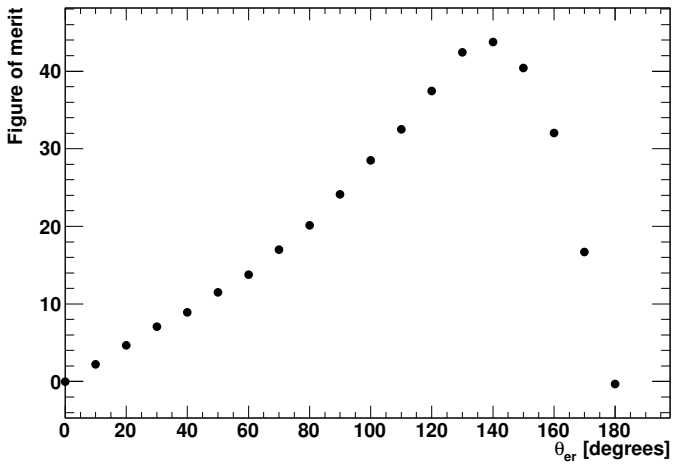

Figure 3.13: *$K_D\sqrt{C} = 1/\sigma_D$ as function of θ_{er}. The geometry is shown in Fig. 3.10.*

One could think of a way to divide the recoil detector in pairs of segments i, each of which results in a K_D^i, C^i and $D^i \pm \sigma_D^i$ from which an average value of D can be calculated. This will lead to a smaller statistical error, but it has not been investigated further.

3.4.3 Systematic effects

Procedure

The way to interpret table 3.7 and 3.8 is explained in section 3.2.2. To calculate the sensitivity of D to the indicated parameters a similar procedure as for A was used. For a reference point in parameter space the value of v_D is determined by simulation. Varying one parameter gives a change of Δv_D. The corresponding change in D is calculated using Eq. (3.37) taking $P = 1$.

Discussion

The systematic effects were studied for two detector geometries. Only the effects that break the left right symmetry of the setup are considered. For example a shift of the MOT position in the z- or x-direction (see Fig. 3.10) would slightly

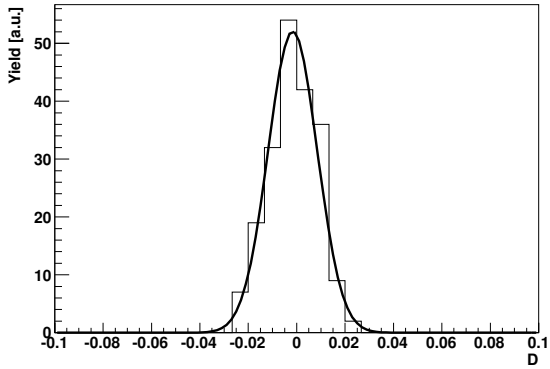

(a) $D = 0$, $\sigma_{\text{fit}} = 1.0 \times 10^{-2}$.

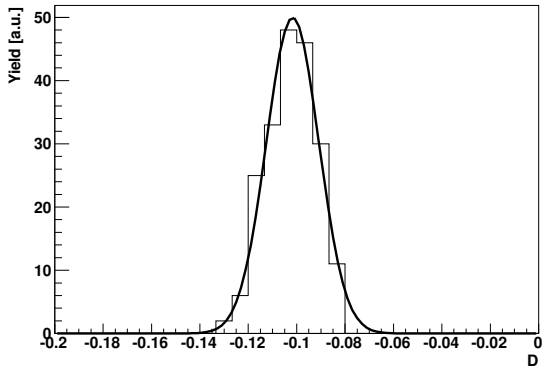

(b) $D = 0.1$, $\sigma_{\text{fit}} = 1.1 \times 10^{-2}$.

Figure 3.14: *200 simulated D-measurements following the method leading to Eq. (3.37). The spread is consistent with Eq. 3.39. The detector arrangement is shown in Fig. 3.10.*

Systematic effect		ΔD	$\Delta D = 1 \times 10^{-4}$
MOT position	(y in mm)	$-5 \times 10^{-5} \Delta y$	2 mm
Spin alignment	(θ in $^\circ$)	$-1.6 \times 10^{-2} (\Delta\theta)^2$	0.08°

Table 3.7: *Systematic shifts in D when using cylindrical recoil detectors (see Fig. 3.10).*

Systematic effect		ΔD	$\Delta D = 1 \times 10^{-4}$
MOT position	(y in mm)	$-9 \times 10^{-6} \Delta y$	11 mm
Spin alignment	(θ in $^\circ$)	$-1.4 \times 10^{-2} (\Delta\theta)^2$	0.09°

Table 3.8: *Systematic shifts in D when using 2 2π detectors.*

change the coincidence rates, but it will not introduce an asymmetry between left and right, so that the cancellation in Eq. (3.37) still takes place. As a consequence of such a shift in the z- or x-direction the value of K_D will be slightly off, but since we are not interested in many digits but in an upper bound on the value of D, this is not very relevant. In principle we do not need to know the degree of polarization, P, very precisely for the same reason. However, as was noted below Eq. (3.32), the spin flip should be very precise. At first sight the situation is different for shifts in the y direction. However, the value of D is rather robust and not very sensitive to MOT displacements in this direction.

3.5 Conclusions

In this chapter we discussed a Monte Carlo simulation of the experiment. It does not yet contain enough detail to perform data analysis of a real experiment. It was used as a tool to explore the statistical and systematic aspects of several types of measurements. We discussed the β-ν correlation parameter (a), the β-asymmetry parameter (A) and the time-reversal violating D-term. For all three cases we described the concept of a measurement, the number of events that is needed to reach a certain statistical error and some systematic effects.

Summarizing:

- a: Using an unpolarized sample one measures the recoils (E_r or TOF) and

fits to the spectrum. Different scenarios were discussed and the number of decays needed for a 1% measurement is calculated:

1) E_r spectrum, $N = 7 \times 10^7$,

2) TOF spectrum, unbiased sample, shake-off electrons, $N = 9 \times 10^7$,

3) TOF spectrum, β detector as a trigger. $N = 1 \times 10^8$.

- A: Using a polarized sample and a β detector one measures the asymmetry in β particles emitted parallel and anti-parallel to the spin. For a 1% accuracy one needs 2×10^5 decays in the MOT.

- D: Using a polarized sample, a β detector and two recoil detectors (i.e. cuts in recoil ion data) one measures β-recoil coincidences. Two scenarios were discussed and the required numbers of decays N for 10^{-4} measurement of D were calculated:

  1) Two cylindrical recoil detectors (Fig. 3.10), $N = 4 \times 10^{10}$

  2) Two 2π recoil detectors, $N = 2 \times 10^{10}$

  It was noted that a suitable segmentation of the data can lead to a smaller error for a given number of events. This needs more investigation.

CHAPTER 4

Experimental setup

The lifetime of ^{21}Na of 32 s requires it to be produced continuously during the experiment. The TRIμP facility was developed to produce a range of radioactive beams for several experiments of the TRIμP group or for external users. The AGOR cyclotron can deliver ion beams ranging from protons to lead ions. When these beams hit a target a secondary beam of reaction products is formed. The secondary beam is separated from the primary beam on basis of its magnetic rigidity in the separator. The beam particles are slowed down in several stages to end in the experimental setup where they are neutralized and trapped in a collector MOT. A push beam transports them to a low background environment in the decay chamber where the atoms are trapped again in a second MOT.

There are several reasons to have a double-MOT setup, i.e. to have a separate chamber where the decay kinematics are studied: the requirements for efficient trapping on the one hand and the final measurement on the other are not compatible. For efficient trapping of atoms from a vapor background the atoms need to spend as much time as possible in the laser beams. Therefore, one uses a trapping cell with dimensions comparable to the trapping-laser beam diameter, leaving no room for a β-particle detector and a reaction microscope for ion detection. These are placed in the second chamber where also the large background from non-trapped radioactive atoms can be avoided.

In this chapter the main components of the setup are discussed. The chapter is split into three parts: production and transport, the double-MOT system, and the detection system. Fig. 4.1 gives an overview of the components discussed in this chapter.

4.1 Production and transport of ^{21}Na

4.1.1 AGOR cyclotron and TRIμP isotope separator

The superconducting cyclotron (AGOR) delivers the primary beam of $^{20}Ne^{6+}$ ions with an energy of 22.3 MeV per nucleon, with an electrical current up to 1 μA or a flux of 10^{12} particles per second. The primary beam hits a deuterium gas target which is at a pressure of 1.7 atm. ^{21}Na is produced in the reaction $d(^{20}\mathrm{Ne},^{21}\mathrm{Na})n$ in inverse kinematics [40] as indicated with the reaction notation. The target nucleus is much lighter than the projectile so that the reaction product has nearly the same momentum as the projectile. However, the 11+ charge state of the ^{21}Na ion is one higher than the projectile's $^{20}Ne^{10+}$. In practice we find the magnetic rigidity of ^{21}Na to be 8.7% lower than the $^{20}Ne^{10+}$ beam. The reaction products can therefore be separated from the remaining beam and most other reaction products in the TRIμP magnetic separator. For more details on the TRIμP separator we refer to [41, 42].

4.1.2 Thermal Ionizer

The number of ^{21}Na ions delivered by the separator is about 3×10^6/s with a kinetic energy of about 20 MeV/u. They have to be slowed down and neutralized before they can be trapped in the magneto-optical trap. This is done in two steps. In the first step the ions are converted into a 2.8 keV singly charged ion beam by a Thermal Ionizer (TI), and in the second step this beam is implanted in a neutralizer foil in the trapping volume, from which they are released as atoms (section 4.2).

In the TI the ^{21}Na ions are stopped in a stack of tungsten foils inside a tungsten cavity that is heated to a temperature of about 2500 K by electron bombardment. In multiple collisions with the cavity walls and the foils the ions are continuously neutralized and re-ionized. If an ion is near the exit it is extracted from the TI by a 6.5 kV extraction field, and then decelerated to 2.8 keV. The ^{21}Na-ion yield from the TI is about 3×10^5/s so the efficiency is about 10%. At the higher temperature of 2800 K an efficiency of 50% can be

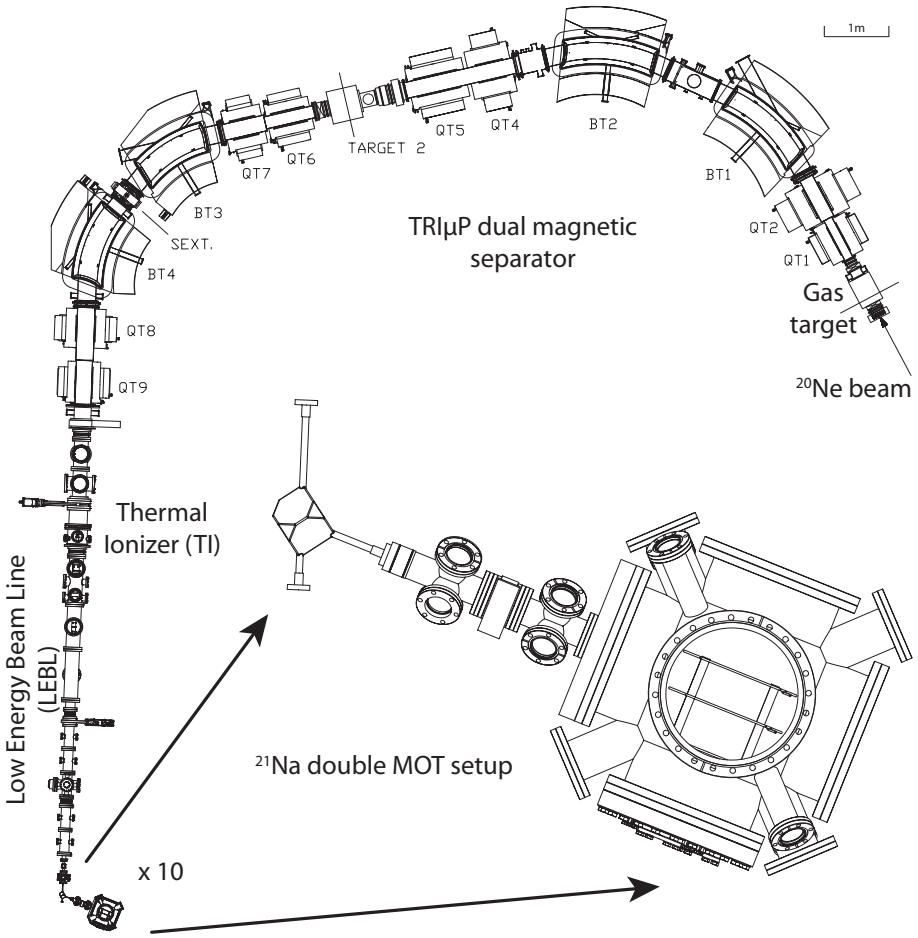

Figure 4.1: *The TRIμP separator, the low energy beam line, and the double-MOT system. The zoom in shows from left to right the collector MOT, the funnel section, and the decay chamber. Figure courtesy of Wilbert Kruithof.*

reached [43]. A more detailed description and characterization of the TI can be found in [43].

4.1.3 Low energy beam line

The 2.8 keV ion beam is transported through the Low Energy Beam line (LEB line) to the trapping cell covering a distance of about 10 m. The cavity of the TI is at ground potential and the ions are accelerated by a -6.5 kV electrode and later slowed down by an electrode at -2.8 kV. In a Wien filter the ^{21}Na is separated from stable isotopes which occur as trace elements in the tungsten foils of the TI. They are emitted with the same energy but have different mass numbers. A drift tube that is switched from -2.8 kV to ground potential while the ions are inside, allows the rest of the setup to be at ground potential. This necessarily introduces a loss of at least 50%, since half of the time the tube is at 0 V, blocking the entrance for incoming particles. Several steering and focusing elements direct the ion beam onto the neutralizer foil inside the trapping cell. The transport efficiency of the LEB line is 20(10)% [44] so that a yield of about 5×10^4 ^{21}Na ions/s is realized.

4.2 Double-MOT system

For a measurement of the time-reversal violating D coefficient we need to detect both the β particle and the recoiling daughter nucleus. The low recoil energy, with an endpoint of 229 eV, excludes the use of a substrate as is used in measurements of the β-asymmetry parameter A [3, 45]. A solution is the use of a Magneto Optical Trap (MOT) in which the atoms are essentially at rest and confined in a region smaller than 1 mm^3.

In the following section the main components of the double-MOT setup will be sketched; for a more detailed description of the MOT setup and the atom transfer see [44].

4.2.1 Sodium trapping and the laser system

Fig. 4.2 shows the electronic level scheme of the Na atom. The atoms are trapped using the D2 line ($3^2S_{1/2} \rightarrow 3^2P_{3/2}$). The main cooling transition is the F=2 to F'=3 transition. However, some atoms will be excited to the F'=2 state, due to the line width of the transition and the presence of Zeeman and

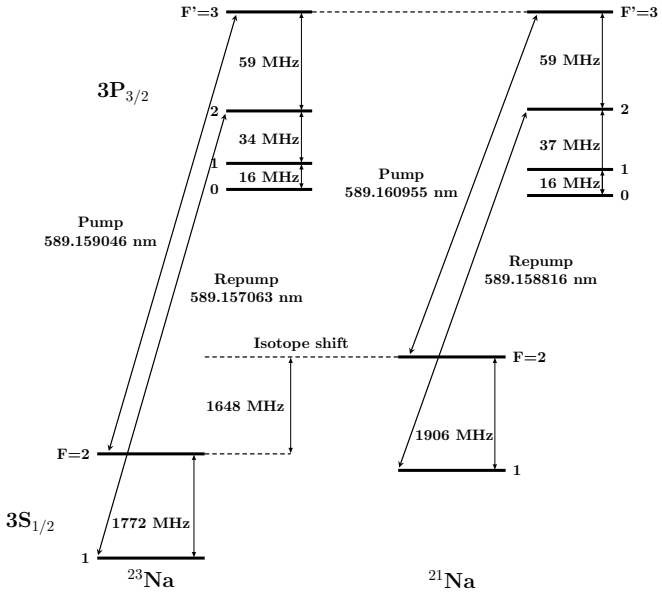

Figure 4.2: *The electronic level scheme near the sodium D2 line ($3^2S_{1/2} \rightarrow 3^2P_{3/2}$) of the stable isotope ^{23}Na and the radioactive ^{21}Na. The cooling ('Pump') transition is indicated with an arrow between the F=2 and the F'=3 hyperfine states. The repump transition goes from F=1 to F'=2. The isotope shift and the hyperfyne splittings in ^{21}Na are taken from [46], all other values from [47]. This figure is taken from [44], slightly modified.*

Doppler shifts; they can decay to the F=1 ground state. To close the cycle an additional 'repump laser' is used to drive the F=1 to F'=2 transition.

The laser light for the cooling transition is delivered by a solid state laser from Toptica Photonics (type DL-RFA-SHG PRO). The production of yellow light at 589 nm goes in three steps. Around 30 mW of light at 1178 nm is produced by a diode laser serving as a seed. This is coupled into a Raman fiber amplifier and amplified to around 3.5 W. Finally the frequency is doubled in a second harmonic generation stage, giving an output of around 2 W of 589 nm light.

The light for the repump transition is produced by a Spectra Physics 380D ring dye laser producing around 350 mW of 589 nm light. The laser light was transported through a 100 m long fiber and with a transport efficiency of around 40% about 120 mW reached the experimental setup.

A frequency comb (Menlo Systems, FD1500/075) provides an absolute reference frequency. The cooling laser was locked to the comb. The frequency of the repump laser was locked at a fixed offset from the cooling laser frequency.

A schematic layout of the laser optics is shown in Fig. 4.3. The MOT chambers are schematically indicated. The actual configuration is given in Fig. 4.1. The collector MOT is situated on the left, the decay MOT on the right, and in between is the funnel section. The light enters the table through a fiber. A Polarizing Beam Splitter cube (PBS) divides the light between the collector MOT and the decay MOT. An Acousto-Optical Modulator (AOM) is switching the push beam on and off. The split-off light goes up via a periscope and is directed along the line connecting the two MOTs. The main beam leaves the AOM and enters a Pockels cell which, combined with a PBS, redirects the light of the MOT to the funnel section when the push beam is on. The main beams for the two MOTs are expanded by telescopes and the quarter-wave plates are used to create circularly polarized light.

4.2.2 Collector MOT

The $^{21}Na^{+}$ ions from the low energy beam line (LEB line) enter the trapping volume (see Fig. 4.1), which is a glass cell (Fig. 4.4) manufactured by Technical Glass inc. The ions are collected on 25 μm thick zirconium (Zr) neutralizer foil. NaI detectors are put near the foil to detect the 511 keV annihilation radiation which is used to measure the incident ion rate. The foil is periodically heated by an electric current to about 1100 K to release the atoms into to the trapping volume. The released fraction is estimated at 30% for ^{21}Na [44].

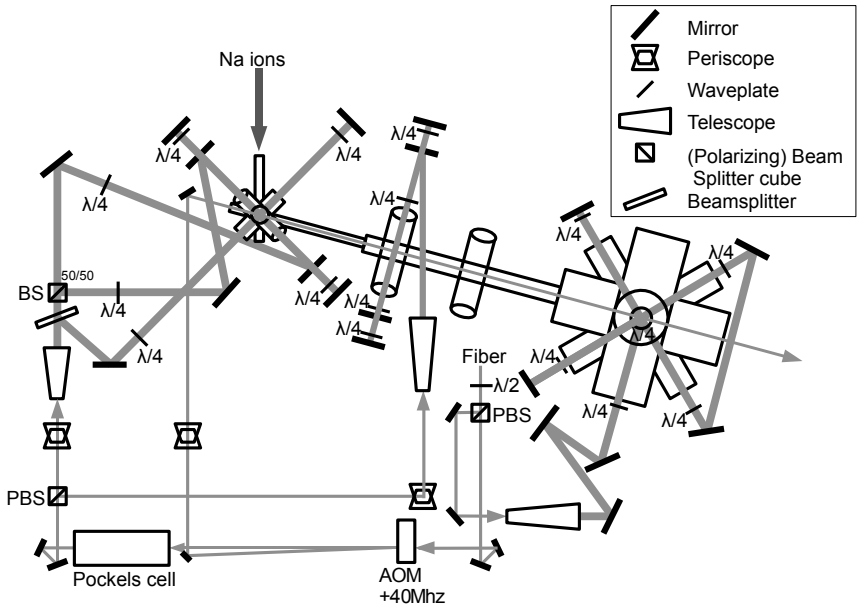

Figure 4.3: *The layout of the laser table. See text for details. Figure courtesy of Wilbert Kruithof.*

The atoms in the trapping volume pass through the laser beams. The capture probability as a function of the speed of the atom has a cutoff at the so called capture velocity (v_c) which is in the order of 30 m/s. Therefore, only the low velocity tail of the Maxwell-Boltzmann distribution can be captured. Multiple passes through the trapping volume increase the capture probability. For this one needs to prevent the atoms from sticking to the cell walls. This can be done by applying a non-stick coating. We tried two types of coatings: SC-77 (Fluorochem Ltd) or PDMS (Xiameter, with a viscosity of 10^5 centistokes). After the bounce off the glass wall the atoms are re-thermalized to room temperature, thereby increasing the single pass capture probability by a factor 7 [44].

If a working coating is applied the number of bounces is limited by the geometry of the cell; at some point an atom will permanently leave the trapping volume through one of the exits. For the cubic trapping cell, shown in Fig. 4.4,

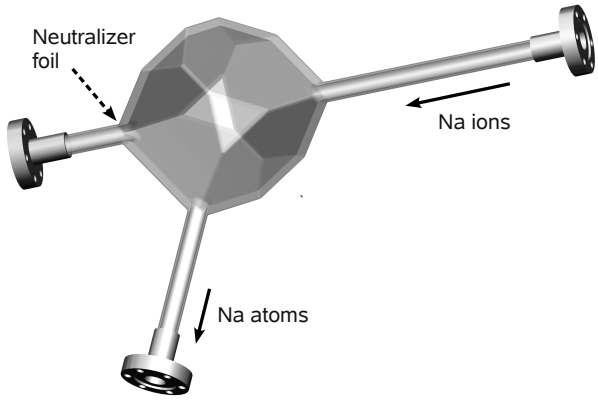

Figure 4.4: *The cubic glass cell of the collector MOT. The ^{21}Na ions enter from the right, fall on the neutralizer which is mounted on the left flange. The trapped ^{21}Na atoms are pushed to the detection setup through the tube at the bottom of the picture.*

this geometrical maximum is estimated at 500, allowing for an increase of the collection efficiency over the single pass efficiency by a factor of 100. In the current situation the collection efficiency in the collector MOT, defined as the fraction of the number of atoms coming off the neutralizer that end up trapped in the MOT, is about 2×10^{-4}, mainly limited by the number of bounces which is estimated to be of order 1 [44]. Therefore, thus far the coating was not successfully applied. A simple check is performed by letting a droplet of water slide over the coated glass surface. When applied correctly the coating creates a hydrophobic surface on which the droplet can freely slide, without wetting the surface. Our cell did not convincingly pass this test.

Detecting the trapped atoms was done by fluorescence detection. Fig. 4.5 shows a typical neutralizer heating cycle using natural sodium. A lens system collects the light and in the image plane an aperture cuts away part of the background. A narrow band filter (15 nm around 589 nm) reduces the background counts from ambient light as well as the black body radiation from the hot neutralizer. For the photon detection a Hamamatsu R7449 photo multiplier tube (PMT) is used. The overall detection efficiency is 10^{-5} or, with a photon scatter rate per atom in the MOT of 10^7 /s, 10^2 photons/s/atom.

Fig. 4.6 shows the observation of fluorescence from radioactive ^{21}Na in

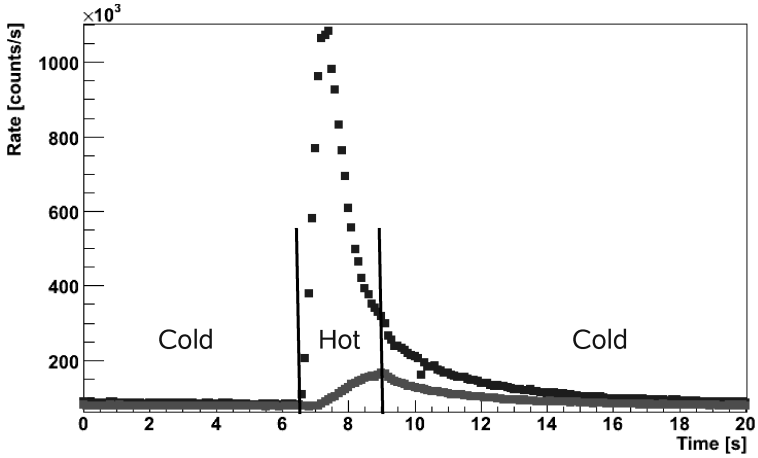

Figure 4.5: *The MOT fluorescence as a function of time; a full cycle is shown. During the time interval indicated by the two lines, the neutralizer is hot and the atoms are released into the trapping volume. The higher (lower) of the two peaks is with (without) a beam of ^{23}Na ions on the neutralizer. Even without ion beam there is still residual ^{23}Na coming off the neutralizer. Figure courtesy of Wilbert Kruithof.*

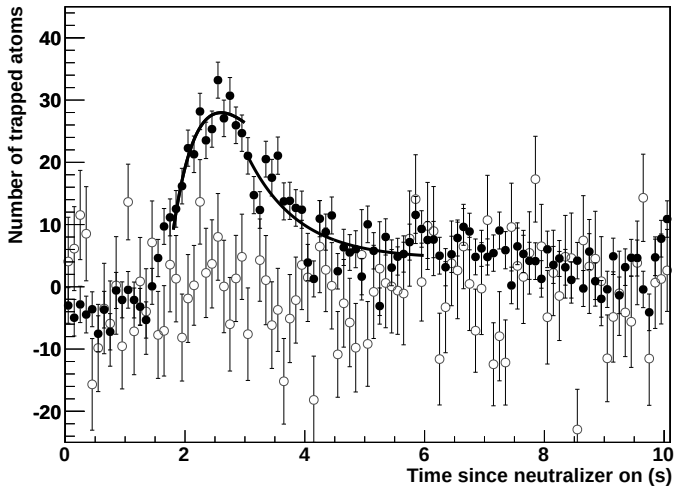

Figure 4.6: *Fluorescence signal of trapped ^{21}Na in the collector MOT. The closed symbols show a measurement with red detuned lasers (trapping), the open symbols with blue detuned lasers (anti trapping). The curve through the data is a model fit; details can be found in [44], where the picture is taken from.*

our MOT setup. The figure shows the result of two different laser frequency (but otherwise identical) settings: trapping (closed symbols), and anti-trapping (open symbols). The anti-trapping measurement was done to ensure that the signal was indeed from trapped ^{21}Na. The trapping signal shown is the result of about 1 hour of data taking, heating the neutralizer 2 s per 40 s.

The vacuum is maintained at $\sim 5 \times 10^{-9}$ mbar by a turbo pump and ion pump. However, when the neutralizer foil is heated the pressure in the cell increases.

4.2.3 Atom transfer

The atoms are transferred from the first to the second MOT by an on-resonance push beam over a distance of about 70 cm. For transverse compression and cooling a '2D MOT' (funnel) was built but not yet made to work, see Fig. 4.1 and 4.3. A transport efficiency of around 80% has been achieved in setups of comparable dimensions. For an overview see [44]. In the present experiment, using only the push beam, an efficiency of a few percent was reached. This compares well to systems using a push beam only. A higher efficiency is foreseen once the funnel section is successfully commissioned.

The push beam has been operated in a pulsed mode. It was on for about 10-40 µs, which was realized by selecting the first order diffracted beam from an AOM (see Fig. 4.3), 40 MHz above the cooling transition of the MOT. During the push time the MOT beams must be turned off to prevent re-trapping. This is done by redirecting the MOT beams to the funnel for 1 ms using a Pockels cell decreasing the intensity in the MOT beams by a factor of 190.

4.2.4 Decay MOT

In and around the decay chamber (described in section 4.3) a second MOT setup was built (see [34]). The trapping laser light is provided by a laser beam with a diameter of around 15 mm. The main magnetic filed for the MOT is produced by two coils. 300 A flows trough the coils which are separated by 28 cm and have 16 windings of hollow copper tubes that allow for water cooling.

4.3 Decay products detection

The decay chamber (see Fig. 4.1) is a CF-200 six-cross chamber with 4 extra CF-63 ports for the MOT laser beams and 4 extra ports, one of which is used

for MOT fluorescence detection. An ion pump and a turbomolecular pump keep the pressure at $\sim 10^{-10}$ mbar. On two opposing CF-200 flanges the recoil ion momentum spectrometer (RIMS) and the β detector are mounted.

4.3.1 Recoil ion detector

In chapter 3 we discussed how the decay correlation parameters are measured. In particular, for the correlation parameter D we considered possible detector geometries. For a measurement of the β- correlation parameter a one can make use of the recoil-ion momentum or use only the time of flight of the ion to the MCP detector. For a D measurement it is required to know the initial direction of the recoil ion and thus to fully resolve the recoil ion momentum. This is realized in practice by recording the hit position on the MCP and the time of flight.

A detailed description of the detector is given in chapter 5; here we give a short overview of the main components. The center of the MOT is about 12 cm away from the MCP. The guiding field for the ions is produced by three copper ring electrodes with an inner diameter of around 12 cm. The ions are collected at an MCP and on impact a localized shower of electrons is produced at the backside of the MCP at the hit position. A few mm behind the MCP a delay line detector (RoentDek DLD80) is installed to determine the position of this electron pulse, and by that the hit position. The time of flight is determined by measuring the time difference between the β particle detection and the ion impact on the MCP. Using a sufficiently strong guiding field, the full solid angle can be covered.

4.3.2 β detector

A detector is used that detects both the energy and position of the β particle. It should be able to distinguish between gammas (mainly from annihilation) and β's and finally, since the the detection of the β particle is the main event trigger and starts the time of flight measurement, it should have a good timing resolution.

More details can be found in chapter 6 on the β detector, here we give its main characteristics. Due to its favorable pulse rise time properties [34] it was chosen to use NE104 plastic scintillator material. There are two layers of scintillation material: a 2 mm thick layer (ΔE detector) and a 2 cm thick layer (E detector) to stop the β particles. Light created in the ΔE or E detector is guided to PMTs. By using multiple PMTs we can estimate the hit position of

the β particles. For more details we refer to 6.2.3. Demanding a coincidence between the two layers reduces the background from gammas.

4.4 Data acquisition

The signals from the detectors in the experimental setup are shaped and fed into various VME-modules to be described in more detail in chapter 5 and 6. These modules are initialized and read out by software called CADDIE (Control and Distributed Data-acquisition Integrated Environment) running on a VME computer. CADDIE also groups the data from the separate modules into events and sends them over the network to a receiving computer. It was developed by F. Zwarts of the IT department at the KVI.

On a normal desktop or laptop computer the Bogey software is running. It was developed by C.J.G. Onderwater from the TRIμP group at the KVI. Bogey connects with CADDY over the network and receives the data. Usually the data is saved to disk for later off-line analysis. Since Bogey is integrated with the ROOT data analysis framework [32] it offers great flexibility in on-line and off-line analysis of the data stream.

CHAPTER 5

Recoil-ion momentum spectroscopy

The observables that need to be measured to reconstruct the three-body kinematics of β-decay are the momentum of the β-particle and the recoil ion. This chapter concerns the latter.

The relatively low energy (max. 229 eV) of the recoil allows for guiding it in an electric field onto a position sensitive detector. In this way a 4π solid angle is covered. The detection of the β-particle serves as a starting time for the Time-Of-Flight (TOF) measurement. The measurement of the hit position of the recoil position and its TOF can be combined to determine the recoil momentum.

5.1 Setup

Fig. 5.1 shows a schematic overview of the recoil spectrometer. The MOT cloud with radioactive atoms is located between the two rings on the left. The voltages on the three copper rings determine an electric field that guides the recoil nuclei to the Multi Channel Plate (MCP) detector. When a recoil ion hits the MCP an electron cloud produced by the MCP falls on the delay-line detector allowing for a 2D reconstruction of the impact position. In the following the MCP and delay lines will be described in some more detail.

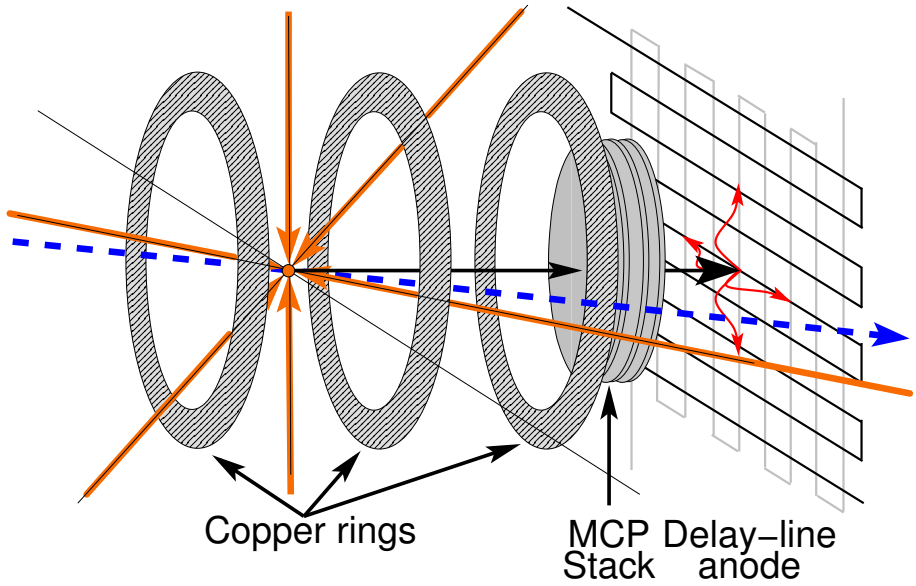

Figure 5.1: *The recoil ion momentum spectrometer. The three electrode rings define an electric field, guiding the ions to the MCP. The electrons from the MCP fall on the delay-line anode. The solid lines indicate the path of the trapping laser beams, the dashed line the pulsed UV-laser, used for the calibration procedure described in this chapter. Figure courtesy of Sander Rikhof.*

5.1.1 MCP and delay lines

The position sensitive detector is a 3 layer MCP stack (z-stack configuration) with behind it a delay-line anode (RoentDek DLD80). The delay-line anode has a sensitive area of 8 cm by 8 cm and consists of a square frame with wires wound around it in two orthogonal directions. When an electron cloud hits the delay line a small electric signal travels to both ends of each wire. The difference in arrival time at the ends allow for a position reconstruction.

Actually, there are two *pairs* of wires wound around the frame. Each pair has a signal and a reference wire. The signal wire is at a slightly higher potential ($\sim$ 50 V; see Fig. 5.2), and will collect most of the electrons. The electronic noise on the delay lines will be common on the wire pair. Using a differential amplifier this noise can be removed from the actual signal(see Fig. 5.3).

In this work we estimate the efficiency of the MCP to be 50% which is close to the open area ratio. This is experimentally observed using $^{23}Na^{+}$ ions [48]. According to [49] the efficiency can be increased to 85% by using a negatively biased grid in front of the MCP to recapture secondary electrons. This has not been tested in our setup.

5.1.2 Electronics and DAQ

To operate the recoil detector several high voltages need to be applied (see Fig. 5.2): to create the guiding field and also to operate the MCP. A voltage divider circuit outside the vacuum biases the MCP and the delay-line anode, while the three rings have their own high voltage supply.

The electronic and data acquisition schematics are shown in Fig. 5.3. The upper block in the figure shows how the analog signals are processed, digitized by a discriminator, and recorded by a CAEN 1290N multihit time to digital converter (MTDC) that timestamps the hits on its input channels. The MTDC can run in several modes. In the measurements discussed in this chapter it ran in continuous mode, meaning that the MTDC records every hit on all channels continuously, which can be read out on request. The lower block shows the readout logic. It ensures that the MTDC is read out once per ms, but only when a run is going. All signals are also fed into a scaler module (not in figure), and is read out every second.

The typical time scales involved are shown in Fig. 5.6. A TOF is around 1.4 µs, and time between the anode hit and the delay-line hits (average, t_0) is around 50 ns. The system allows timestamps with a resolution of 97.7 ps. To correctly keep track of the total running time we should not miss any of the roll

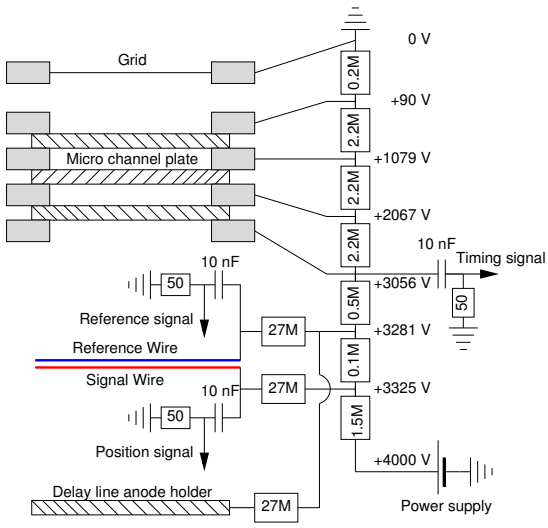

Figure 5.2: *The voltage divider circuit for the MCP and delay-line anode. Figure courtesy of Sander Rikhof.*

overs. The hits in the measurements done in this work come at most at a 50 Hz rate which is too low for that. To be sure not to miss a roll over a 10 kHz clock signal is put on one of the input channels of the MTDC[1].

5.2 Electric field and trajectory simulation

Ideally the guiding electric field E is homogeneous, causing a constant acceleration $a = qE/m$ so that the ions follow a parabolic trajectory to the recoil detector. The initial distance to the MCP is L, T will denote the TOF, and r the distance of the hit position from the center of the MCP. For a point source it can be seen that the mapping $(v_z, v_r) \mapsto (T, r)$ is one-to-one,

[1]From the roll over time of 51 µs one would expect to need at least 20 kHz but the MTDC records both the leading and trailing edge of a pulse.

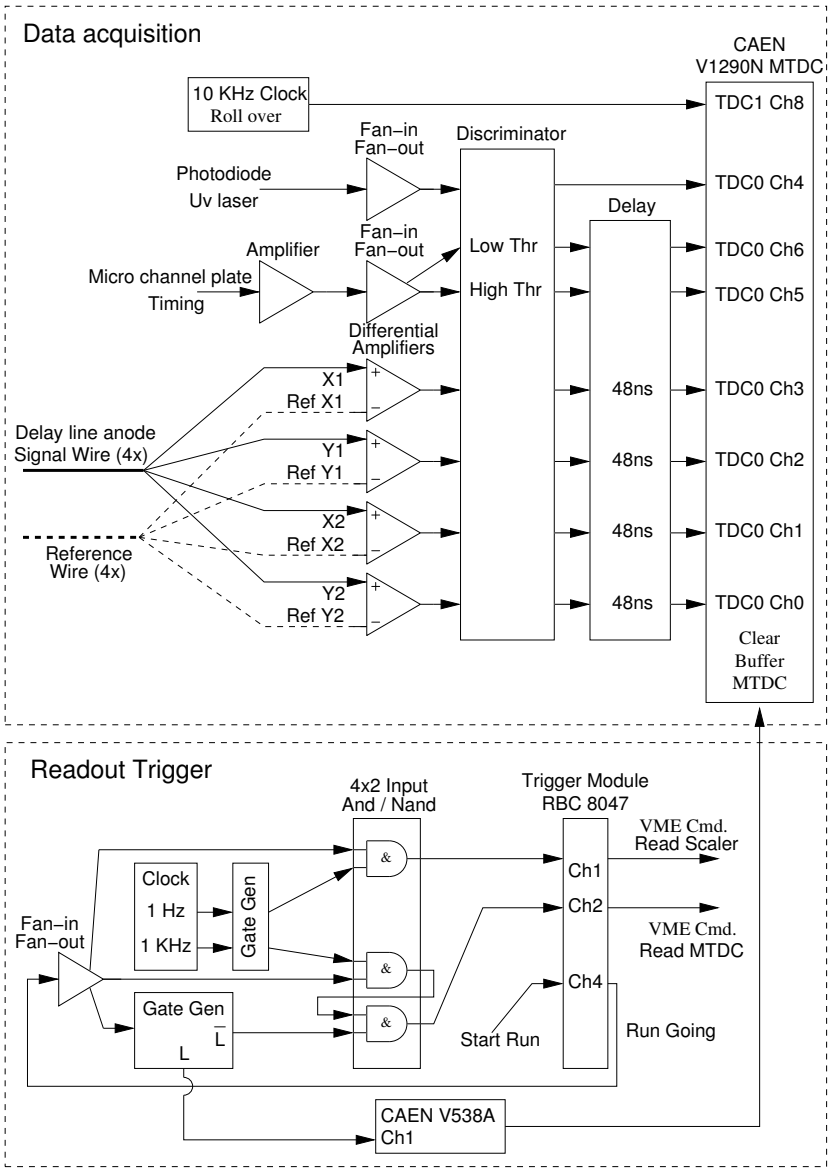

Figure 5.3: *Schematics of the electronics and data acquisition of the recoil ion detection setup. Figure courtesy of Sander Rikhof.*

$$T = \frac{v_z + \sqrt{v_z^2 + 2aL}}{a},$$
$$r = v_r T. \tag{5.1}$$

Conversely,

$$v_z = \frac{1}{2}aT - \frac{L}{T},$$
$$v_r = \frac{r}{T}. \tag{5.2}$$

With SimIon we calculated the electric field and simulated the flight of the ions from the MOT-cloud to the detector. Based on these simulations and initial measurements an additional foil was placed on the copper electrode farthest from the MCP. Without it the distortions due the surrounding chamber at ground potential and the open structure of electrodes were rather large at the site of the trapped atoms. This is illustrated in Fig. 5.4.

In some atomic-physics applications of recoil-ion spectrometry one uses more complicated detector geometries that can compensate for non-zero sample size. One can apply time focusing and position focusing or a combination of the two. Time focusing means that the TOF is to first order independent of the starting position in the z direction, but the sensitivity to $v_{z,0}$ is retained. It can be achieved by introducing a field free drift region after initial acceleration from the decay site [50]. Position focusing makes the hit position on the MCP to first order insensitive to a displacement in the xy plane. An electrostatic lens can achieve this. Combining these two gives 3D focusing and has successfully been applied in atomic-physics experiments (see e.g. [51, 52]). In these cases tens of centimeters long field-free drift regions are used. In our setup there is enough space to accommodate this. Although in the experiment of Behr at TRIUMF it was chosen to use a uniform field without any focusing [38], to simplify the analysis and speed up the Monte Carlo simulation, it should be investigated how much the sensitivity to the MOT position and size (see tables 3.3-3.5) can be improved using focusing.

5.3 Measurements

To test the MCP and delay-line combination, stable sodium atoms are trapped and cooled in the MOT in the measurement chamber and are ionized by a pulsed

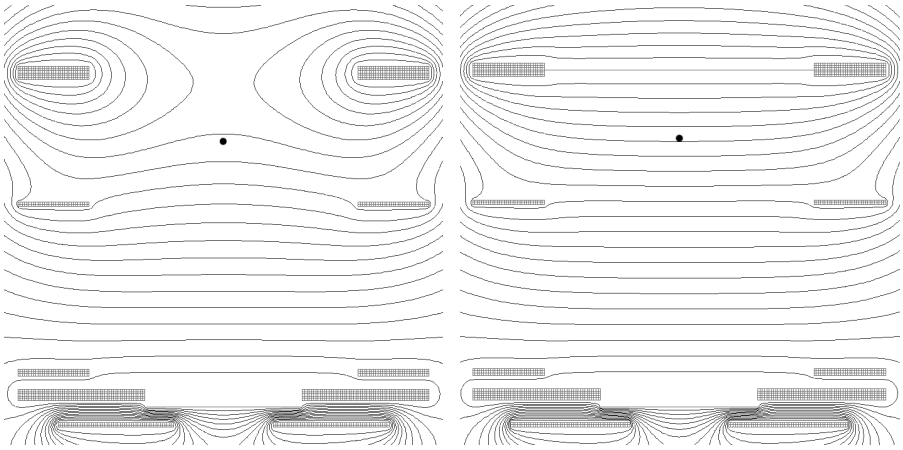

(a) *Without foil in upper ring.* **(b)** *With foil in upper ring.*

Figure 5.4: *The equipotential lines of the guiding field, on a cut through the center of the detector, as calculated by SimIon. The black dot indicates the position of the trapped atoms.*

laser. We use the 3$^{\text{rd}}$ harmonic of a Quantel Brilliant 1024 nm laser. At 50 Hz pulses at 355 nm are produced. The Na atoms that are exited by the 589 nm trapping laser can be ionized with an energy excess of 0.45 eV. The recoil energy of $2.3 \cdot 10^{-5}$ eV or 14 m/s, is extremely low. The ions can be considered at rest for our purposes. The applied electric field strength is 33 V/mm causing an acceleration of $1.4 \cdot 10^{11}$ m/s^2 for a singly charged ion.

The signals that are recorded in the measurements described in this section are shown in Fig. 5.6. The arrival time can be deduced from the timing signal from the anode (t_a) or from the average time of the four signals from the delay-line detector. The TOF start is given by the detection of the UV-pulse by a photo diode.

A spatial reconstruction of the laser induced ionization events could be made and is shown in Fig. 5.5. The x and y coordinate follow directly from the delay-line data. The z coordinate is calculated from the TOF assuming a constant acceleration. The MOT position in these figures is by construction close to $z = 0$. The bright spot shows ionization events from the MOT, the larger region of hits around it is identified as a molasses. This was checked by turning off the magnetic field of the MOT; the bright spot disappeared but the larger

region around it remained.

5.3.1 Timing resolution

In this section we will determine the time resolution of the anode signal from the MCP. The resolution in the TOF measurement in a β-decay measurement can be found by combining the anode time resolution with the time resolution of the β-detector.

When an the electron cloud hits a delay line at t_h, a pulse will travel from the hit position to both ends of the wire, arriving at t_1 and t_2. The combined travel time $(t_1 - t_h) + (t_2 - t_h)$ is constant, reflecting the fixed length of the wire. The subtraction of t_h is crucial since $t_{1,2}$ have an *unknown*, common time offset, varying from event to event. Since t_h is unknown, some common subtraction needs to be done. One option is to use the timing signal from the MCP anode, t_a:

$$T_{\Sigma i} \equiv (t_{i,1} - t_a) + (t_{i,2} - t_a) \qquad (i = x, y) \tag{5.3}$$

remain constant. The corresponding relation for the resolutions, assuming normally distributed 'noise', are

$$\sigma^2_{\Sigma i} = \sigma^2_{i,1} + \sigma^2_{i,2} + 4\sigma^2_a \qquad (i = x, y). \tag{5.4}$$

This alone is not enough to determine σ_a, the timing resolution of the MCP. Consider in addition a second constant quantity

$$T_{\Delta xy} \equiv (t_{x,1} + t_{x,2}) - (t_{y,1} + t_{y,2}). \tag{5.5}$$

The width of the distribution of this quantity is independent of σ_a:

$$\sigma^2_{\Delta xy} = \sigma^2_{x,1} + \sigma^2_{x,2} + \sigma^2_{y,1} + \sigma^2_{y,2}. \tag{5.6}$$

Assuming that the timing at all four wire ends can be measured with the same resolution, one finds $\sigma_{x,1} = \sigma_{x,2} = \sigma_{y,1} = \sigma_{y,2} = \frac{1}{2}\sigma_{\Delta xy}$. Now the anode resolution is determined by

$$\sigma_a = \frac{1}{2}\left(\sigma^2_{\Sigma i} - \frac{\sigma^2_{\Delta xy}}{2}\right)^{1/2}, \tag{5.7}$$

where again $i = x$ or y.

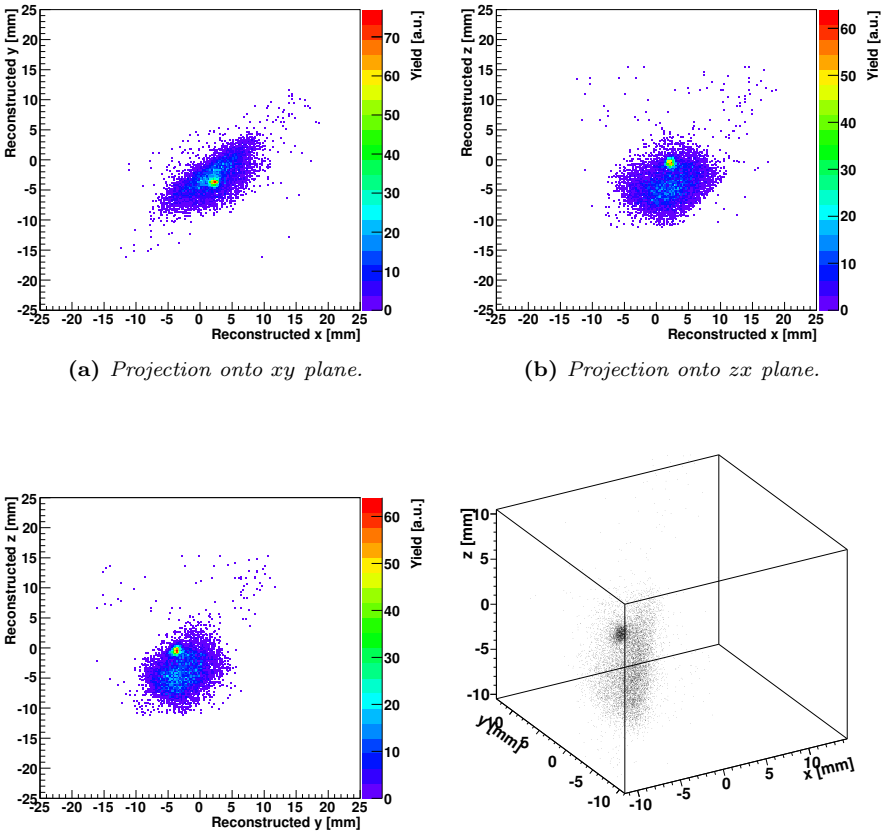

(a) *Projection onto xy plane.*

(b) *Projection onto zx plane.*

(c) *Projection onto yz plane.*

(d) *3D-view.*

Figure 5.5: *Reconstructed ionization events.*

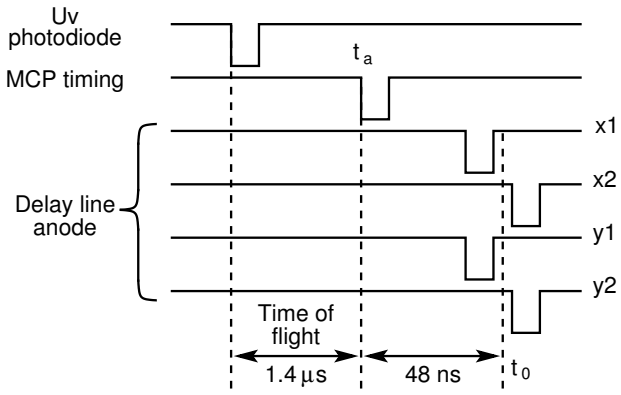

Figure 5.6: *The signals coming from the MCP-delay-line-detector combination. The time of the MCP timing signal will be denoted by t_a and of $x1$ by $t_{x,1}$, etc.*

The measured values are $\sigma_{\Sigma x} = 1.55$ ns, $\sigma_{\Sigma y} = 1.61$ ns are very close and ideally would have been the same. $\sigma_{\Delta xy} = 0.77$ ns so that (taking the larger of the $x-$ and $y-$results) $\sigma_a = 0.76$ ns.

In section 6.2.4 the timing resolution (FWHM) of the β-detector is found to be 2.7 ns. The resolution (FWHM) of the TOF is then 3.2 ns.

5.3.2 Position measurement and resolution

The time of the signals from both ends of the delay lines can be used to calculate the hit position. Let, as in the previous section, $t_{x,1}$ denote the recorded arrival time of the the signal at one end of the x-wire and v the signal propagation velocity in the wire, then

$$\begin{aligned} x &= v(t_{x,1} - t_{x,2})/2 \\ y &= v(t_{y,1} - t_{y,2})/2. \end{aligned} \tag{5.8}$$

According to the specifications we know that the 'single pitch propagation time' of the delay line is 0.95 ns/winding and given the winding density of 1.0 windings/mm this leads to $v = 1.1$ mm/ns.

The x-coordinate is essentially the difference

$$t_x := t_{x,1} - t_{x,2}. \tag{5.9}$$

A projection of the graph in Fig. 5.5a on the x-axis shows a peak on top of a background. The width of the peak is a combination of the uncertainty in the timing measurement and the size of the MOT cloud in the x direction ($\sigma_{M,x}$)

$$\sigma_x^2 = \sigma_{x,1}^2 + \sigma_{x,2}^2 + \sigma_{M,x}^2, \tag{5.10}$$

A fit shows that $\sigma_x = 0.84$ ns. Combining this with the results from section 5.3.1 we infer a MOT size of 0.32 mm.

The resolution in the position measurement was essentially already determined in the previous section. Using Eq. (5.8) we find

$$\sigma_{\text{pos}} = \frac{v}{2}\sqrt{\left(\sigma_{x,1}^2 + \sigma_{x,2}^2\right)} = 0.3 \text{ mm}. \tag{5.11}$$

5.3.3 Discussion

In chapter 3 we saw that departure from an ideal situation (e.g. finite TOF resolution) is not necessarily a problem, but that good knowledge about the imperfection is important (e.g. uncertainty in the TOF resolution). Presently we do not have an estimate of the error on the position and timing resolution. However, when the actual resolution is better than the maximally allowed uncertainty in the resolution, we may assume that the performance of the detector is good enough.

The resolution of the TOF only plays a role in the measurement of the β-ν correlation parameter a. The current performance of 3.2 ns (FWHM) or 1.4 ns (σ) is better than the required 14 ns for a TOF measurement with shake-off electrons as a trigger (table 3.5), so even with the incomplete knowledge about the TOF resolution we can say it suffices. This can not yet be said for a TOF measurement using a β detector as an event trigger (table 3.4).

Conceptually, we can use the position sensitivity of the MCP to monitor the MOT size and position by photo ionizing the trapped atoms. In practice this only works if the position resolution is sufficiently good. The current position resolution of 0.3 mm is better than the required knowledge of the MOT *size* in the case of a using shake-off electrons and A. In case of a, A and D measurements it is good enough to monitor the *position* of the MOT.

5.4 Energy resolution

Assuming the model given by Eq. (5.2), we can calculate the recoil energy $E_r(r, T)$. Since the recoil energy is limited to 229 eV, we can identify a region

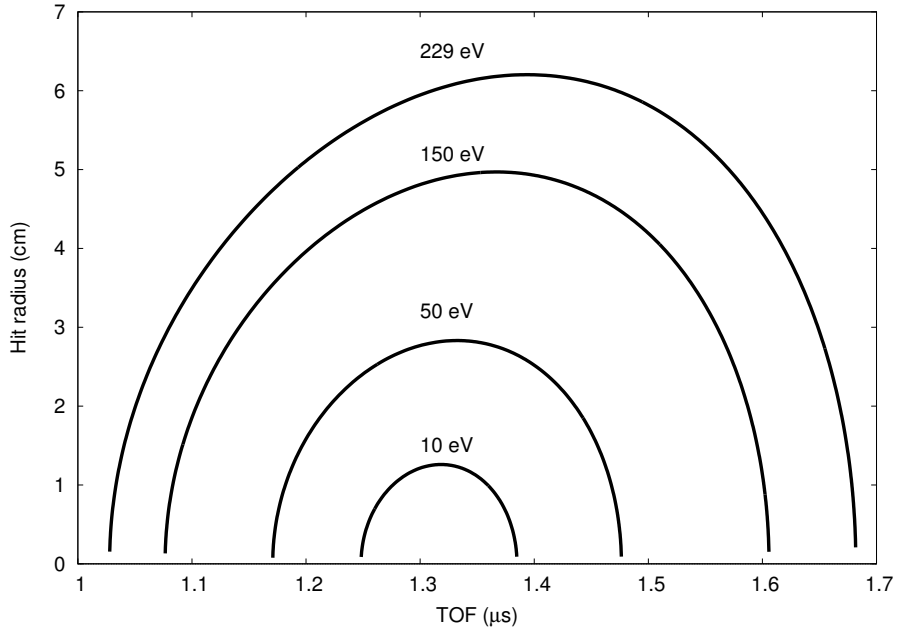

Figure 5.7: *The hit radius as a function of TOF, for several recoil energies.*

in the rT plane in which an event may happen. This is illustrated in Fig. 5.7. If we assume non-correlated Gaussian noise in the parameters (α_i) that enter the energy calculation, we can calculate the uncertainty in the recoil energy from

$$\begin{aligned}\sigma_{E_r}^2 &= \sum_i \left(\frac{\partial E_r}{\partial \alpha_i}\right)^2 \sigma_{\alpha_i}^2 \\ &= \left(\frac{a^2T^4 - 4(L^2 - r^2)}{2T^3}\right)^2 \sigma_T^2 + \left(\frac{2L - aT^2}{T^2}\right)^2 \sigma_L^2 \\ &\quad + \left(\frac{2L - aT^2}{2}\right) \sigma_a^2 + \left(\frac{2r}{T^2}\right)^2 \sigma_r^2. \end{aligned} \tag{5.12}$$

The first term reflects the uncertainty in TOF, the second in the starting position (MOT cloud size), the third in the acceleration, and the fourth in the measured hit position. Fig. 5.8 shows E_r, σ_{E_r}, and σ_{E_r}/E_r. The uncertainties,

Quantity	Value
L	121 mm
a	$1.4 \cdot 10^{11}$ ms^{-2}
σ_T	2,7 ns
σ_L	0.4 mm
σ_a	$1.4 \cdot 10^{8}$ ms^{-2}
σ_r	0.28 mm

Table 5.1: *Overview of the values (cf. results from sections 5.3.1 and 5.3.2.) used to obtain the energy resolution. For σ_a it is assumed that the potentials of the ring electrodes can be kept constant within ∼1‰.*

σ_i, that were used are listed in table 5.1. A typical value for the absolute error is 6 eV (Fig. 5.8b) and for the relative error 0.04 (Fig. 5.8c).

The finite resolution in E_r will distort the measured recoil energy spectrum. We saw in section 3.2.2 that such a distortion can be dealt with effectively as long as its description is sufficiently accurate.

5.5 Distortions of the Electric field

Distortions to the electric field lead to systematic errors. Consider the following deviation from a constant electric field[2]:

$$\begin{aligned} E_z(r,z) &= E_0\left(1+\alpha\frac{z}{2L}\right) \\ E_r(r,z) &= -\frac{\alpha E_0}{L}r. \end{aligned} \tag{5.13}$$

This results in the decoupled equations of motion

$$\begin{aligned} \ddot{z} &= a_0 + \beta^2 z \\ \ddot{r} &= -\frac{\beta^2}{2}r, \end{aligned} \tag{5.14}$$

where $\beta = \sqrt{\alpha a_0/L}$ and $a_0 = qE_0/m$, the acceleration when $\alpha = 0$. Solving Eq. (5.14), subject to the initial conditions $z(0) = r(0) = 0$ and $\dot{z}(0) = v_z$ and

[2]To obey $0 = \nabla \cdot \mathbf{E} = (\partial_r + \frac{1}{r})E_r + \partial_z E_z$, one must include a distortion in E_r as well.

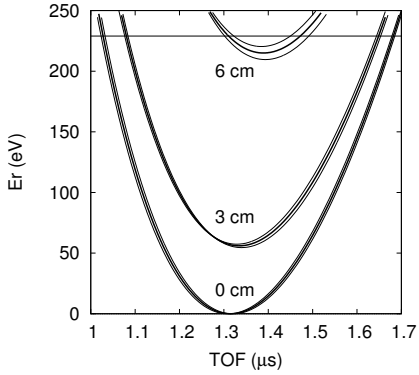

(a) *E_r for different radii. The horizontal line indicates the maximum recoil energy for ^{21}Na of 229 eV. The thin lines around each curve indicate the change in E_r due to a distortion, as discussed in section 5.5 with $\alpha = \pm 0.05$.*

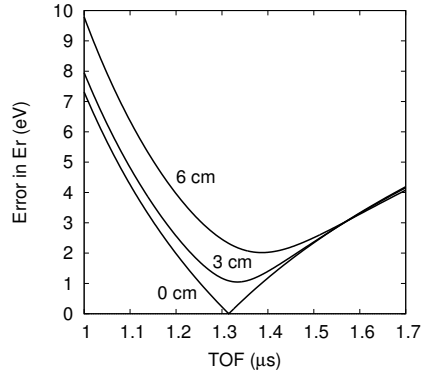

(b) *σ_{E_r} for different radii.*

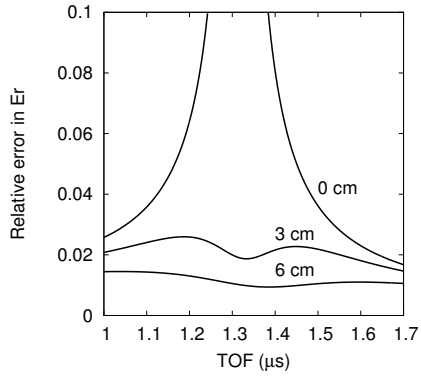

(c) *σ_{E_r}/E_r for different radii. The relative error diverges when E_r goes to zero.*

Figure 5.8: *The recoil energy, its error, and relative error.*

$\dot{r}(0) = v_r$, gives

$$z(t) = \frac{a_0}{\beta^2}\left(\cosh(\beta t) - 1\right) + \frac{v_z}{\beta}\sinh(\beta t)$$
$$r(t) = v_r \frac{\sqrt{2}}{\beta}\sin(\frac{\beta}{\sqrt{2}}t) \tag{5.15}$$

Expanding the sine and hyperbolic functions, one can see that the motion reduces to the case of a constant electric field E_0 for $\alpha \to 0$.

$$z(t) = \frac{1}{2}a_0 t^2 + v_z t + \left(\frac{v_z t}{3!} + \frac{a_0 t^2}{4!}\right)(\beta t)^2 + ...$$
$$r(t) = v_r t\left(1 + \frac{1}{3!}\left(\frac{\beta t}{\sqrt{2}}\right)^2 + ...\right) \tag{5.16}$$

At t=1.4 μs, a typical TOF, $(\beta t)^2 = 2.6\alpha$.

Inverting $z(t)$ from Eq. (5.15) gives the expression for the time of flight in terms of v_z

$$T = \frac{1}{\beta}\log\left(\frac{\beta\sqrt{\beta^2 L^2 + 2a_0 L + v_z^2} + \beta^2 L + a_0}{\beta v_z + a_0}\right)$$
$$= T_0 - \left(\frac{a_0^2 L^2 - 2a_0 L v_z^2 - 2v_z^4}{6a_0^2 L\sqrt{2a_0 L + v_z^2}} + \frac{v_z^3}{3a_0^2 L}\right)\alpha + ... \tag{5.17}$$

where $T_0 = (\sqrt{2a_0 L + v_z^2} - v_z)/a_0$, the unperturbed TOF. Substituting this result into $r(t)$ and again expanding around $\alpha = 0$ we find

$$r = v_r T_0 + \frac{v_r}{2}\left(\frac{L}{\sqrt{2a_0 L + v_z^2}} - T_0\right)\alpha + ... \tag{5.18}$$

Note that Eqs. (5.17) and (5.18) are the equivalent of Eq. (5.1). The inverse relations for obtaining v_z and v_r from the *measured* quantities r and T can be obtained directly from Eq. (5.15).

$$v_z = -\frac{1}{2}a_0 T + \frac{L}{T} + \frac{a_0^2 T^3 - 4a_0 L T}{24L}\alpha + ...$$
$$v_r = \frac{r}{T} + \frac{a_0 r T}{12L}\alpha + ... \tag{5.19}$$

Lastly, we can expand the recoil energy around $\alpha = 0$

$$E_r(r,T) = \frac{M}{2}\frac{4(L^2+r^2)+a_0T^2(a_0T^2-4z)}{4T^2} - \frac{M}{2}a_0\frac{4(2L^2-r^2)+a_0T^2(a_0T^2-6L)}{24z}\alpha + ... \tag{5.20}$$

The effect of this to first order in α can be seen in a plot of E_r vs. TOF in Fig. 5.8a, for $\alpha = \pm 0.05$. A careful study of the electric field is thus required.

5.6 Conclusions

In this chapter we described the design and performance of the recoil ion detector. An electric field pulls the recoiling daughter nucleus to the MCP and delay-line detector allowing for a measurement of the time and position of impact. The detector was tested by trapping stable Na in the MOT and ionizing it with a pulsed UV-laser at a rate of 50 Hz.

For the position resolution we found $\sigma_{\text{pos}} = 0.3$ mm, and for the timing resolution 0.76 ns. The energy of the recoil nucleus is a function of the TOF and the hit position and so the relative energy resolution depends on these parameters, see Fig. 5.8c. A typical value is $\sigma_{E_r} = 4\%$.

CHAPTER 6

β Detection

As discussed in chapter 3 there are five independent parameters in a three-body decay. So, the combined system of the recoil detector and the β detector should be able to measure at least five independent kinematic quantities. In the approach chosen here we measure six in total: in the previous chapter we discussed the 2D hit position of the recoil at, and its time of flight to the MCP while in this chapter we discuss the measurement of the energy of the β particle and its 2D hit position.

In [34] the requirements of the β detector were discussed and the design of the ΔE detector is motivated. Firstly, the detector should detect β particles and discriminate between positrons (β^+) and γ radiation. Secondly, to reconstruct both the momentum of the recoil it should have sufficient timing resolution for the start of the time-of-flight measurement, position and energy resolution. Thirdly, it should measure the energy and hit position of the β particle.

6.1 Detector setup

6.1.1 Design of the ΔE and E detector

For particle identification the detector consists of two parts: a ΔE and an E detector. A β particle entering the detector passes through a 75 μm thick stainless steel sheet. This sheet is part of the container in which the ΔE-E-detector combination is placed (see Fig. 6.1). It separates the UHV of the detection chamber from the β detector. This is necessary because the components of the detector are not UHV compatible. To avoid the need of a thick window, the ΔE part is kept at fore vacuum. The full assembly is mounted on a CF-200 flange of the detection chamber. The second layer the β particle passes, is the 2 mm thick scintillator disk (NE104) of the ΔE detector. β particles with energies up to about 0.7 MeV are mostly stopped in the ΔE detector. Higher energy β particles are minimum ionizing particles and loose mostly of ∼0.4 MeV [34] independent incident energy. The particles are stopped in the E detector in a 2 cm thick layer of the same scintillator material.

An important source of background are photons produced by positron annihilation. In 2 mm of scintillator material a 511 keV photon has a 2% probability to interact with the material [53]. Therefore, requiring a coincidence between the two parts of the detector, removes most of this background. In the remainder of this section both the ΔE and the E detector will be discussed.

The scintillator disk of the ΔE detector is 2 mm thick and has a diameter of 170 mm. Positioned at about 120 mm from the the center of the chamber, the fraction of the total solid angle covered is 9%. The scintillator photons travel through one of the six light guides, each coupled to a Hamamatsu R7449 PMT (see Fig. 6.1a). The segmenting of the light guides gives a certain position resolution (see section 6.2.3). Surrounded by a μ-metal tube, the PMTs are shielded from magnetic fields.

The present E detector (see Fig. 6.1b) can be put through the 13 cm diameter opening on top of the ΔE-detector housing. It closes off the interior of the ΔE detector ($\sim 10^{-3}$ mBar) from the outside air. The interior of the E detector with the PMTs is at ambient pressure. Its cylindrical housing is closed off by a 2 cm thick perspex disk, serving as a light guide. The 2 cm thick scintillator disk is put on this light guide with optical grease. When put together with the ΔE detector the thin and thick scintillator disc are separated by a few mm. An array of 7 Hamamatsu R7449 PMTs, one in the center and six around it, is coupled to the light guide with optical grease. The PMTs are shielded by μ-metal tubes. In this configuration the opening angle as seen from the center

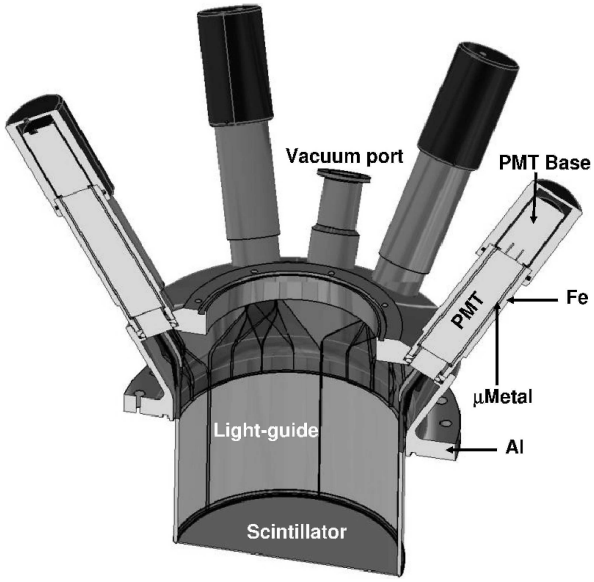

(a) *The ΔE detector.*

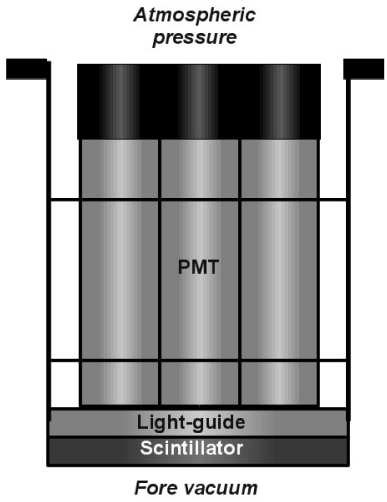

(b) *The E detector.*

Figure 6.1: *The E detector fits inside the ΔE detector.*

of the MOT is 5% of 4π (⌀12 cm at 13 cm).

6.1.2 Acceptance and efficiency considerations

The acceptance and efficiency are strongly affected by a number of parameters of the incident β particle. Both the energy and angle of incidence affect the back-scattered and accepted fraction. The graphs shown in Fig. 6.2 illustrate this. The data are simulation results using the 'Casino' software [33]. One can simulate the passage of electrons through several customized layers of material. Here, the simulation includes the vacuum separation sheet and the thin scintillator. A particle passing through these two layers is considered accepted. The threshold as it is used in the simulations of chapter 3 is based on the results shown in Fig. 6.2a.

For a 0° incident angle at $E_\beta \simeq 0.6$ MeV the back-scattered fraction is around 10%, see Fig. 6.2a. At this energy the β particle is stopped in the ΔE detector and will not cause an event trigger. As the energy increases, the back-scattered fraction goes down and reaches around 5% when half of the β particles reach the E detector. Since the MOT cloud is essentially a point source of β particles the angle of incidence is strongly correlated with the hit position on the detector and can be maximally 35°. The acceptance at 1 MeV varies between 60% (at 35°) and 77% (at 0°), see figure 6.2b.

These characteristics complicate the analysis of the experiment, but only an *error in the characterization* causes a systematic error in the final result, as discussed in section 3.2.1.

6.1.3 Electronics and DAQ

The electronics for the β detector are shown in fig 6.3. From the β detector a total number of 13 PMT signals need to be processed. They are split up in two groups: 1) six channels from the ΔE detector and 2) seven channels from the E detector. The two groups go into separate 8-channel constant-fraction discriminators. The event trigger for the measurements described here require that at least one PMT of each group fires. All analog signals are integrated in a CAEN V792 charge to digital converter (QDC); the logic signals go into a CAEN V1190B multi-hit time to digital converter (MTDC), which also records the time signals of the recoil detector (chapter 5). A SIS 3820 scaler module records the count rates. The pulses going into channel 1 and 3 of the electronic unit labeled 'Corbo' cause a readout of the scaler module and MTDC respectively. The scaler is readout every 10 ms, the MTDC with every β-detector trigger.

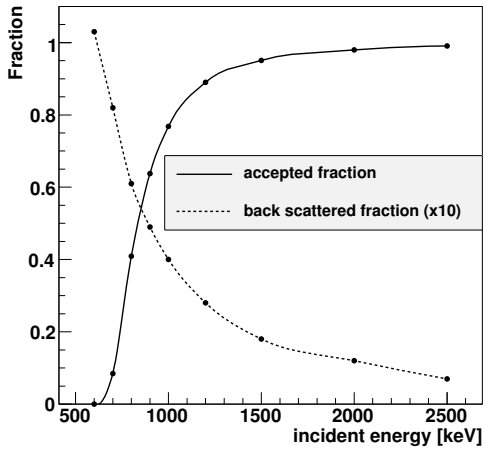

(a) *Fixed angle (0° with normal).*

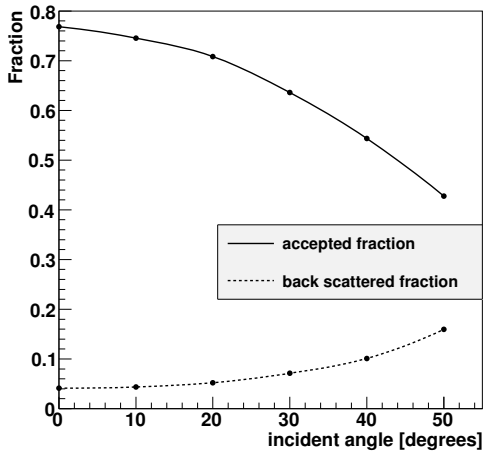

(b) *Fixed energy (1 MeV).*

Figure 6.2: *The acceptance and back scattering as a function of energy and incident angle. An event is considered accepted if a β particle passes through the ΔE detector. A back-scattered particle leaves the ΔE detector on the wrong side.*

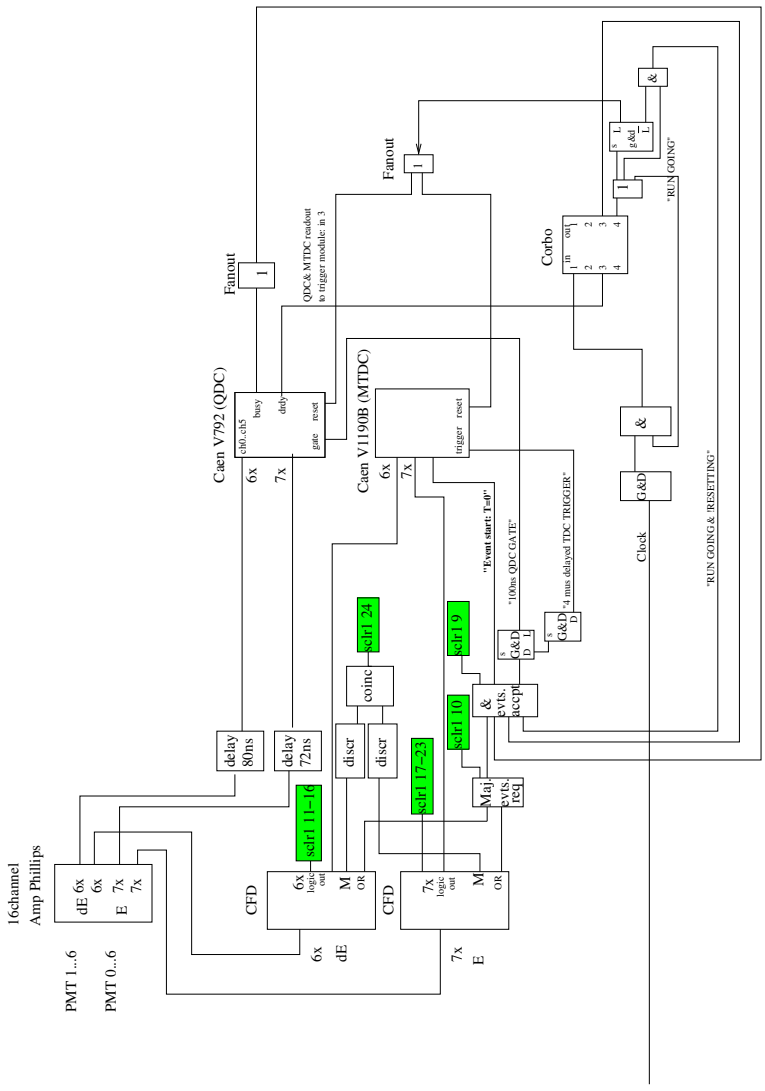

Figure 6.3: *Electronics scheme of the beta detector. There are two groups of PMTs. If at least one of each goes over threshold, the charge content of all analog signals is integrated and the timing of all PMTs over threshold is recorded. Figure courtesy of Hans Wilschut.*

6.2 Measurements

The measurements that are described here were performed to characterize the β detector in terms of its energy, position, and timing resolution; all three will be discussed below. Two different sources were used, a ^{207}Bi and ^{90}Sr source. The bismuth source is useful for energy calibration purposes because of its electron conversion lines at 1 MeV, however, it is also a strong source of γ rays [54]. In contrast, ^{90}Sr produces no γ rays but a continuous electron-energy spectrum as it decays purely through β^- decay (endpoint 546 keV) into ^{90}Y, which itself decays by β^- decay (endpoint 2280 keV) to the stable ground state of ^{90}Zr [55]. The latter endpoint lies close to that of ^{21}Na (2525 keV).

6.2.1 Gain matching of the PMTs

The six PMTs of the ΔE detector, are gain matched using the minimum-ionizing particle peak in the QDC spectrum. The ^{90}Sr source is placed near the rim of the 75 μm foil, close to the PMT under consideration. The coarse gain matching is done by adjusting the HV (typically 1.0 kV). The finer gain matching is done by scaling the QDC readouts in software. The sum of six PMTs (see figure 6.5d for a typical spectrum) is taken to be proportional to the energy deposited in the ΔE detector.

Gain matching the seven tubes of the E detector was slightly more difficult since there is no clear feature as in the ΔE spectrum. The following scheme provides an alternative. The ^{207}Bi source is put right above one of the E PMTs and a QDC spectrum is recorded. It contains contributions from both electrons and gamma rays. This gamma background can be measured by using a 0.9 mm aluminum absorber. Then the electrons are stopped in either in the absorber or the ΔE detector. The difference spectrum makes up an almost perfect exponential and its decay constant is a measure of the relative gain of the PMT.

6.2.2 Energy resolution and photon statistics

One of the limiting factors in resolving the energy deposition is the relatively low number of photons that is produced in the scintillator, 1×10^4 photons/MeV. The minimum ionizing energy in the ΔE detector, 2 mm of NE104, is 0.4 MeV. From direct observations from the oscilloscope it turns out that for minimum ionizing particles ∼10 photons are detected by the PMT coupled to the light

guide nearest to the source. This leads the energy resolution

$$\begin{aligned} \frac{\Delta E_{\text{dep}}}{E_{\text{dep}}} &= \frac{1}{\sqrt{N}} = \frac{0.2}{\sqrt{E_{\text{dep}}}} && (E_{\text{dep}} \text{ in MeV}) \\ &\simeq 30\% && \text{(for minimum ionizing part.)} \end{aligned} \tag{6.1}$$

for the ΔE detector.

The energy resolution of the E detector can be estimated by looking at the geometry of the system. Suppose most of the photons are produced near the surface facing the ΔE detector, 4 cm away from the PMT. If this location is above a PMT, the solid angle subtended by the 25 mm diameter photo-sensitive area is 2%. Again taking a quantum efficiency of 20% one finds

$$\begin{aligned} \frac{\Delta E_{\text{dep}}}{E_{\text{dep}}} &= \frac{0.2}{\sqrt{E_{\text{dep}}}} && (E_{\text{dep}} \text{ in MeV}) \\ &\simeq 15\% && (\text{for } E_{\text{dep}} = 1 \text{ MeV.}) \end{aligned} \tag{6.2}$$

for the E detector.

6.2.3 Position sensitivity

To find the position sensitivity, PMT spectra are measured with varying source positions (see Fig. 6.4). In the following the event trigger requires that at least one PMT of both the ΔE and the E detector is above threshold. The charge content of a pulse is clearly seen to depend on the position of the source relative to the PMT. In principle one can use all thirteen pulses to estimate the hit position. At this point it suffices to present the data in an intuitive manner that reveals the potential quality of position reconstruction.

Position sensitivity in the ΔE detector

If for a certain event ΔE_i represents the QDC value of the tube i, and $\mathbf{r}_i$ the position vector of tube i, then the hit position on the ΔE detector is estimated by

$$\mathbf{x}_{\mathbf{r}} = \frac{\sum_i \Delta E_i \mathbf{r}_i}{\sum_i \Delta E_i}, \tag{6.3}$$

i.e. a weighted average of the tube position vectors.

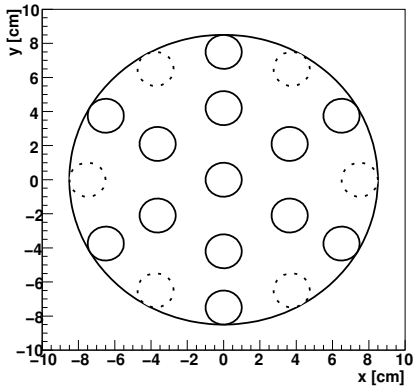

Figure 6.4: *The source positions that were used. The big circle represents the vacuum separation sheet on top of which the source was placed. The 7 inner positions are directly above the PMTs of the E detector. The solid line positions on the outer ring are the nearest possible to a ΔE PMT; the dashed are between two PMT positions.*

Fig. 6.5 shows the results of a measurement with the source close to the rim. A notable feature, most prominent in Fig. 6.5a and 6.5b, is the presence of straight lines. If only two PMTs fire (say 1 and 2) then, by construction, $\mathbf{x}_r$ falls on a line connecting $\mathbf{r}_1$ and $\mathbf{r}_2$. Fig. 6.5b and 6.5c show low and high light output, respectively. One can immediately conclude that the position reconstruction using the ΔE detector is better when more photons are collected.

In Fig. 6.5a and 6.5b the red pixel marks exactly the position of the PMT closest to the source. This happens when only one PMT fires because then $\mathbf{x}_r$ coincides with one of the $\mathbf{r}_i$. Among the minimum ionizing particles 45% of the events are in this pixel. For other source positions, this percentage is different. For a source on the inner ring, it is 13%. The dashed outer ring positions give 20%. In the latter case the events are divided over two pixels corresponding to the two nearest PMTs.

For the source positions on a line connecting the center and a position $\mathbf{r}_i$, especially close to the rim, it is clear that one can conclude in which segment the event is took place. However, for source positions in between two PMTs (dashed circles in Fig. 6.4) the distribution is less sharp peaked. The position resolution of the E detector might help here.

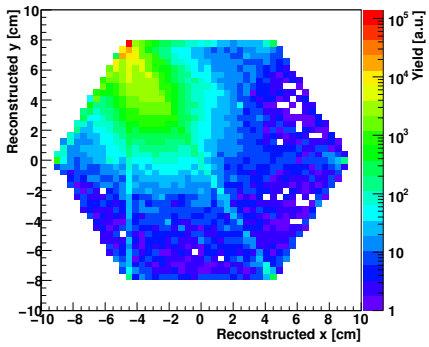

(a) *No cut.*

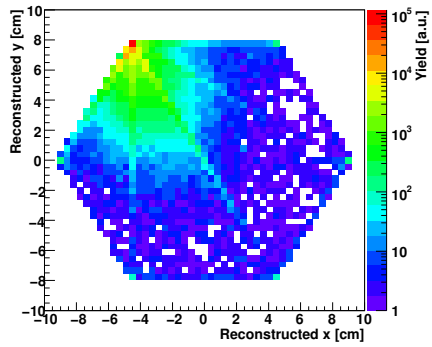

(b) *Minimum ionizing particles (cut 1).*

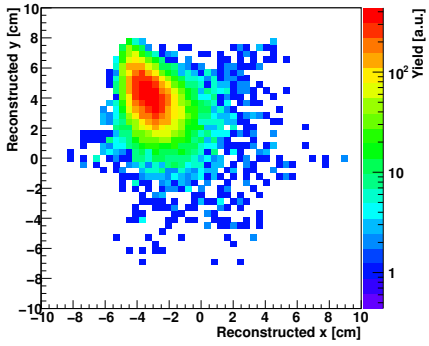

(c) *Higher energy deposition (cut 2).*

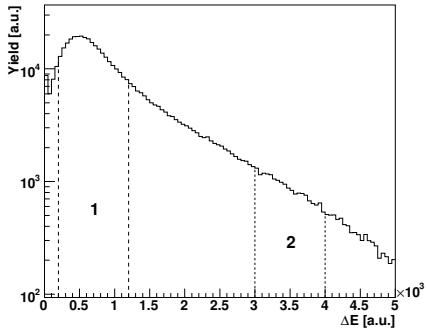

(d) $\sum \Delta E_i$ *spectrum.*

Figure 6.5: *Scatter plots of the event by event position reconstruction with a fixed source position. The figures 6.5b and 6.5c are obtained by applying the cuts as shown in Fig. 6.5d. There is no additional cut in* $\sum E_i$.

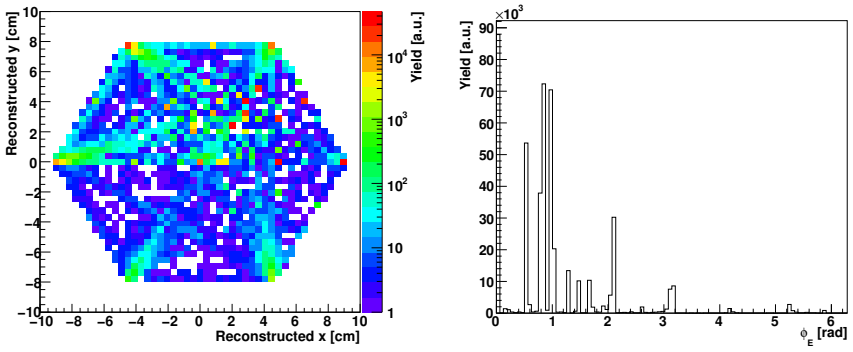

(a) *No cut.* **(b)** *No cut.*

(c) *With minimal E requirement.* **(d)** *With minimal E requirement.*

Figure 6.6: *2D plots: scatter plots of the event by event position reconstruction using the E detector. 1D plots: the polar angle distribution of the events.*

Position sensitivity in the E detector

Fig. 6.6 shows the reconstructed positions of events obtained with the ^{90}Sr source, using the E detector. The source position is the same as in Fig. 6.5. In Fig. 6.6 the intense spots are associated with particular combinations of QDC values that occur very often. Some spots are exactly in between two PMT positions. Apparently the QDC values, after pedestal subtraction) of two PMT signals are then exactly the same. Most likely this happens at very low channel numbers. This is confirmed by imposing a minimal energy requirement ($\sum E_i > E_{\min}$) that removes the hot spots that do not make sense considering current the source position. Comparing figures 6.6a and 6.6b on the one hand and 6.6c and 6.6d on the other, shows that this procedure is necessary.

Combining the ΔE and E detector

To see whether the positions inferred from the ΔE and E detector agree on an event-to-event basis, consider Fig. 6.7. The dashed diagonal line indicates agreement between $\phi_{\Delta E}$ and ϕ_E. Again the ΔE detector is gated on the minimum ionizing particles. The $\phi_{\Delta E}$ distribution is not correlated with ϕ_E. The broad band of events along the dashed line occur at high energy deposits in the E detector. They are more or less uniformly distributed in an (x, y)-plot and are most likely minimum-ionizing cosmic muons. To illustrate this clearer Fig. 6.8 shows the data of many runs at very high $\sum E_i$, so the decay events from the source are not included. A very clear correlation between the two detectors can be seen. The fact that the band lies somewhat above the dashed line stems from the fact that the PMTs of the E detector are slightly rotated with respect to the ΔE detector PMTs, which was not taken into account in the position reconstruction.

For $\sum E_i > E_{\min}$ we are left with only 10% of the events. In 90% of the events the E detector does not give sensible information, even though at least one of its PMTs went over threshold. For this majority of events energy reconstruction seems not to be possible. However, the position information from the ΔE detector works as expected[1]. Fig. 6.9 displays the effect of this 'minimal-energy cut' on the ΔE data. The events above the threshold show a minimum-ionizing peak and a slightly more localized reconstructed position spectrum.

Clearly the energy resolution of the β detector, as it is currently configured, is not working as expected. Its design and operation need to be reconsidered.

[1]Note that we can miss one of the measured parameters and still be able to reconstruct all three momenta in the decay: the set of measured parameters is kinematically overdetermined.

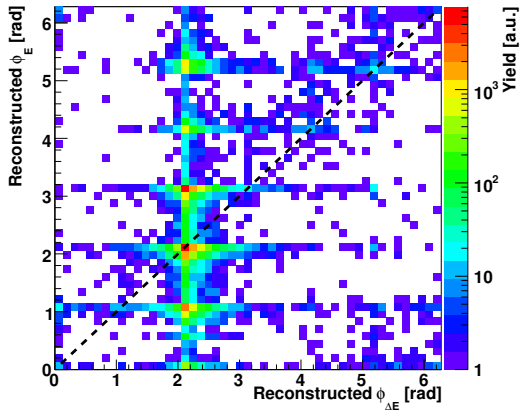

Figure 6.7: *The reconstructed polar angle coordinates: ϕ_E vs $\phi_{\Delta E}$. Ideally all points lie on the dashed line.*

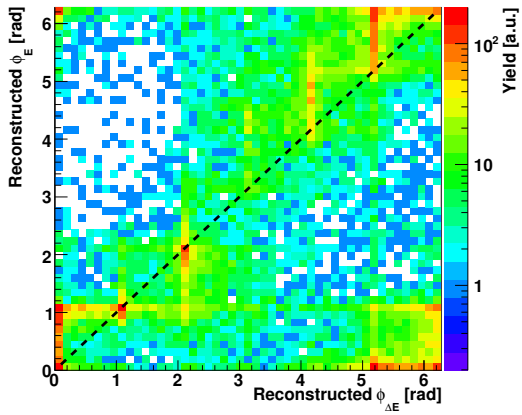

Figure 6.8: *Same as Fig. 6.7, but now many runs are summed and only high $\sum E_i$ events are displayed.*

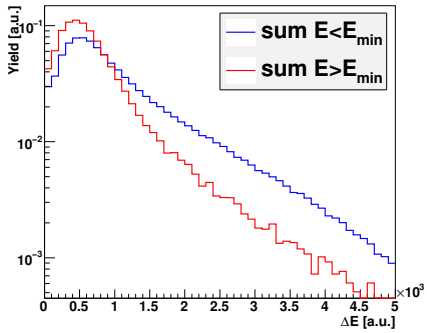

(a) *Two normalized* $\sum \Delta E_i$ *spectra for two different* $\sum E_i$ *cuts.*

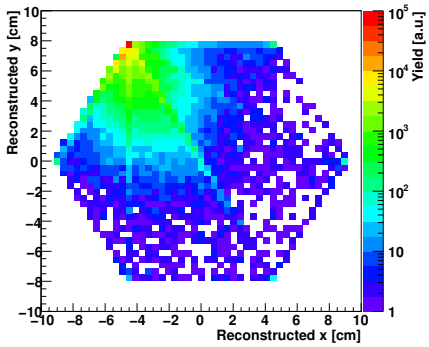

(b) $\sum E_i < E_{min}$.

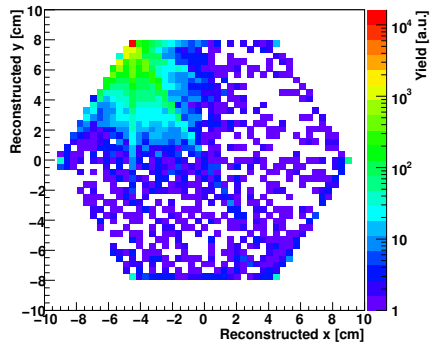

(c) $\sum E_i > E_{min}$.

Figure 6.9: *The effects on the* ΔE *data of making cuts in* $\sum E_i$. *In the two 2D graphs only MIPs are plotted (cut 1 in Fig. 6.5d).*

6.2.4 Timing resolution

For the time-of-flight measurement of the recoil nucleus the start time is given by the β particle. The logic signals from all PMTs go into an MTDC (CAEN V1190B). The time resolution can be established by measuring the relative time between two PMTs, as is shown in Fig. 6.10. In this way we find that the resolution (full width at half maximum or FWHM) of a single ΔE PMT is 3.1 ns and an E PMT is 6.1 ns, see Fig. 6.10a and 6.10b respectively. Taking the weighted average time of one ΔE and one E-PMT pulse gives a resolution 2.7 ns. The end of the flight of the ion is determined by the MCP. Combining the MCP's timing resolution from section 5.3.1 we find a TOF resolution (FWHM) of 3.2 ns. With a total TOF between 1.1 and 1.7 μs the relative precision is about 0.3%.

Also concerning the time resolution of the β detector we had expected better results (∼1 ns) which is a further reason to reconsider the current design.

6.2.5 Discussion

In chapter 3 we saw that several properties of the β detector need to be understood in detail to control the systematic errors. For a discussion of the timing resolution see section 5.3.3. Another important aspect is the response function of the β detector. A beam of mono energetic positrons hitting the particles is spread out over a broad range of QDC channels [38], so setting a software threshold at certain QDC channel creates a smooth low energy cutoff. This requires more study and should be modeled correctly in the Monte Carlo simulation of the experiment.

In general we experienced some performance issues with the β detector which probably have to do with a bad coupling of the PMTs to the light guide. In contrast to other, similar experiments we use more than one PMT in the ΔE- and E detector. This allows us to some extent to measure the hit position of the β particle but makes it more challenging to characterize the more complex response, as a function of both energy and position. Since this is a critical issue, we need to reconsider the design of the β detector.

6.3 Conclusions

In this chapter we discussed the design and the performance of the β detector. It consists of two layers of scintillator plastic. The thin layer is the ΔE detector

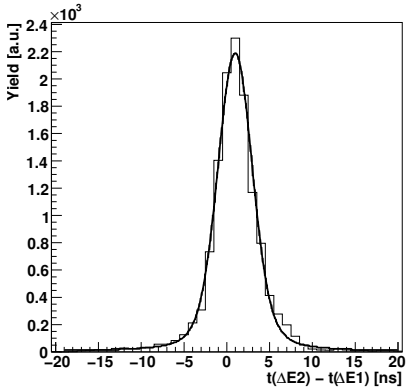

(a) $t(\Delta E_2) - t(\Delta E_1)$; *FWHM = 4.4 ns*

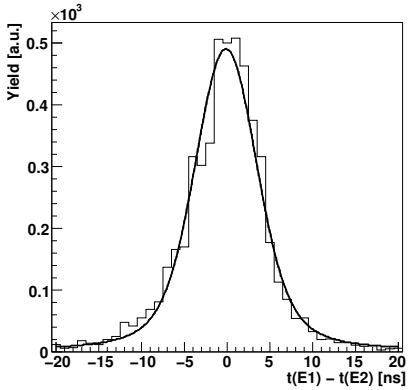

(b) $t(E_1) - t(E_2)$; *FWHM = 8.7 ns*

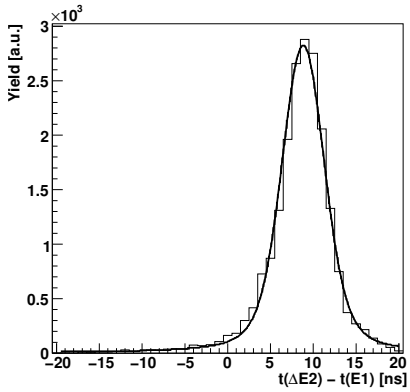

(c) $t(\Delta E_2) - t(E_1)$; *FWHM = 6.1 ns*

Figure 6.10: *Timing resolution of the β detector. The ^{90}Sr source was positioned at the rim closest to ΔE_3. E_1 is the nearest E PMT. The purpose of the fitted Voigt functions is to extract the widths from the distributions.*

and the thick layer is the E detector. The light produced in the scintillator material is collected by several PMTs.

The β detector was tested with a ^{207}Bi source and a ^{90}Sr source. We can draw the following conclusions:

- Position resolution: we can determine in which of the six segments the β detector was hit.
- Timing resolution: the β detector starts the TOF measurement with a resolution of 2.7 ns (FWHM).
- Energy resolution: for both the ΔE and the E detector we found $\sigma_{E_d}/E_d = 0.2/\sqrt{E_d}$, where E_d is the deposited energy in MeV.

The threshold is determined from a simulation and was found to be around 1 MeV. More study is necessary to find a more precise value (and shape) of the threshold, as we know from chapter 3 is necessary to reduce the systematic error in a measurement of the β-ν correlation parameter a. To arrive at a detector that can be understood well enough one needs to reconsider the design.

CHAPTER 7

Summary and outlook

This thesis describes the steps towards a correlation measurement in nuclear β decay of ^{21}Na to search for physics beyond the Standard Model. Our experiment uses a Magneto-Optical Trap (MOT) to provide a source of radioactive ^{21}Na atoms. A combination of recoil and β detection allows for the measurement of several decay-correlation parameters (introduced in equation 2.8) that are sensitive to this "new physics".

Since the beginning of this experiment the goal has been to perform a precise measurement of the TRV coefficient D, which is related to the imaginary part of one of the coupling constants ($\mathrm{Im}(a_{LR})$) in the Hamiltonian, see chapter 2. It was known that the limits on electric dipole moments (EDMs) put an upper bound on D. However, leptoquark models appeared not to be bound by this. Recently this viewpoint has changed, and limits were calculated using the EDM limits and the leptoquark model [26]. According to Ref. [29] these calculated limits are too strong and should be taken a factor 10 weaker. Therefore the bounds from EDM measurements are 1-100 times stronger than the best measurement of D. Given the limit from the best measurement, and the precision with which the final-state interactions are calculated, there is still a window of opportunity motivating a D measurement. In addition, it is often argued that direct limits avoid possible fine-tuning arguments.

In chapter 2 we also explored the current bounds on coupling constants that parametrize other types of new physics. In particular the scalar (S) and tensor (T) couplings. The coefficients for the β- correlation, $\tilde{a}$ and the β asymmetry, $\tilde{A}$, are sensitive to these types of interactions, primarily through the Fierz interference term, b (see Eqs. (2.17) and 2.18)).

A measurement of the β-ν correlation parameter, $\tilde{a}$, could contribute to the improvement of right-handed scalar interactions, A_R. The left-handed interactions, A_L, are already strongly bound by the $0^+ \to 0^+$ measurements (see Fig. 2.1). We found that, using ^{21}Na, a precision of 0.8% is necessary to improve on the current bound, where we assume the absence of tensor interactions. These left- and right-handed tensor interactions (α_L and α_R) are better pursued using pure Gamow-Teller transitions, such as the decay of ^{6}He [19, 56]. It was noted that measurements of neutrino masses put a much stronger bound on A_R (and α_R) than β-decay experiments have done. This makes more precise measurements of $\tilde{a}$ less attractive. Measuring the β-asymmetry parameter, $\tilde{A}$, using ^{21}Na, can improve the bound on left-handed tensor interactions, α_L. We found that a precision of 0.6‰ is needed to improve the current best bound. This certainly is challenging; the highest precision reached so far is 1.4% with ^{114}In [45].

Correlation measurements are relevant for a different reason. Combining the correlation and lifetime measurements of mirror nuclei would add to the precision of $|V_{\mathrm{ud}}|$, A_L and α_L in a way that is similar to what has been done for superallowed $0^+ \to 0^+$ transitions. This is described in [12].

To be able to perform a precise measurement of a, A or D there are several crucial requirements. One needs a good understanding of the setup to control the systematic effects and a high statistical accuracy.

The understanding of the setup lies partly in a detailed simulation of the experiment. In this work a simulation was performed that was not intended to determine the required statistics. The simulation was purely geometrical; the β particle did or did not hit a disc in space, representing the β detector and for the recoil ion the time of flight and hit position were calculated assuming a ballistic orbit to the MCP. We used the simulation to calculate N_{d}, which is the number of atoms that need to be captured and decay in the second MOT chamber where the correlation measurement is done, based on the required precision found in chapter 2. The results are summarized in table 7.2. To be able to analyze actual data, we need a detailed understanding and modeling of the background caused

by positron annihilation, back-scattered β particles and other effects.

In addition to the aspects of the detectors that were discussed in chapters 5 and 6, more detailed knowledge of the response of the detectors needed. For both the MCP and the β detector a spatial-uniformity study should be performed. Due to its design, we suspect that the β detector has a rather complex response as a function of hit position that will be challenging to model in enough detail for a simulation. One should reconsider whether the benefits of position resolution outweigh the extra complexity that comes with it, especially in view of the rather poor position resolution with the current design.

To observe enough decays in a reasonable amount of time, the whole chain of efficiencies, from the production to the transport and re-trapping in the second chamber (chapter 4), needs to be optimized. Table 7.1 gives the yield of ^{21}Na at, and the efficiency of, several stages in the experiment; the values are taken from [44], and are shown in the columns labeled "Current". With this number of atoms trapped per second in the second MOT, it would take too much time to perform a measurement of a, A or D. Therefore, an improvement at various stages is required.

In the thesis of Wilbert Kruithof [44] the trapping efficiency in the collector MOT was identified as the main bottleneck and thus an important opportunity for improvement. The trapping efficiency in the MOT depends on the capture probability of an atom for a single pass through the laser volume and the number of such passes. The number of passes can be increased by applying an anti-sticking coating that allows the atoms to bounce up to hundreds of times, thus increasing the trapping efficiency by a large factor. Thus far we have no evidence of a working coating. The chemical procedure of applying requires some more dedication and practice. One should gain some experience in judging the quality of the coating by doing simple tests such as the 'droplet test'. A convincing description of the physics of such a coating is lacking, making improvements difficult. Therefore, collaboration with groups using these anti-sticking coatings would be beneficial.

Other stages that need to be considered are the primary beam and production target, the extraction from the thermal ionizer (TI), the ion transport trough the low energy beam line (LEBL), and the atom transfer from the first to the second MOT. The power of the primary beam hitting the target is currently limited by the heat dissipation in the target window. A higher beam current lead to destruction of the window. It seems feasible to gain a factor of 10 here by increasing the target pressure and beam current once a solution is found to dissipate the heat in the window in a more efficient way. The extraction efficiency of the TI is not a limit. It was shown that it can be increased from 10%

Step	Current		Projected	
	Efficiency	Rate (s^{-1})	Efficiency	Rate (s^{-1})
Into TI		3.0×10^6		3.0×10^7
Extraction from TI	0.1	3.0×10^5	0.5	1.5×10^7
Onto neutralizer	0.2	6×10^4	0.5	7.5×10^6
Neutralizer release	0.3	1.8×10^4	0.3	2.3×10^6
Capture in 1^{st} MOT	2.4×10^{-4}	4.7	0.01	2.3×10^4
Recapture in 2^{nd} MOT	4.8×10^{-2}	0.22	0.5	1.1×10^4

Table 7.1: *The yield of ^{21}Na at various stages of the setup. The efficiency of each step is also given. The "Projected" column states the improvements that are discussed in the main text.*

to 50% when the temperature is raised from 2500 K to 2800 K [43, 44]. Also, given the current configuration using a pulsing drift tube, the ion-transport efficiency through the LEBL can be at most 50%. The current efficiency of 20% is probably related to the emittance of and transport through the LEBL. Both aspects can be improved using a properly operating radio-frequency cooler and buncher (RFQ). In table 7.1 we take 50%. Finally, the atom-transfer efficiency between the two MOTs can be higher than 50% [44], once the compression stage (funnel) is properly working. We assume that 50% can be achieved.

All these improved factors are used in the "Projected" column in table 7.1. Using the resulting yield and the required number of events, we calculate the projected measurement times in the last column of table 7.2.

In this work we have identified several critical issues that need to be resolved in order to come to a successful experiment. The possible systematic errors require a well understood detection system and for this reason the present system needs further characterization and improvement. To gain the required statistics the production of ^{21}Na is sufficient in view of the available primary beam, but the delivery of the radioactive beam is not yet sufficient. The experiment can well be done, once the above mentioned improvements are implemented.

Par.	Method	Precision	N_{d}	Projected measurement time
a	Fit to E_r	0.8%	7×10^7	1.7 h
	Fit to TOF (β)		1×10^8	2.5 h
	Fit to TOF (s.o.)		9×10^7	2.2 h
A	β-asym.	0.6‰	6×10^7	1.5 h
D	Cyl. detectors	4×10^{-4}	4×10^{10}	39 d
	$2 \times 2\pi$ detectors		2×10^{10}	19 d

Table 7.2: *A summary of the measurements of the correlation parameters a, A, and D. Here E_r refers to the recoil-ion energy distribution and TOF refers to the recoil time-of-flight distribution that was started either by measuring a β^+ particle or a shake-off electron. The required precision (sigma) and the number of decays in the MOT are calculated in chapter 2 and 3, respectively. The last column shows the expected measurement time assuming the yield in the right column of table 7.1.*

Nederlandse Samenvatting

Inleiding

Op het Kernfysisch Versneller Instituut (KVI) in Groningen is de TRIμP faciliteit gebouwd voor de productie van radioactieve isotopen. Radioactief verval wordt veroorzaakt door krachten en interacties die het hart van de hedendaagse deeltjesfysica vormen. Het nauwkeurig bestuderen van de vervalsprocessen maakt het mogelijk te zoeken naar nieuwe of nog onbekende fenomenen; "nieuwe natuurkunde".

Het Standaardmodel (SM) beschrijft *alle* deeltjes en, behalve de zwaartekracht, *alle* interacties die we op dit moment kennen. De grote verscheidenheid aan fenomenen in de natuur is verbazingwekkend genoeg terug te brengen tot vier fundamentele interacties: de zwaartekracht, de electromagnetische interactie, de zwakke interactie en tot slot de sterke interactie. Het SM vat alles behalve de zwaartekracht samen.

Met groot succes heeft het SM vele experimentele tests doorstaan. Er zijn echter nog veel open vragen en nog meer alternatieve theoriëen om een antwoord te geven op deze vragen. Door experimenten uit te voeren, worden de voorgestelde theoriën op de proef gesteld en kunnen die in speelruimte worden beperkt of zelfs worden afgeschreven.

Een belangrijk concept in de deeltjes fysica is symmetrie. Ze komen in verschillende vormen voor maar we beperken ons hier tot de zogenaamde discrete symmetrieën. Bij elke symmetrie hoort een symmetrie-operatie. Wanneer een theorie, of beter gezegd de observabelen, onder deze operatie niet veranderd, zeggen we dat de theorie 'invariant is onder die operatie'. Neem als voorbeeld spiegelsymmetrie ('pariteit'). De Newtonse mechanica die de beweging

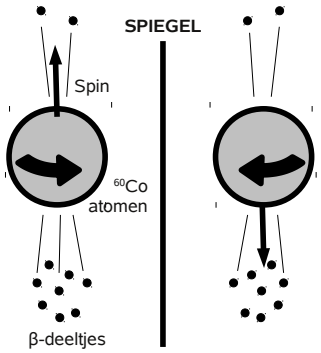

Figuur 7.1: *De breking van spiegelsymmetrie in radioactief verval. De spin- en draairiching zijn via de rechterhand- of kurkentrekkerregel gekoppeld. In het gespiegelde proces worden de β-deeltjes vooral in de richting van de spin uitgezonden, waar dat in het echte proces precies andersom is. Het gespiegelde proces volgt dus niet dezelfde regels.*

van alle voorwerpen in het dagelijks leven uitstekend beschrijft, is invariant onder spiegeling. Stel, iemand toont een videofragment met twee botsende biljartballen en stelt de vraag: 'Zit je hier naar de werkelijke situatie te kijken of zijn de beelden gespiegeld?' Deze vraag is onmogelijk te beantwoorden omdat zowel de normale als de gespiegelde versie van het proces evengoed kunnen voorkomen. Dit is terug te zien in de wiskundige formulering van de Newtonse mechanica. Wanneer de 'wereld' gespiegeld wordt, blijven alle formules onveranderd.

Het bijzondere is nu dat op het niveau van de elementaire deeltjes er van deze spiegelsymmetrie geen sprake meer is. Dit is in 1957 experimenteel vastgesteld. Men vond dat de electronen (β-deeltjes) die bij het radioactieve verval van ^{60}Co werden uitgezonden met name *tegen de richting van de spin* in werden uitgezonden. Hieruit blijkt dat de spiegelsymmetrie gebroken is: in een spiegel keert de draairichting (=spinrichting) om, maar de electronen gaan nog steeds dezelfde kant uit. Met andere woorden, de β-deeltjes bewegen nu voornamelijk *met de spin mee*. De gespiegelde variant van het proces voldoet niet aan dezelfde wetmatigheden en de theorie die dit beschrijft moet dus niet invariant zijn onder spiegeling.

Naast deze spiegelsymmetrie spelen er in de deeltjesfysica nog twee an-

dere symmetrieën een belangrijke rol: tijdsomkeringssymmetrie en ladingssymetrie. De Newtonse mechanica is ook invariant onder tijdsomkering: een achterstevoren afgespeelde video van een botsing van twee biljartballen ziet er net zo natuurlijk uit als de normale variant. In het ^{21}Na β-vervalexperiment gaan we op zoek naar een schending van deze tijdsomkering op sub-atomaire schaal.

Het ^{21}Na experiment dat op het KVI wordt uitgevoerd is in zekere zin vergelijkbaar met het ^{60}Co experiment: er wordt gekeken naar β deeltjes die uitgezonden worden bij het verval. Maar omdat we een andere symmetrie bestuderen, zijn er andere vereisten: naast de β-deeltjes moeten we ook de dochterkern observeren. Dit is alleen mogelijk wanneer de radioactieve atomen min of meer vrij in de ruimte 'zweven'. Dat doen we met een atoomval. Laserlicht en magneetvelden houden de atomen bijeen in een volume van ongeveer 1 mm^3. Wanneer een atoom vervalt verlaten het β-deeltje en de dochterkern de val en kunnen ze gedetecteerd worden.

In dit proefschrift

In dit proefschrift wordt het ^{21}Na β-vervalexperiment beschreven. Drie onderwerpen staan centraal: (1) een simulatie van het experiment, het testen en karakteriseren van (2) de β-detector en van (3) de dochterkerndetector. Het vangen en afkoelen van de natriumatomen heeft een belangrijke rol gespeeld in het onderzoek, maar is reeds uitgebreid beschreven in het proefschrift van Wilbert Kruithof [44].

De simulatie is uitgevoerd om in te schatten hoeveel atomen we in de val moeten laten vervallen voordat we de gewenste precisie hebben gehaald: hoe meer 'statistiek je verzameld', des te groter is de precisie die je kunt halen. Zoals blijkt uit eerdere metingen weten we dat een evenentuele schending van tijdsomkering een zeer klein effect is, kleiner dan 1 op 10.000, wat een grote hoeveelheid data vereist. De uitkomst van de simulatie is dat we ca. 2×10^{10} (tweehonderd miljard) deeltjes moeten laten vervallen om de huidige limiet te verscherpen. Met de simulatie was het ook mogelijk om enkele systematische effecten te bestuderen (verschuivingen in meetuitkomsten door imperfecties van de opstelling).

De β-detector is getest met behulp van radioactieve bronnen, ^{90}Sr en ^{207}Bi. De bron is op verschillende plaatsen op de detector gelegd om te testen of we met de dedector de inslagpositie van het β-deeltje kunnen reconstrueren. Uit de meting is gebleken dat de zogenaamde ΔE detector een betere positieresolutie heeft dan de E detector. Verder is gebeleken dat de tijdsresolutie 2.7 ns

(FWHM) is.

De dochterkerndetector is getest en gekarakteriseerd door gebruik te maken van het stabiele ^{23}Na. Dit werd ingevangen in de atoomval, door een gepulseerde laser geïoniseerd en tenslotte naar de detector geleid in een elektrisch veld. De detector heeft twee taken. Ten eerste het meten van de vluchttijd van de dochterkern van de atoomval naar de detector, waarbij de detectie van het β-deeltje de meting start. Ten tweede moet de inslagpositie van de dochterkern worden gemeten. Dit wordt gedaan door een *Multi Channel Plate* (MCP, te vergelijken met een versterker) te combineren met een *delay line detector*, welke de daadwerkelijke positiemeting mogelijk maakt. Met deze twee gegevens is het mogelijk te berekenen in welke richting en met welke snelheid het ion de val heeft verlaten. De precisie waarmee dit gebeurt, is gemeten: de positieresolutie is 0.3 mm, (σ) en de tijdsresolutie is 1.8 ns (FWHM). Gecombineerd met de β-detector is de resolutie van de vluchttijdmeting 3.2 ns (FWHM).

Voor het uiteindelijke experiment is een meer gedetailleerde karakterisering van de detectors nodig om de systematische fouten onder controle te houden. Zo moet bijvoorbeeld de positie-afhankelijke detectie-efficiëntie gemeten worden. Verder is het aan te raden om het ontwerp van de β detector te herzien voor beter te interpreteren detector 'output'.

Omdat het van belang is dat er veel radioactieve vervallen gedetecteerd worden moet er zuinig omgesprongen worden met de geproduceerde ^{21}Na. Op dat vlak zijn nog verbeteringen nodig en ook mogelijk. Als deze doorgevoerd zijn, is een tijdsomkeringssymmetriemeting met de vereiste precisie binnen een acceptabel tijdsbestek mogelijk.

Dankwoord

Nu mijn promotie-onderzoek en mijn tijd op het KVI voorbij zijn, wil ik graag de mensen bedanken die het interessant, gezellig, leerzaam of überhaupt mogelijk gemaakt hebben.

Ik begin met mijn promotor Hans. I decided to thank everyone in his or her moedertaal, so hier gaan we dan. Bedankt voor de begeleiding in de afgelopen jaren, voor het geduld necessary to fill the gaps in my nuclear physics knowledge, and finally het snelle lezen van de many revisions of this thesis.

I thank my reading committee members prof. G. Ban, prof. A. Pellegrino and prof. Y. Sakemi for carefully reading my manuscript and providing me with useful comments.

Wilbert, met veel plezier heb ik de afgelopen jaren met je samengewerkt. Je was de perfecte sparringpartner in de vele, vele discussies die we hebben gehad, welke allerminst beperkt bleven tot natuurkunde.

Jos, bedankt voor de vele gezellige pauzes, de vele gesprekken en discussies en dat je mijn paranimf wilt zijn.

Lotje, allereerst bedankt dat je mijn paranimf wilt zijn. Bedankt voor de hulp die je ons vaak geboden hebt. En natuurlijk: jij en Wilbert zijn onvergetelijke wandelpartners!

Ook bedank ik bij dezen de wetenschappelijke staf binnen de TRIμP groep, Gerco, Klaus, Lorenz en Steven, voor de dagelijkse begeleiding en het delen van kennis en ervaring.

Oscar, je was een fijne kamergenoot, en natuurlijk een gezellige reisgenoot in de afgelopen jaren.

Meneer Leo, enorm bedankt voor de niet te evenaren hulp bij ons project. Met veel plezier heb ik met je samengewerkt!

Sander, met de vele, vele uren die je in ons experiment hebt gestoken was je een trouwe en nuttige hulp. We gaan vast nog wel eens een rondje fietsen.

Alle promovendi, postdocs en technisch personeel uit de TRIμP groep: Joost, Corine, Mayerlin, Amita, Sreekanth, Bodda, Auke, Elwin, Otto, Stephan und der Olli (thanks for getting all the Moghul food!); dank!

Voor de eerste hulp bij theorievragen bedank ik Rob Timmermans, Lotje Wansbeek, Jordy de Vries en Keri Vos. Rob, bedankt voor het doorspitten en het helpen verbeteren van het theoriehoofdstuk in dit proefschrift.

Iedereen uit de ATF groep: bedankt voor het delen van het koffiehok en de gezelligheid aldaar.

Graag wil ik iedereen van de Cyclotrongroep bedanken voor alle ondersteuning tijdens de bundeltijden.

Zonder de ondersteunende afdelingen kan een experiment op het kvi niet bestaan. Daarom wil ik bij dezen iedereen van de mechanische werkplaats (Dirk, tige dank foar het betrouwbare en snelle puntlassen!), de vacuümdienst, de electronica-afdeling en de tekenkamer hartelijk bedanken voor hun bijdrage.

Stoica's, bedankt voor de diners en spelletjesavonden! Wordt vervolgd...

Ik bedank de oud-promovendi, in willekeurige volgorde: Moslem, Subadheep, Gouri, Emil en Marlène.

Karin, al was het alleen maar in het laatste jaar, erg bedankt voor je steun en liefde.

Tot slot wil ik mijn ouders, broer en zus bedanken voor een nooit aflatende steun en interesse. Bedankt!!

Bibliography

[1] E. Fermi. Versuch einer Theorie der β-Strahlen. I. *Zeitschrift fr Physik A Hadrons and Nuclei*, 88:161–177, 1934. 10.1007/BF01351864.

[2] T. D. Lee and C. N. Yang. Question of Parity Conservation in Weak Interactions. *Phys. Rev.*, 104:254–258, Oct 1956.

[3] C. S. Wu, E. Ambler, R. W. Hayward, D. D. Hoppes, and R. P. Hudson. Experimental Test of Parity Conservation in Beta Decay. *Phys. Rev.*, 105:1413–1415, Feb 1957.

[4] Richard L. Garwin, Leon M. Lederman, and Marcel Weinrich. Observations of the Failure of Conservation of Parity and Charge Conjugation in Meson Decays: the Magnetic Moment of the Free Muon. *Phys. Rev.*, 105:1415–1417, Feb 1957.

[5] P. Herczeg. Beta Decay Beyond the Standard Model. *Progress in Particle and Nuclear Physics*, 46:413–457, 2001.

[6] W. Greiner and B. Müller. *Gauge Theory of Weak Interactions*. Springer-Verlag Berlin Heidelberg New York, 3 edition, 2000.

[7] J. D. Jackson, S. B. Treiman, and H. W. Wyld. Possible Tests of Time Reversal Invariance in Beta Decay. *Phys. Rev.*, 106(3):517–521, May 1957.

[8] M.E. Ebel and G. Feldman. Further remarks on Coulomb corrections in allowed beta transitions. *Nuclear Physics*, 4(0):213 – 214, 1957.

[9] Nathal Severijns, Marcus Beck, and Oscar Naviliat-Cuncic. Tests of the standard electroweak model in nuclear beta decay. *Rev. Mod. Phys.*, 78:991–1040, Sep 2006.

[10] P. Herczeg and I. B. Khriplovich. Time-reversal violation in β decay in the standard model. *Phys. Rev. D*, 56:80–89, Jul 1997.

[11] J. C. Hardy and I. S. Towner. Superallowed $0^+ \to 0^+$ nuclear β decays: A new survey with precision tests of the conserved vector current hypothesis and the standard model. *Phys. Rev. C*, 79:055502, May 2009.

[12] O. Naviliat-Cuncic and N. Severijns. Test of the Conserved Vector Current Hypothesis in $T = 1/2$ Mirror Transitions and New Determination of $|V_{ud}|$. *Phys. Rev. Lett.*, 102:142302, Apr 2009.

[13] E. G. Adelberger, C. Ortiz, A. García, H. E. Swanson, M. Beck, O. Tengblad, M. J. G. Borge, I. Martel, H. Bichsel, and the ISOLDE Collaboration. Positron-Neutrino Correlation in the $0^+ \to 0^+$ Decay of ^{32}Ar. *Phys. Rev. Lett.*, 83:1299–1302, Aug 1999.

[14] P. A. Vetter, J. R. Abo-Shaeer, S. J. Freedman, and R. Maruyama. Measurement of the β-ν correlation of ^{21}Na using shakeoff electrons. *Phys. Rev. C*, 77:035502, Mar 2008.

[15] A. Gorelov, D. Melconian, W. P. Alford, D. Ashery, G. Ball, J. A. Behr, P. G. Bricault, J. M. D'Auria, J. Deutsch, J. Dilling, M. Dombsky, P. Dubé, J. Fingler, U. Giesen, F. Glück, S. Gu, O. Häusser, K. P. Jackson, B. K. Jennings, M. R. Pearson, T. J. Stocki, T. B. Swanson, and M. Trinczek. Scalar Interaction Limits from the β-ν Correlation of Trapped Radioactive Atoms. *Phys. Rev. Lett.*, 94:142501, Apr 2005.

[16] Takeyasu M. Ito and Gary Prézeau. Neutrino Mass Constraints on β Decay. *Phys. Rev. Lett.*, 94:161802, Apr 2005.

[17] R. Huber, J. Lang, S. Navert, J. Sromicki, K. Bodek, St. Kistryn, J. Zejma, O. Naviliat-Cuncic, E. Stephan, and W. Haeberli. Search for Time-Reversal Violation in the β Decay of Polarized ^{8}Li Nuclei. *Phys. Rev. Lett.*, 90:202301, May 2003.

[18] V. A. Wichers, T. R. Hageman, J. van Klinken, H. W. Wilschut, and D. Atkinson. Bounds on right-handed currents from nuclear beta decay. *Phys. Rev. Lett.*, 58:1821–1824, May 1987.

[19] C. H. Johnson, Frances Pleasonton, and T. A. Carlson. Precision Measurement of the Recoil Energy Spectrum from the Decay of He^6. *Phys. Rev.*, 132:1149–1165, Nov 1963.

[20] F. Glück. Order- radiative correction to ^{6}He and ^{32}Ar β decay recoil spectra. *Nuclear Physics A*, 628(3):493 – 502, 1998.

[21] F. Wauters, I. Kraev, D. Zákoucký, M. Beck, M. Breitenfeldt, V. De Leebeeck, V. V. Golovko, V. Yu. Kozlov, T. Phalet, S. Roccia, G. Soti, M. Tandecki, I. S. Towner, E. Traykov, S. Van Gorp, and N. Severijns. Precision measurements of the ^{60}Co β-asymmetry parameter in search for tensor currents in weak interactions. *Phys. Rev. C*, 82:055502, Nov 2010.

[22] Shung ichi Ando, Judith A. McGovern, and Toru Sato. The D coefficient in neutron beta decay in effective field theory. *Physics Letters B*, 677(12):109 – 115, 2009.

[23] Marc van Veenhuizen. Time-reversal violation in nuclear β-decay of ^{19}Ne and ^{12}Na. Master's thesis, University of Groningen, Aug 2002.

[24] H. P. Mumm, T. E. Chupp, R. L. Cooper, K. P. Coulter, S. J. Freedman, B. K. Fujikawa, A. García, G. L. Jones, J. S. Nico, A. K. Thompson, C. A. Trull, J. F. Wilkerson, and F. E. Wietfeldt. New Limit on Time-Reversal Violation in Beta Decay. *Phys. Rev. Lett.*, 107:102301, Sep 2011.

[25] A. L. Hallin, F. P. Calaprice, D. W. MacArthur, L. E. Piilonen, M. B. Schneider, and D. F. Schreiber. Test of Time-Reversal Symmetry in the β Decay of ^{19}Ne. *Phys. Rev. Lett.*, 52:337–340, Jan 1984.

[26] John Ng and Sean Tulin. CP violation in beta decay and electric dipole moments. *Phys. Rev. D*, 85:033001, Feb 2012.

[27] P. Herczeg. The T-Odd R and D Correlations in Beta Decay. *Journal of Research of the National Institute of Standards and Technology*, 110:453–459, 2005.

[28] C. A. Baker, D. D. Doyle, P. Geltenbort, K. Green, M. G. D. van der Grinten, P. G. Harris, P. Iaydjiev, S. N. Ivanov, D. J. R. May, J. M. Pendlebury,

J. D. Richardson, D. Shiers, and K. F. Smith. Improved Experimental Limit on the Electric Dipole Moment of the Neutron. *Phys. Rev. Lett.*, 97:131801, Sep 2006.

[29] J. de Vries, E. Mereghetti, R.G.E. Timmermans, and U. van Kolck. The Effective Chiral Lagrangian from Dimension-Six Parity and Time-Reversal Violation. *In preparation.*

[30] R.B. Firestone. Nuclear Data Sheets 103, 269, 2004.

[31] N. Severijns, M. Tandecki, T. Phalet, and I. S. Towner. Ft values of the $T = 1/2$ mirror β transitions. *Phys. Rev. C*, 78(5):055501, Nov 2008.

[32] ROOT data analysis framework. http://root.cern.ch/drupal.

[33] Pierre Hovongton, Dominique Drouin, et al. "monte CArlo SImulation of electroN trajectory in sOlids" (CASINO). http://www.gel.usherbrooke.ca/casino/index.html. Developed at Université de Sherbrooke, Québec, Canada.

[34] M. Sohani. *Setup for Precise Measurements of β-decay in Optically Trapped Radioactive Na.* PhD thesis, University of Groningen, 2008.

[35] N. D. Scielzo, S. J. Freedman, B. K. Fujikawa, and P. A. Vetter. Recoil-ion charge-state distribution following the β^+ decay of ^{21}Na. *Phys. Rev. A*, 68:022716, Aug 2003.

[36] P. Vetter, J. Abo-Shaeer, S. Freedman, and R. Maruyama. *Measurement of the Beta-Neutrino Correlation of Sodium-21 using Shakeoff Electrons.* May 2008.

[37] N.D. Scielzo, S.J. Freedman, B.K. Fujikawa, I. Kominis, R. Maruyama, P.A. Vetter, and J.R. Vieregg. Detecting shake-off electron-ion coincidences to measure -decay correlations in laser trapped 21Na. *Nuclear Physics A*, 746(0):677 – 680, 2004.

[38] A. Gorelov. *Positron-Neutrino Correlation Measurements in the Beta Decay of Magneto-Optically Trapped ^{38m}K Atoms.* PhD thesis, Simon Fraser University, Summer 2008. See paragraph 3.10, equation 3.16.

[39] D. Melconian, J.A. Behr, D. Ashery, O. Aviv, P.G. Bricault, M. Dombsky, S. Fostner, A. Gorelov, S. Gu, V. Hanemaayer, K.P. Jackson, M.R. Pearson, and I. Vollrath. Measurement of the neutrino asymmetry in the decay of laser-cooled, polarized 37K. *Physics Letters B*, 649(5-6):370 – 375, 2007.

[40] E. Traykov, A. Rogachevskiy, M.B Bosswell, U. Dammalapati, P. Dendooven, O.C. Dermois, K. Jungmann, C.J.G. Onderwater, M. Sohani, L. Willmann, H.W. Wilschut, and A.R. Young. Production of radioactive nuclides in inverse reaction kinematics. *Nuclear Instruments and Methods in Physics Research, Section A: Accelerators, Spectrometers, Detectors and Associated Equipment*, 572(2):580–584, 2007. cited By (since 1996) 9.

[41] G.P.A. Berg, O.C. Dermois, U. Dammalapati, P. Dendooven, M.N. Harakeh, K. Jungmann, C.J.G. Onderwater, A. Rogachevskiy, M. Sohani, E. Traykov, L. Willmann, and H.W. Wilschut. Dual magnetic separator for. *Nuclear Instruments and Methods in Physics Research Section A: Accelerators, Spectrometers, Detectors and Associated Equipment*, 560(2):169 – 181, 2006.

[42] Emyl Traykov. *Production of radioactive beams for atomic trapping.* PhD thesis, University of Groningen, Mar 2006.

[43] P.D. Shidling, G.S. Giri, Jungmann K. Van Der Hoek, D.J., W.L. Kruithof, C.J.G. Onderwater, B. Santra, Versolato O.O. Sohani, M., L. Willmann, and H.W. Wilschut. Thermalization of different alkali and alkali-earth elements at the TRIμP facility. *Nuclear Instruments and Methods in Physics Research, Section A: Accelerators, Spectrometers, Detectors and Associated Equipment*, 622(1):11–16, 2010.

[44] Wilbert Kruithof. *Laser trapping of sodium isotopes for a high-precision β-decay experiment.* PhD thesis, University of Groningen, 2012.

[45] F. Wauters, V. De Leebeeck, I. Kraev, M. Tandecki, E. Traykov, S. Van Gorp, N. Severijns, and D. Zákoucký. β asymmetry parameter in the decay of ^{114}In. *Phys. Rev. C*, 80:062501, Dec 2009.

[46] M. A. Rowe, S. J. Freedman, B. K. Fujikawa, G. Gwinner, S.-Q. Shang, and P. A. Vetter. Ground-state hyperfine measurement in laser-trapped radioactive ^{21}Na. *Phys. Rev. A*, 59:1869–1873, Mar 1999.

[47] Daniel A. Steck. Sodium D Line Data. Available online at http://steck.us/alkalidata (revision 2.1.4, 23 December 2010).

[48] E. Liénard, M. Herbane, G. Ban, G. Darius, P. Delahaye, D. Durand, X. Fléchard, M. Labalme, F. Mauger, A. Mery, O. Naviliat-Cuncic, and D. Rodríguez. Performance of a micro-channel plates position sensitive

detector. *Nuclear Instruments and Methods in Physics Research Section A: Accelerators, Spectrometers, Detectors and Associated Equipment*, 551(23):375 – 386, 2005.

[49] Nicholas David Scielzo. *Measuring the $\beta - \nu$ asymmetry in Laser Trapped ^{21}Na.* PhD thesis, University of California, Berkely, 2003.

[50] W. C. Wiley and I. H. McLaren. Time-of-Flight Mass Spectrometer with Improved Resolution. *Review of Scientific Instruments*, 26(12):1150–1157, 1955.

[51] R. Dörner, V. Mergel, L. Spielberger, M. Achler, Kh. Khayyat, T. Vogt, H. Bräuning, O. Jagutzki, T. Weber, J. Ullrich, R. Moshammer, M. Unverzagt, W. Schmitt, H. Khemliche, M.H. Prior, C.L. Cocke, J. Feagin, R.E. Olson, and H. Schmidt-Böcking. Kinematically complete experiments using cold target recoil ion momentum spectroscopy. *Nuclear Instruments and Methods in Physics Research Section B: Beam Interactions with Materials and Atoms*, 124(23):225 – 231, 1997.

[52] Steven Knoop, Reinhard Morgenstern, and Ronnie Hoekstra. Direct observation of pure one-electron capture from the target inner shell in low-energy $p + \mathrm{Na}$ collisions. *Phys. Rev. A*, 70:050702, Nov 2004.

[53] S. M. Seltzer J. H. Hubbell. Tables of X-Ray Mass Attenuation Coefficients and Mass Energy-Absorption Coefficients from 1 keV to 20 MeV for Elements Z = 1 to 92 and 48 Additional Substances of Dosimetric Interest. http://www.nist.gov/pml/data/xraycoef/index.cfm.

[54] M. J. Martin Weitz. Nuclear Data Sheets 70,315, 1993.

[55] E. Browne. Nuclear Data Sheets 82, 379, 1997.

[56] X Fléchard, Ph Velten, E Liénard, A Méry, D Rodríguez, G Ban, D Durand, F Mauger, O Naviliat-Cuncic, and J C Thomas. Measurement of the correlation coefficient a in the decay of trapped 6 He + ions. *Journal of Physics G: Nuclear and Particle Physics*, 38(5):055101, 2011.